BRNO UNIVERSITY OF TECHNOLOGY

VYSOKÉ UČENÍ TECHNICKÉ V BRNĚ

FACULTY OF MECHANICAL ENGINEERING

FAKULTA STROJNÍHO INŽENÝRSTVÍ

INSTITUTE OF SOLID MECHANICS, MECHATRONICS AND BIOMECHANICS

ÚSTAV MECHANIKY TĚLES, MECHATRONIKY A BIOMECHANIKY

DESCRIPTION OF FATIGUE BEHAVIOR OF ADDITIVELY MANUFACTURED POLYMER METAMATERIAL STRUCTURE

POPIS ÚNAVOVÉHO CHOVÁNÍ POLYMERNÍ 3D TIŠTĚNÉ METAMATERIÁLOVÉ STRUKTURY

MASTER'S THESIS

DIPLOMOVÁ PRÁCE

AUTHOR
AUTOR PRÁCE

Bc. Petra Helešicová

SUPERVISOR
VEDOUCÍ PRÁCE

Ing. Lukáš Trávníček, Ph.D.

BRNO 2024

Assignment Master's Thesis

Institut:	Institute of Solid Mechanics, Mechatronics and Biomechanics
Student:	**Bc. Petra Helešicová**
Degree programm:	Engineering Mechanics and Biomechanics
Branch:	Engineering Mechanics
Supervisor:	**Ing. Lukáš Trávníček, Ph.D.**
Academic year:	2023/24

As provided for by the Act No. 111/98 Coll. on higher educati on institutions and the BUT Study and Examination Regulations, the director of the Institute hereb y assigns the following topic of Master's Thesis:

Description of fatigue behavior of additively manufactured polymer metamaterial structure

Brief Description:

Mechanical polymer metamaterials allowing variable stiffness gaine d interest due to their potential within structural applications. The production of these metama terials is often done by 3D printing technology, which is a production method that has been used in recent years and is still being researched. For the successful application of the mentioned struct ure, its short–term and long–term behavior must be described. The main goal of the the sis will, therefore, be to predict the fatigue lifetime of a mechanical metamaterial structure. Due t o the complex geometry of the structure, it is necessary to use numerical modeling using the fini te element method. The necessary material models will be created based on the measured exp erimental data. The results will be validated using experimental fatigue measurements on a real structure. The thesis will be developed in cooperation with the Institute of Physics of Materials, AS CR.

Master's Thesis goals:

1. Study additive manufacturing technology and fatigue life prediction criteria for polymers.
2. Carry out static and fatigue experiments on 3D printed speci mens to characterize the material behavior and to create the necessary material model.
3. Create a numerical model of the metamaterial structure.
4. Predict the fatigue lifetime of a metamaterial structure using different fatigue criteria.
5. Validation of the obtained results using experimental fatigue measurements on a real structure.

Recommended bibliography:

FLEISCH, M.; THALHAMER, A.; MEIER, G.; RAGUŽ, I.; FUCHS, P.F. et al. Functional mechanical metamaterial with independently tunable stiffness in the three spatial directions. Materials Today Advances. 2021, č. Volume 11, s. 100155. ISSN 2590-0498.

OSSWALD, Tim A. a MENGES, Georg. Material science of polymers for engineers. 3rd edition. Cincinnati: Hanser Publishers, [2012]. ISBN 9781569905142.

MCKEEN, Laurence W. Fatigue and Tribological Properties of Plastics and Elastomers. Third Edition. William Andrew, 2016. ISBN 978-0-323-44201-5.

Deadline for submission Master's Thesis is given by the Schedule of the Academic year 2023/24

In Brno,

L. S.

_____   _____
prof. Ing. Jindřich Petruška, CSc.   doc. Ing. Jiří Hlinka, Ph.D.
Director of the Institute   FME dean

ABSTRACT

Metamaterials have become a highly researched area in recent years because they enable customisation of mechanical properties in manufactured components, which would not be possible when using conventional materials. To safely utilise metamaterials in operation, it is necessary to describe their behaviour under load. The presented master's thesis deals with a description of the fatigue behaviour of a 3D printed polymeric metamaterial structure. The thesis is divided into theoretical and practical part. In the theoretical part, a review of metamaterials and their classification is presented, followed by a review of 3D printing methods suitable for polymeric materials, and the basics of mechanical behaviour of polymers. In the practical part, steps are taken to estimate the fatigue life of the proposed metamaterial structure using four criteria. Mechanical properties of the additively manufactured material are measured in a series of experiments. The measured properties are used as input data for a numerical model. The boundary conditions and loading of the model are set to correspond to the real loading conditions. The numerical model is used to assess critical locations within the structure and to predict the fatigue lifetime. Stress and strain values representing steps of cyclic loading are recorded at two critical locations. These values are used to predict the fatigue life.

KEYWORDS

metamaterial, fatigue, lifetime estimation, numerical modelling, finite element method, additive manufacturing

ABSTRAKT

Metamateriály jsou v posledních letech velmi často zkoumanou oblastí, jelikož umožňují přizpůsobení mechanických vlastností vyráběných součástí, které není možné získat s využitím konvenčních materiálů. Aby bylo možné metamateriály bezpečně využívat v provozu, je nutné popsat jejich chování při zatěžování. Prezentovaná diplomová práce je zaměřena na popis únavového chování 3D tištěné polymerní metamateriálové struktury. Práce je rozdělena na teoretickou a praktickou část. V teoretické části je provedena rešerše metamateriálů a jejich rozdělení, poté rešerše metod 3D tisku vhodných pro polymerní materiály a nakonec jsou představeny základy mechanického chování polymerů. V praktické části jsou postupně prováděny kroky pro určení odhadu únavové životnosti uvažované metamateriálové struktury pomocí čtyř kritérií. Pomocí experimentálních testů jsou naměřeny mechanické vlastnosti uvažovaného materiálu, které jsou vloženy do vytvořeného numerického modelu. Okrajové podmínky a zatížení modelu jsou zvoleny tak, aby odpovídaly reálným podmínkám při zatěžování. Numerický model je využitý pro určení kritických lokací ve struktuře a pro predikci únavové životnosti. Ve dvou kritických místech jsou zaznamenávány hodnoty napětí a přetvoření představující jednotlivé fáze cyklického zatěžování. Tyto hodnoty jsou použity pro predikci únavové životnosti.

KLÍČOVÁ SLOVA

metamateriál, únavové zatížení, odhad životnosti, numerické modelování, metoda konečných prvků, 3D tisk

Author's Declaration

Author:	Bc. Petra Helešicová
Author's ID:	208605
Paper type:	Master's Thesis
Academic year:	2023/24
Topic:	Description of fatigue behaviour of 3D printed polymer metamaterial structure

I declare that I have written this thesis independently, under the guidance of the advisor and using exclusively the technical references and other sources of information cited in the thesis and listed in the comprehensive bibliography at the end of the thesis.

As the author, I furthermore declare that, with respect to the creation of this thesis, I have not infringed any copyright or violated anyone's personal and/or ownership rights. In this context, I am fully aware of the consequences of breaking Regulation § 11 of the Copyright Act No. 121/2000 Coll. of the Czech Republic, as amended, and of any breach of rights related to intellectual property or introduced within amendments to relevant Acts such as the Intellectual Property Act or the Criminal Code, Act No. 40/2009 Coll. of the Czech Republic, Section 2, Head VI, Part 4.

Brno . . . .
                                                             author's signature*

---

*The author signs only in the printed version.

ACKNOWLEDGEMENT

Contents

1   Introduction

The mechanical behaviour of the material plays a crucial role in the design process of an engineering application. Mechanical parameters are widely and extensively studied, and materials are newly created or altered to obtain values of properties that would meet the requirements needed for a given application. These range widely from aerospace engineering requiring strong and lightweight durable materials to biomedical applications recreating the mechanical properties of human tissue. Traditional materials have properties given by their composition and structure, often an area of material engineers, where grain size or alloying change the properties of material less, or more significantly. This approach is well established and is used commonly, however, there are limitations in manufacturing processes, that restrict the creation of customised mechanical properties.

The solution to the customisation of mechanical properties might have appeared during the last decades, with the evolution of mechanical metamaterials. Metamaterials allow for customisation of behaviour, gaining their properties not only by structure and composition as traditional materials but, more importantly by their geometry. The topology of the structure allows for custom, tunable, or non-convential mechanical properties. This area offers a very lucrative manufacturing scheme, with properties that fit the requirements perfectly for a given application.

Metamaterials became highly researched thanks to the development of additive manufacturing (AM). The principle of this fabrication process lies in creating the geometry, layer by layer, based on a computer-aided design (CAD) model that allows for great precision and complex geometry to be created. CAD enables geometry changes to be easily made, which changes the properties when manufactured. AM methods range from fused filament fabrication (FFF) for large-scale units through selective laser sintering (SLS) to Vat photopolymerisation for components as small as several micrometres.

To further increase the applicability of metamaterials together with AM, different base materials are used. Many mechanical metamaterials are fabricated from polymer materials. These have areas of properties where they exceed conventional engineering materials, such as metals, or ceramics. In addition, they are accessible and lightweight. Using a range of materials, modern manufacturing methods and a process of creating metamaterials with custom mechanical properties creates a nearly unlimited area of applicability.

However, given the elaborate topology of the structures, the resulting stress state in a loaded component can be complex. To safely use the mechanical metamaterials, we need to know the short- and long-term behaviour of the structure. This must be evaluated for every structure that will be used in an application to ensure a safe operating conditions and prevent complications. A metamaterial structure that allows for tunable stiffness fabricated by FFF was analysed, its mechanical properties were measured for a given geometry configuration and a material model was created. Fatigue properties were measured and lifetime was predicted using a combination of experimental tests and numerical modelling.

2 Problem situation analysis and thesis goals

2.1 Problem situation formulation

Additive manufacturing of polymers is becoming a regular manufacturing process as methods advance and finished products become more suitable for engineering applications. These methods allow for fabrication of intricate design features that are not available by common fabrication methods (extrusion, blow moulding, etc.). The manufacturing of metamaterials has progressed with improvements in additive technologies, resulting in the ability to create complex geometries with unusual or tunable properties. To safely put metamaterials into practice, short-term behaviour must be described and long-term lifetime must be predicted, as for any other mechanical part. However, that is not a trivial task for metamaterials due to the complexity of their structures.

To predict the lifetime of the proposed metamaterial structure, the behaviour of the material must first be described under static and cyclic loading. Therefore, one of the thesis' goals is to execute quasi-static and fatigue laboratory tests while considering various printing orientations. Based on the results obtained from the static testing of standardised specimens, the material model will be constructed. Numerical modelling is used to obtain a detailed description of the stress states at the critical locations of the metamaterial structure. The fatigue lifetime of the metamaterial structure will be estimated using numerical simulations and material fatigue test results by applying criteria from the literature. These estimations will be validated by laboratory fatigue tests of the whole structure.

2.2 Problem formulation

Predicting the fatigue lifetime of a metamaterial structure using numerical modelling in combination with experimentally obtained data.

2.3 Thesis goals

Goals set for the thesis include;

- Research the topic of additive manufacturing and fatigue life prediction criteria for polymers.
- Carry out quasi-static and fatigue experiments on 3D printed specimens to define the material model.
- Create a numerical model of the metamaterial structure using data from experiments.
- Apply fatigue lifetime prediction criteria and evaluate their appropriacy using validation experiments of the metamaterial structure.

3 Metamaterials

Metamaterials are a branch of materials that gain their properties through the detailed and precise architecture of their geometry, on top of the properties of a given material. As a result of this precise design, metamaterials can mimic the behaviour of a different structure or material or exhibit properties that are considered unnatural for commonly found materials. These properties include e.g. a negative Poisson's ratio, a negative refraction index, and negative electrical permittivity and magnetic permeability. These properties cannot be obtained using common means of fabrication either. They are most commonly manufactured using a base *"cell"* that is repeated to create a complete structure. Figure 3.1 shows three examples of metamaterial structures that vary in size and fabrication method. The idea of metamaterials originated for the first time in the electromagnetics area, where theoretical investigation of materials with simultaneous negative values of the dielectric constant and magnetic permeability was conducted in the 1960s [1].
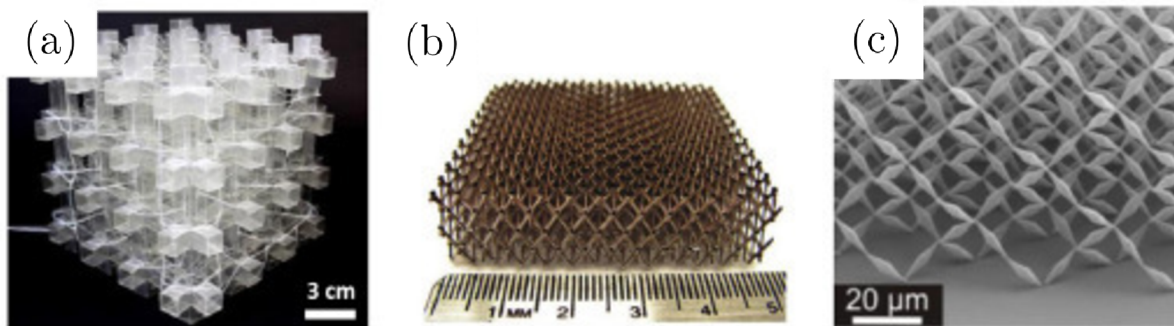
Fig. 3.1: Examples of different metamaterial structures varying in sizes and fabrication process. (a) Transformable origami-inspired metamaterial actuated by pressurizing its unit cells. (b) Hollow Ni-P microlattice synthetsized by Self-Propagating Polymer Waveguides, electroless plating and polymer etching. (c) Metamaterial with ultra large bulk modulus to shear modulus ratio fabricated using Two-Photon Lithography. [2]

Although metamaterials have originated in electromagnetics, they have gained much popularity, especially in recent years, because of their versatile potential to be used in various fields, not purely focused on electromagnetics. The progress of fabrication processes drives the expansion of metamaterials as more complex structures can be created, which again creates pressure to get higher resolution and better quality of manufacturing. The main categories of metamaterials, as described in [3], are;

- Electromagnetic metamaterials
- Acoustic metamaterials
- Thermal metamaterials
- Mechanical metamaterials.

3.1 Electromagnetic metamaterials

As stated above, electromagnetic metamaterials were groundbreaking in the area of material structures with unconventional characteristics. Electromagnetic metamaterials can have negative electrical permittivity or magnetic permeability or both. Conventional materials with both of these parameters positive are called Double-Positive materials (DPS). Metamaterials with one of these variables being negative are called Single-Negative metamaterials (SNG). The combination of complimentary negative-permittivity material and negative-permeability material leads to a left-handed electric field, magnetic field, and phase vector [1]. This resulted in these metamaterials being called Left-Handed Materials (LHM) [3] or Double-Negative metamaterials (DNG) [4]. Negative values of these parameters result in a variety of uncommon behaviours.

The negative refractive index can be observed at an interface between standard (DPS) matter and DNG materials, where the refracted wave has a negative angle and propagates "backwards", as shown in Fig. 3.2 [4]. The reverse Doppler effect can be observed in electromagnetic metamaterials, where the approaching wave source results in a lower frequency [1; 4]. Electromagnetic metamaterials are used for optical applications, such as a "super-lens" that focuses the light at a point smaller than the wavelength of the used light [1], antennas that allow scanning in all directions including sideways and backwards, radar absorbers, etc. [1; 3; 4].
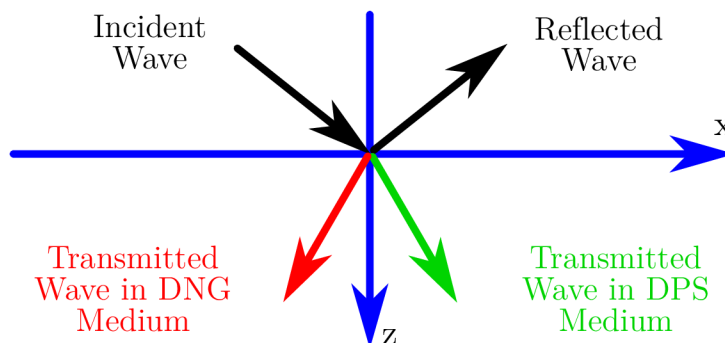
Fig. 3.2: Geometry of the scattering of a wave on a DPS-DNG interface [4].

3.2 Acoustic metamaterials

Acoustic metamaterials deal with sound waves and vibrations, which are generally very difficult to manipulate. The work with sound waves is usually done by transforming them into electronic forms and using electronic appliances [5]. Acoustic metamaterials present a way to alter sound waves using the material without external devices. The wave propagation is governed by the bulk modulus and the mass density of the material/structure. The evolution of acoustic metamaterials occurred hand in hand with the evolution of electromagnetic metamaterials, as a simple analogy can be proposed where bulk modulus is analogous to magnetic permeability and mass density is analogical to electric permittivity [6]. Materials observed in nature have both of these parameters positive; however, metamaterials allow the building of negative bulk modulus and/or negative mass density structures.

Acoustic imaging is one of the proposed applications that is analogous to super-lens mentioned in Section 3.1. The negative refraction index allows for high-precision imaging using acoustic waves, which could detect small cracks in buildings or early stage tumours [5]. Metasurfaces consist of coiled elements or resonant membranes and act as wavefront shaping devices that allow controlling the wave and focusing the sound [5; 6]. Negative refraction was obtained using a metasurface with coiled elements as shown in Fig. 3.3. In general, various porous materials are used for sound absorption. The lower the frequency of the sound wave, the thicker the material must be to successfully absorb the waves. Acoustic metamaterials use very high energy density structures coupled with impedance matching, which allow high absorption at very small thickness, creating acoustic cloaking [5]. Active acoustic metamaterials allow for tunability of the structures in real time as a response to incoming sound waves [5; 6].
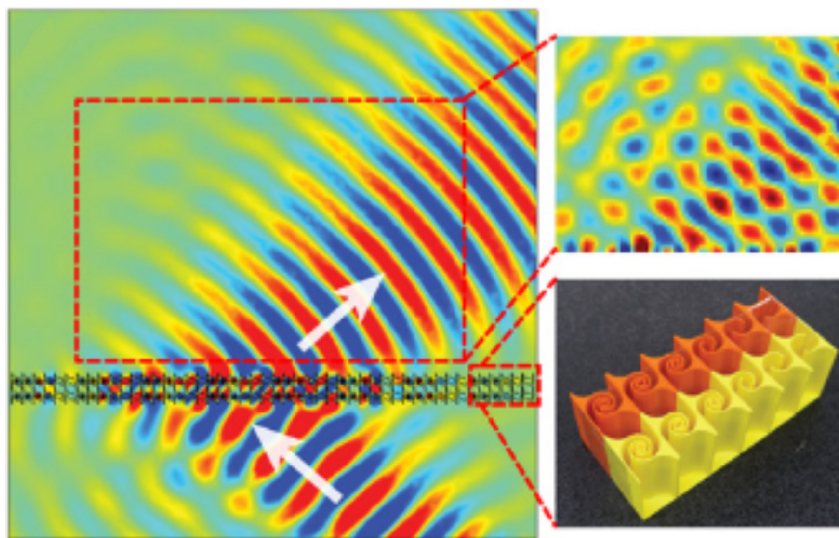

Fig. 3.3: Metasurface structure generating a negative refraction of the transmitted wave. Simulation result of pressure (Left), Experimentally measured pressure map (Right Top), Metasurface structure with coiled elements (Right Bottom) [6].

3.3 Thermal metamaterials

Thermal metamaterials alter the flow of heat in an environment. Metamaterials are utilised in this area in two ways; creating thermal properties of structures that are not found in nature (this category is discussed in Section 3.4.3), or manipulating the heat transfer. Controlling the flow can be used to generate work, used for cooling or heating, or create thermal equilibrium [7]. Design approaches for thermal metamaterials can be divided into macroscopic phenomenological theory and microscopic photonic/thermal photonic theory.

Macroscopic approaches utilise the transformation theory, in which conductivities are mathematically predicted for a desired state and tailored to reach the desired behaviour [8]. These metamaterials are commonly fabricated using so-called "binary-layered structures", where currents perpendicular and parallel experience two materials in series and in parallel, respectively [7]. This transformation allows for the creation of thermal devices

(depicted in Fig. 3.4) such as cloaks, where the structure copies the thermal gradient of the environment, concentrators, where the temperature gradient is condensed into a smaller region, or the rotator which changes the direction of the temperature gradient within the structure [7; 9]. Other devices such as a bilayer thermal cloak or multiphysics invisible sensor have been manufactured [9].
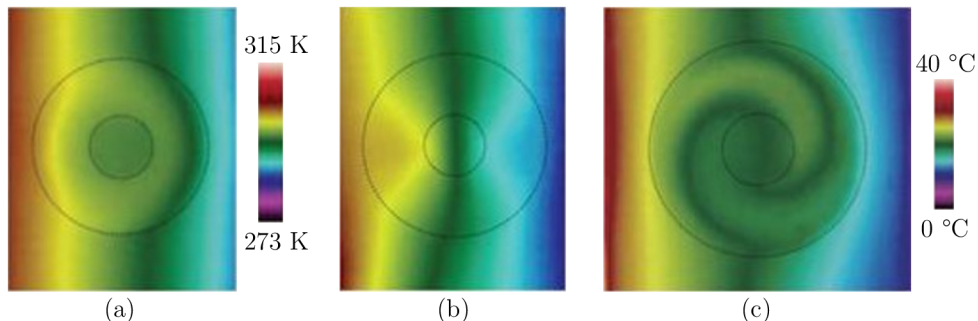

Fig. 3.4: Temperature gradient within different thermal metamaterial devices. (a) Cloak, (b) concentrator, (c) rotator [7].

Microscopic theory controls heat transfer through photons, which are the heat carriers in semiconductors and insulators [8]. By altering the photon behaviour, the thermal properties can be manipulated. Thermal crystals have been used to block photon frequency bands by scattering [8], thus manipulating thermal behaviour. Nanophotonic metamaterials utilise local resonances to govern thermal conductivity [9].

3.4 Mechanical metamaterials

Mechanical metamaterials provide an alternation of mechanical properties of structures that would not be possible to obtain with conventional materials and components. Mechanical metamaterials have been studied extensively in recent years because of their high practicality. Traditional mechanical metamaterials follow the ideas of the families of metamaterials mentioned above, creating a zero or negative value of the mechanical properties, such as negative Poisson's ratio (also called auxetic metamaterials), negative compressibility, or negative thermal expansion [2; 10; 11]. A special feature of mechanical metamaterials is tunable stiffness. Furthermore, mechanical metamaterials are not limited to switching between two states, but can reach any state in between due to combinations of counterintuitive properties [11].

3.4.1 Negative Poisson's ratio

Poisson's ratio μ is defined as $\mu = -\frac{\varepsilon_T}{\varepsilon_L}$, with ε_T and ε_L being the strains in transversal and loading direction, respectively [11]. Standard materials exhibit a value of Poisson's ratio between 0 (cork) and 0,5 (rubber). When the load is applied, the longitudinal length increases and the transverse length decreases, or vice versa. Auxetic structures (alternative name for negative Poisson's ratio structures) use different principles to reach a negative value of Poisson's ratio, which results in elongation/contraction in both directions when load is applied. Five main categories (as shown in Fig. 3.5) are re-entrant, chiral, rotating,

crupmled sheets, and perforated sheets [10]. The negative value of μ can help prevent indentation with high energy absorption, provide tunable stiffness or resist shear [2].
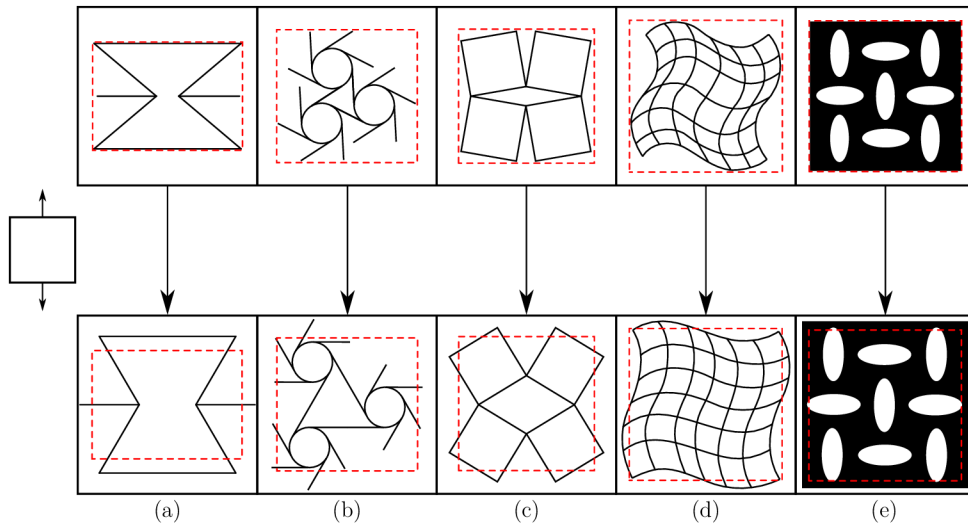

Fig. 3.5: Categories of auxetics metamaterials (a) re-entrant, (b) chiral, (c) rotating, (d) crumpled sheets, (e) perforated sheets in their undeformed state (upper row) and deformed state in tension (bottom row) [10].

3.4.2 Negative compressibility

Compressibility describes the relative volume change of a material during pressure change [11]. Standard materials show positive compressibility, which means that they contract under compression and expand under tension. Negative compressibility occurs in nature in only a very limited number of crystals [2], where the unit elongates in at least one direction when pressure is applied (as shown in Fig. 3.6). In man-made structures, it can occur only when loading induces a transition from a stable state to a different metastable state, similar to the bistability of a structure in mechanics [11]. Several mechanisms have been proposed for obtaining negative compressibility, ranging from bimaterial strips through a particular geometry or constraints to a force potential mechanism. These have the ambition of being used in actuators, force amplifiers, or protective devices [11].
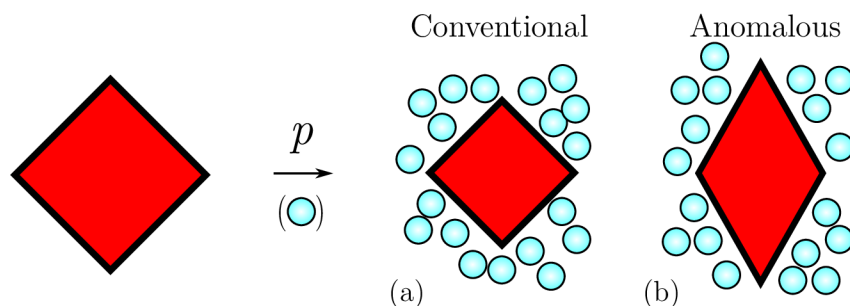

Fig. 3.6: Mechanical response to hydrostatic pressure in (a) conventional material, (b) anomalous material with negative linear compressibility [11].

3.4.3 Negative thermal expansion

The conventional exhibit of a positive thermal coefficient is elongation upon heating. Some cases of a negative thermal expansion (NTE) coefficient include water between 0° C and 4° C, where heating induces compression. Negative thermal coefficient metamaterials are produced by combining materials with distinctively different thermal coefficients in the structure (examples of NTE structures are shown in Fig. 3.7). This different response to heating then induces rotation or bending, which results in overall contraction [12]. Thermal expansion coefficient can be tuned for different values in different temperature ranges, allowing applications in dental fillings, laminates, or precision instruments [10; 12].
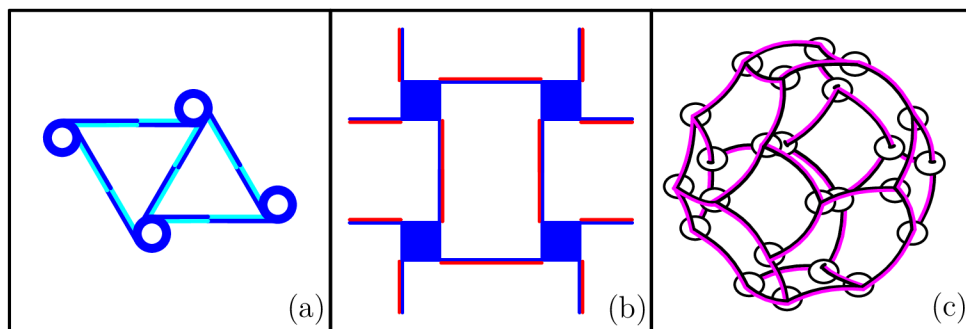

Fig. 3.7: Negative thermal expansion structures: (a) and (b) modified bi-material chiral structures, (c) foam cellular metamaterial with bi-material ribs inverted hexagonal cell [11].

3.4.4 Tunable stiffness

Many mechanical metamaterials can be created with tunable stiffness. Origami-inspired metamaterials exhibit low stiffness in the folding phase of deformation and high stiffness in the post-locking folding phase of deformation [2]. Given metamaterials with struts, such as lightweight structures or chiral structures, the stiffness is tuned by changing the thickness of the struts [13]. Metamaterials that use pattern transformation with holes offer stiffness tunability by changing the shape, size, or location of holes [11]. These types of metamaterials are shown in Fig. 3.8. The change in stiffness is induced by changing a geometry parameter. This can result in a change of other properties, such as the Poisson's ratio, or a change in stiffness in one direction can induce its change in another direction.
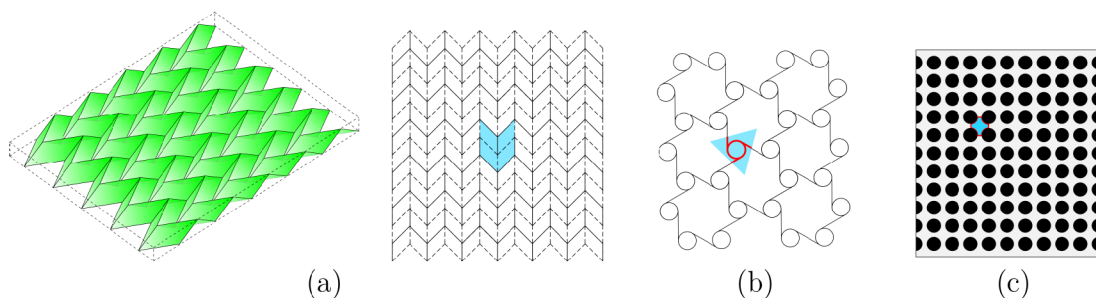

Fig. 3.8: Examples of metamaterial types with tunable stiffness and their unit cells. (a) Origami-inspired metamaterial "Miura-ori" in folded and unfolded form [2]. (b) Trichiral metamaterial structure. (c) Pattern transformation metamaterial "holey sheet" [11].

Fleisch et al. [13] have designed a metamaterial geometry with independent tunable stiffness in each direction (Fig. 3.9(a)). The structure consists of cubic nodes connected by struts in three spatial dimensions. By altering geometric features: cube size, distance between cubes, strut thickness, radius of fillets, and overhang of cubes, the stiffness can be changed independently locally, axially, or globally. This structure can be created as isotropic, orthotropic, or even anisotropic. Stiffness can be increased locally with smooth transitions of stiffness between cells. This structure is investigated in the practical part of the thesis.
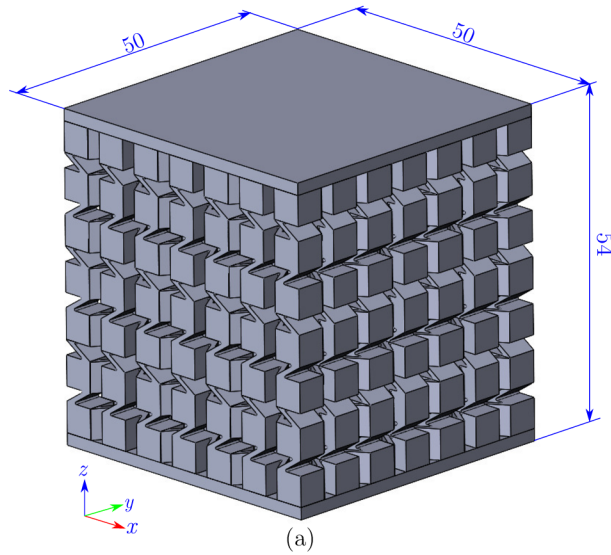

Fig. 3.9: Metamaterial structure with independently tunable stiffness [13], which is investigated in this thesis.

4 Additive manufacturing of polymer materials

4.1 Polymer materials

Polymer materials have changed the world. Like many other inventions, the main expansion of plastics occurred during the Second World War, where they were used for the production of parachutes, ropes, armour, and more [14]. Due to its versatility, the material group is used in many different applications ranging from everyday items to precisely manufactured industrial components.

There are many different categories and families of polymer materials that differ in their properties and intended usage. The main categories are thermoplastics, thermosets, and elastomers [15; 16].

- **Thermoplastic materials** solidify when cooled, but once reheated, the free movement of the chain molecules is allowed again. There is no cross-linking of molecules created during cooling, and the molecules can move independently of other molecules. Thermoplastics are further divided into *amorphous* and *semi-crystalline*. The structure of amorphous polymers solidifies in a disorder of molecules, resulting in a random molecular structure. Semi-crystalline polymer molecules begin to arrange in order when they cool, forming spherulites with lamellae of arranged crystalline regions and amorphous regions between them (Fig. 4.1). These spherulites could be compared to grains in metallic materials. Approximately 85% of polymers produced are thermoplastics [15; 17].
- **Thermosetting polymers**' molecules cross-link during cooling and create a solid network that does not allow any movement of the individual molecules. These cross-links are not influenced by any subsequent reheating, and thus, the material flow is restrained even after reheating. Cross-links are made up of chemical bonds (ionic or covalent), physical bonds (van der Waals forces), and hydrogen bonds.
- **Elastomers** get cross-linked during cooling. However, this cross-linking is only light and allows for a very large extension of the molecules. These bonds prevent the molecules from sliding and make even large deformations reversible.

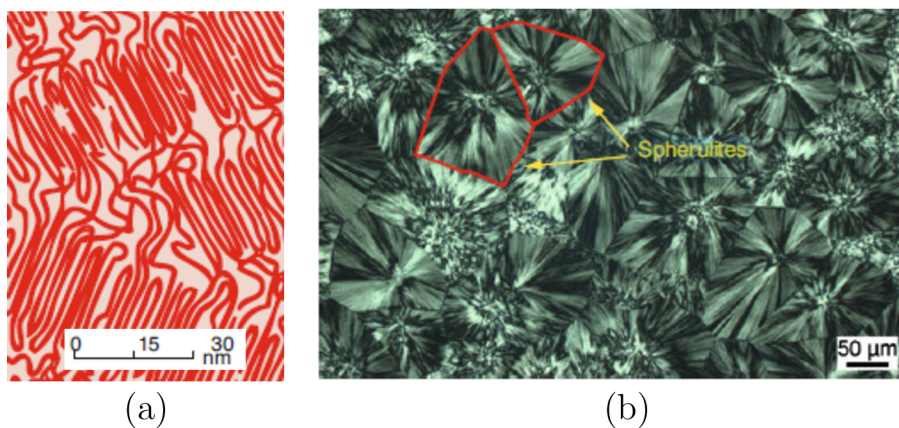

(a)   (b)

Fig. 4.1: (a) Schematic of a semi-crystalline structure in a spherulite, (b) Spherulites in polypropylene [15].

Additive manufacturing uses all three categories of polymers as feedstock. Feedstock can be in the form of liquid polymers, polymer powders, filaments, sheets, or pellets [18]. The materials can be used plain or reinforced with fibres. Some of the commonly used polymers for 3D printing are polylactic acid (PLA), acrylonitrile butadiene styrene (ABS), polyether ether ketone (PEEK), and polyamides (PA).

Polylactic acid (PLA) is an organically sourced polymer, produced from corn starch or sugar cane [19]. It can be produced as amorphous or semi-crystalline. The mollecular structure, molecular orientation, and crystallinity all affect the mechanical properties of the finished product. The properties can thus be altered to suit a specific application. In general, PLA has good mechanical properties comparable to those of synthetic polymers such as polypropylene (PP) or polyethylene (PE). It tends to be more fragile than those materials, and plasticisers are often added to improve flexibility and impact strength [18]. PLA is a popular material for 3D printing in the general population. It is suitable for most additive manufacturing methods including vat photopolymerization and material jetting. As a result of its low melting temperature, PLA is commonly used in fused deposition modelling (FDM). The printed layers have good adhesion and the finished product can be painted or machined. However, the material degrades over time and has low heat resistance, making it less suitable for engineering applications [18]. It is a popular starting filament for home printers to create household items or decorations. Due to the biocompatibility of the material, PLA is used for the printing of biomedical parts [19].

Acrylonitrile butadiene styrene (ABS) is a copolymer made of three polymers: acrylonitrile, butadiene, and styrene. It is an amorphous polymer produced by three different techniques. Each of them results in slightly different mechanical properties of the material [19]. In general, ABS has very high strength (including impact strength) and toughness. It has good resistance to abrasion, insulating properties, and dimensional stability. The versatility of colour and surface texture allows for a wide variety of applications [18]. The main disadvantage of ABS is its poor environmental resistance and low resistance to UV light and heat. ABS is another very common filament for additive manufacturing. The low melting temperature of this amorphous polymer and its easy processing make it well suited for extrusion-based methods. Compared to PLA, ABS is less brittle and has more available finishing techniques. ABS is popular for printing concept models, fixtures, and even interlocking parts, such as gears, because of the toughness of the material.

Polyether ether ketone (PEEK) is an organic aromatic thermoplastic polymer. It is semi-crystalline and its exceptional properties rank it among high performance polymers [18]. The melting point of PEEK is above 300 °C, which makes the thermal resistance very high. Continuous use is possible at temperatures up to 250 °C [19]. The resistance to solvents and chemical inertness result in a very stable material. PEEK is very tough and withstands dynamic loading as well as abrasion and wear. The downsides are low UV resistance and expensive production, making PEEK more suitable for targeted applications requiring high performance, such as aerospace parts [18]. PEEK requires more powerful printing tools than PLA and ABS because of its high melting temperature. It can be used in sheet lamination or material extrusion methods. The stability of temperature must be ensured to keep the material properties good for the whole structure. PEEK can be used

as metal replacement or end-use parts for industries such as automotive or aerospace. The biocompatibility of the material and the good mechanical behaviour make PEEK suitable for the replacement of metal or ceramic implants [18].

Polyamides (PA), also called nylons, belong to the family of engineering resins (together with Acrylonitrie Butadiene Styrene (ABS) or Polyethylene Terephthalate (PET)). They are created as *homopolymers* including only one type of monomer, *copolymers* which consist of a mixture of monomers or *reinforced polyamides*, which consist of a reinforcement that increases the mechanical parameters of the finished product. Reinforcement is usually realised by glass fibres in varying ratios. Polyamides are semi-crystalline and tend to be very tough. Good abrasion, impact, and wear resistance make them suitable for engineering applications [18]. The nature of the polymer allows for the creation of bulk products as well as very fine filaments. This versatility results in a wide range of applications for polyamides. PA is a widely used material for 3D printing by extrusion methods. The printing process is as easy as for PLA and ABS, but the mechanical properties are good enough for engineering applications. In powder form, PA is commonly used for selective laser sintering. Polyamides are easily mouldable and extruded, allowing complex shapes to be created. They exhibit good electrical insulation, corrosion resistance, and toughness, so they can be used for electrical applications, housings, or cable ties [20]. Fibre production allows the manufacturing of polyamide fabrics.

4.2   Additive manufacturing methods

Additive manufacturing (AM) is the process of creating 3D structures by printing them layer by layer. The desired part is created as a computer-aided design (CAD) model and is used as a source for the machine, which builds on the layers to "print" the full volume. This process has become widely popular due to its variability, which allows for highly customised shapes or batch making. 3D printing, which is an interchangeable term for additive manufacturing, is applicable to many different materials, ranging from metals, ceramics, to polymers. An ISO/ASTM standard [21] was created that separates AM processes into two types of processes, which are single-step and multi-step processes (see Fig.4.2).

- **Single-step processes** are processes in which the intended shape and the targeted mechanical properties are reached within a single-step operation. This type contains processes defined by the fusion of similar materials. Additive manufacturing of polymers is often realised in a single-step process.
- **Multi-step processes** require two or more operations to reach the final product. The first step usually provides the geometry, whereas the mechanical properties are reached with the consolidation of the material during the second step.

These processes are further divided by the standard into seven basic categories of manufacturing processes, which are binder jetting (BJT), directed energy deposition (DED), material extrusion (MEX), material jetting (MJT), powder bed fusion (PBF), sheet lamination (SHL) and vat photopolymetrisation (VPP). Of these, all categories are relevant
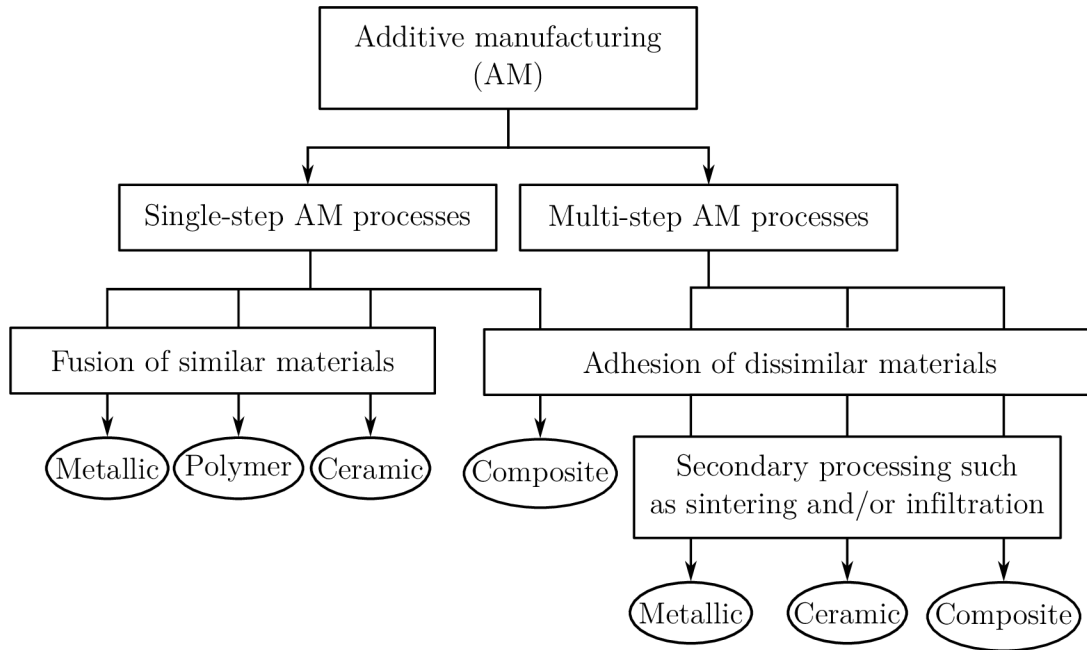
Fig. 4.2: Assortment of single-step and multi-step AM process and the material used [21].

to polymer materials, except for directed energy deposition, which is used for metallic materials.

There are numerous ways in which a 3D printed polymer object can be created. The type of bonding is one of the fundamental aspects of the chosen process, which is then further divided by the material feedstock (in what state is the material delivered to the system), and how is the material distributed into the individual layers. This then determines the manufacturing process. The overview of the single-step processes of polymer materials is shown in Fig. 4.3.
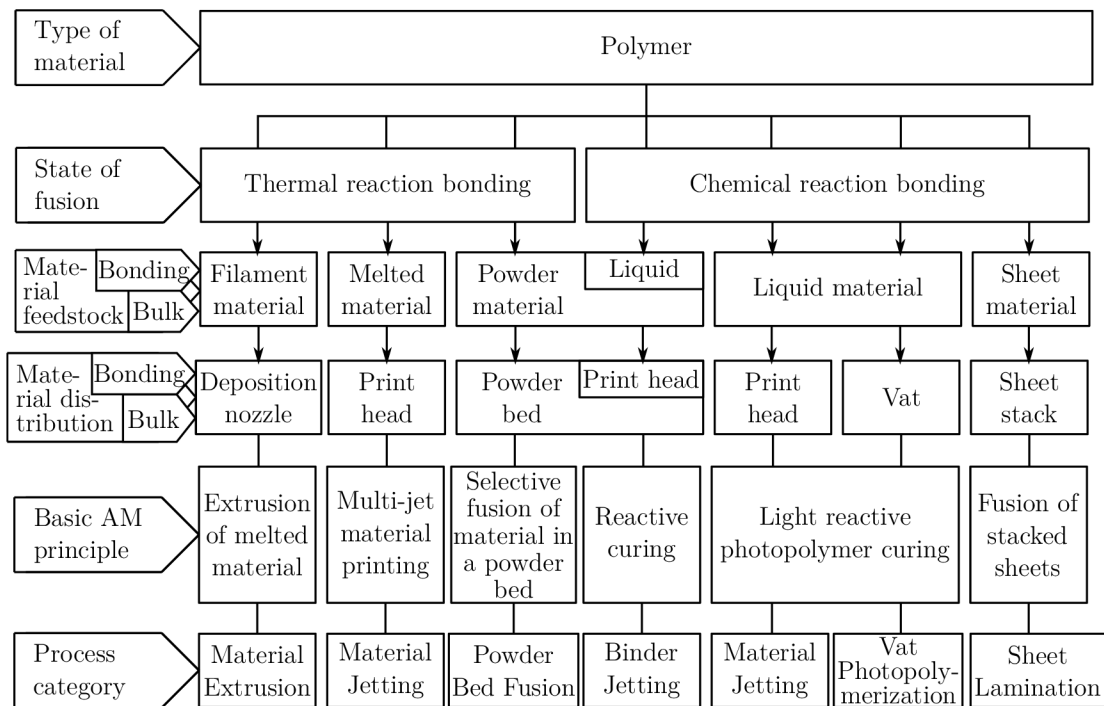

Fig. 4.3: Overview of single-step AM processing principles for polymer materials [21].

4.2.1 Binder Jetting (BJT)

Binder jetting is a chemical reaction type of 3D printing process. Instead of using heat to fuse the material particles together, a liquid binder is used to bond the powdered bulk material together. In the first step, the bulk material is layered onto the base, and in the second step the printhead distributes the binder to glue the particles together to form a layer of the part as defined by the source CAD model. The base is then moved downwards by the thickness of one layer, and steps one and two are repeated until the whole part is created. The residual powder in each layer remains on the base and provides temporary support for the part, so no structural supports need to be created. Fig. 4.4 shows a schematic representation of the binder jetting machine and process.
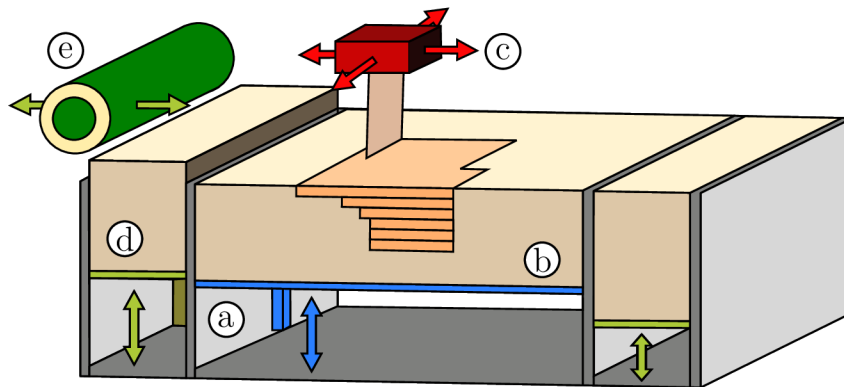

Fig. 4.4: Binder jetting apparatus consisting of (a) vertically movable base platform, (b) printed model embedded in supporting powder bed, (c) inkjet printing head, (d) support material feed stock, and (e) roller for powder distribution [22].

Choosing the right binder is a crucial part of the process, and many requirements are placed on the binder, such as low viscosity, good powder interaction, and long shelf life [23]. The binder for polymer feedstock is commonly a solvent/solvent mixture, which swells the polymer powder and causes entanglement of the polymer chains within the particles. Another option is to use film-forming polymers or polymer dispersions as binders [22]. Binders can be used in two ways; In-liquid or In-Bed. In-Liquid binders are present in the jetted medium and are used mainly for metallic and ceramic powders, while in-bed binders are often used in polymers such as poly(vinyl alcohol) (PVA) or poly(lactic acid) (PLA) [22]. The binder is activated by the jetted ink, which is clear of binders, which helps prolong the print head lifetime as there is no risk of binder creating clusters that would clog the system.

Green parts, as are the initial products manufactured by BJT called, are highly porous, as the in-bed binders generally dissolve and leave voids in the structure [23]. As a result of this, metallic and ceramic parts are often sintered after binder jetting to densify the material and enhance the mechanical properties. That is difficult for many polymeric structures, although some research has been concluded [24]. BJT is thus more suitable for the creation of structures where porosity is desired or for the creation of models for concept modelling that do not require good mechanical properties.

4.2.2 Material Extrusion (MEX)

As the name suggests, parts manufactured by material extrusion are created by layer-by-layer extrusion of the feedstock, which can be polymer filaments, viscous inks of polymer pellets, through a nozzle onto a base platform where they solidify [25]. After each layer, the base moves down/the nozzle moves up by the thickness of one layer and new layer of the CAD source model is printed. Material extrusion has become one of the most widely used manufacturing processes, since the apparatus and operation are straightforward, affordable and available to the general public. Many extrusion-based 3D printers are sold for low-scale printing at home or in an office environment [22]. Fused deposition modeling (FDM), and direct ink writing (DIW) can be found within this category.

- **Fused deposition modelling (FDM)**
  Thermoplastic polymer filaments or pellets are fed through a heated nozzle and brought above melt temperature before the layer is printed on the base plate/previous layer [25]. The nozzle is usually 0D so the 2D layer is produced by printing packed 1D lines of the material to create the whole layer. The fused deposition modelling process is shown in Fig. 4.5, where two nozzles are used to print the model and the support structures. In recent applications, the supports are often printed using the same material as the model and are removed later.
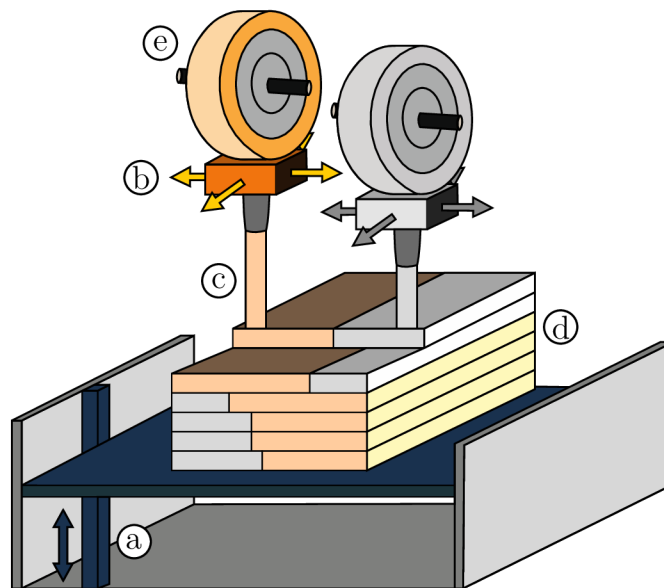

Fig. 4.5: Fused deposition modelling machine consisting of (a) vertically movable base platform, (b) tempered extrusion printing head for deposition of (c) model and (d) support material stored in (e) feedstocks containing filaments or pellets of thermoplastic materials [22].

The critical parameters of fused filament fabrication (FFF), which is an interchangeable term with FDM, are the melt rheology, the processing temperature, the build speed, and the CAD model shape parameters [22]. The correct combination of these parameters is crucial to manufacture a good quality product, and is different for each material. Complete fusion for the material needs to be ensured, rather than surface adhesion, which would result in a much weaker material prone to cracking

and delamination. The main disadvantages of the method lie in the narrow window where all parameters are aligned properly to produce a strong component. The size of the nozzle determines the roughness of the finished product, which is usually quite high, and the process tends to leave voids in the structure after printing.

FDM is a fabrication method suitable for the manufacturing of metamaterials. The technique allows multiple materials to be extruded simultaneously, which is used e.g. for dielectric metamaterials [26]. The feedstock can be prepared with various fibres/particles to change the behaviour of the material, and the method allows presenting discontinuities in printing and thus locally changing the behaviour of the material [26; 27]. Multimaterial nozzles have been introduced to the market, which also opens new possibilities for printing metamaterials [25].

- **Direct ink writing (DIW)**
  Although direct ink writing is also an extrusion manufacturing process and the machines may look quite similar, DIW does not need, unlike FDM, any heating of the used material. The material is pushed through the nozzle using pressure, and thus any material can be used as long as it meets the requirements of flowability [28]. This allows a wider range of materials to be used. The binding of the printed layers occurs after the deposition and solidification period using solvents or heat cure [25].

4.2.3   Material jetting (MJT)

Material jetting, also called inkjet printing, is an additive manufacturing process that uses a liquid material as an ink and creates the CAD source model replication by layering the material onto the surface [25]. The ink is distributed either in a continuous regime, where a consistent flow of droplets is present, or in a drop-on-demand regime, where individual droplets of the material are laid onto the surface when the system is triggered. The liquefied polymer must have a viscosity that is low enough to allow the forming of droplets.

The manufacturing apparatus of a trademarked PolyJet MJT machine is shown in Fig. 4.6. The multi-nozzle inkjet head deposits the model material and the support material. The model material is a photopolymer ink that is cured with UV light after each completed layer. The support material is applied in every layer to provide support for overhanging parts of the model. Unlike BJT, the supporting material must have a dense volume to provide sufficient support to the individual droplets [22]. The supporting material is disposed of after the product is finished.

Material jetting allows for multi-material printing. This is well suited for the manufacturing of metamaterials. MJT is popular for the construction of acoustic metamaterials, due to the easily altered frequency response of the material [27].
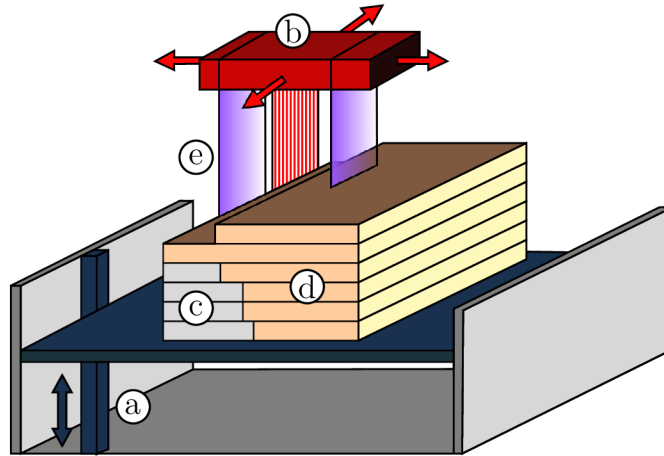
Fig. 4.6: Material jetting machine PolyJet consisting of (a) vertically movable base platform, (b) multi-nozzle inkjet head, (c) layers of support material, (d) layers of model material, and (e) UV light source attached to inkjet head [22].

4.2.4   Powder bed fusion (PBF)

In powder bed fusion, the model material is used in its powder form. A layer of powder is applied, and a localised heat source is used to melt the particles so that they coalesce and form a solid layer of the product. This is done for each layer of the model until the part is finished. The powder is applied as a consistent layer on the whole area and the uncoalesced particles act as supports for any overhanging sections [25]. The entire powder bed is often kept at elevated temperatures (but still below softening temperature) to allow stress relaxation and prevent distortions caused by internal stresses within the particles and layers [22]. The most prominent manufacturing process of polymers within the PBF is selective laser sintering (SLS).

Powder bed fusion processes are commonly used for manufacturing metamaterials as they allow complex structures to be created. These methods have, for example, been employed to create metamaterials with various Poisson's ratios [2; 27].

- **Selective laser sintering (SLS)**
  The general procedure of SLS has been explained above. Unlike another common method – selective laser melting (SLM), which is often used for metals and which melts the powder particles completely, SLS only softens the material to allow sintering of the particles. The selective laser sintering process in Fig. 4.7 shows components for layer distribution and heat transmission.

  SLS is one of the most widely used methods because of its high applicability to many materials. Virtually any material can be used as long as the particles are sinterable [25]. The manufactured parts also show good mechanical properties and are suitable for use in engineering applications [22]. The mechanical properties of the printed material are governed by the base material, the particle size, sintering temperature, and layer thickness. Most of the parts show a certain level of porosity, and the surface can be rough. These can become weak spots of the structure and are reduced by post-processing and/or coatings.
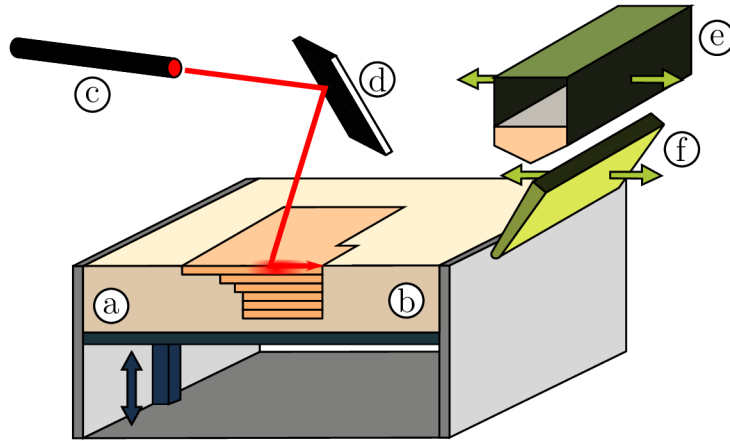
Fig. 4.7: Selective laser sintering machine consisting of (a) vertically movable base platform, (b) heated powder bed with embedded, sintered model layers, (c) laser source and (d) optics, (e) powder feedstock and deposition hopper, and (f) blade for powder distribution and levelling [22].

4.2.5 Sheet lamination (SHL)

Sheet lamination methods work on the basis of layering individual sheets of material on top of each other and subsequently laminating them in every step, while cutting out the model layers. Most commonly used methods include laminated object manufacturing (LOM), also called laminated layer manufacturing, and selective deposition lamination (SDL).

- **Laminated object manufacturing (LOM)**
  Laminated object manufacturing is a combination of additive and subtractive methods. A schematic build of the machine is shown in Fig. 4.8. A sheet of material (ranges anywhere from paper, polymers, to metals or fabrics) is stretched over the working area and adhesive is uniformly distributed over the whole area (this is the main difference between LOM and SDL, where SDL uses selective deposition of adhesive only on the cross section of the part, whereas LOM bonds together the outer material as well either by layering adhesive on the working area or using adhesive-coated sheets). The layers are laminated by a hot roller, and the cross section of the layer is cut out with a laser. The outer material is cut into cross-hatch for future disassembly and the base moves down by one layer thickness. This process is repeated until the entire part is created. Then the cross-hatch sections are removed and the finalised structure is obtained.

  LOM is more suitable for creating full-volume structures without internal cavities, as these are very complicated to make [25]. The process also creates a lot of waste, which makes it less advantageous for complicated structures, such as metamaterials.
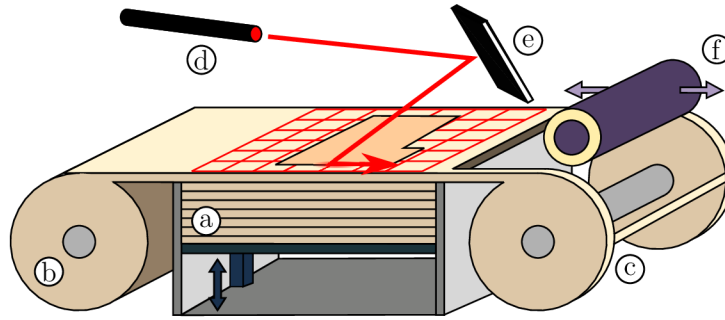
27

Fig. 4.8: Laminated object manufacturing (LOM) machine consisting of (a) vertically movable base platform, (b) material feedstock of sheet rolls, (c) residual material collection, (d) laser and (e) laser optics, and (f) heated roller [22].

4.2.6 Vat photopolymerisation (VPP)

The vat photopolymerisation methods are built on the principle of curing photosensitive polymer resins in a layer-by-layer manner using a light source such as a laser or digital projection that induces the polymerisation of initially liquid material. These methods include e.g. stereolithography, digital light processing, continuous liquid interface production, or two-photon polymerisation.

- **Stereolithography (SLA)**
  One of the early 3D printing methods is called stereolithography. A laser beam is used to cure photosensitive polymer resins in a layer-by-layer manner. The resin is stored in a vat, and the moveable platform is used as a base layer of the part. There are two approaches to SLA printing, as shown in Fig. 4.9. The terminology is not clearly established in the literature as it varies between publications [26; 27; 29; 30]. In this work, the terminology defined by Askari et al. [26] is used.

  The top-down approach starts with the platform under the resin surface by the thickness of a layer. A laser beam then cures the layer as defined by the CAD model and the platform moves down by a layer thickness again. In this manner, the whole structure is printed, while the previously printed layers are submerged in the uncured resin vat. Bottom-up mode utilises a transparent non-adherent plate under the resin vat to apply the light source to the layer and polymerise the monomers, and the base platform then moves upwards, so the structure suspends from the platform outside the resin [26].

- **Digital light processing (DLP)**
  The manufacturing process of digital light processing is very similar to that of stereolithography. However, rather than using a single-point laser source and rastering the layer point-by-point, DLP uses a projection of the whole layer, which allows curing of the whole layer at once. The light is emitted using a digital micromirror device (DMD), which consists of an array of mirrors that project light on each pixel and control the on/off state [27]. This allows for much higher speeds of production compared to SLA. Top-down or bottom-up approaches may be used [27].
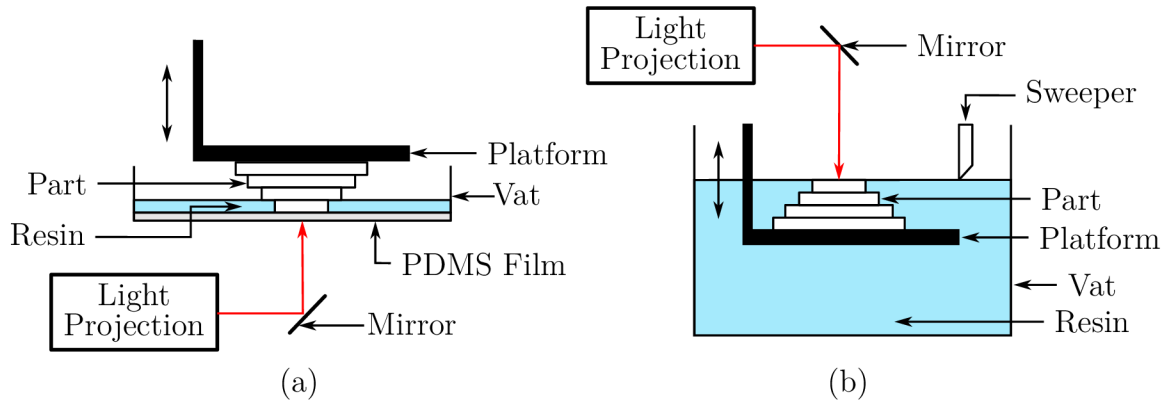
Fig. 4.9: Stereolithography printing process in a (a) bottom-up manner, (b) top-down manner consisting of a vat of polymer resin, base platform that retracts from the resin surface and light source (PDMS stands for polydimethylsiloxane) [31].

- **Continuous liquid interface production (CLIP)**
  The continuous liquid interface production process is built on digital light processing and stereolithography principles. The manufacturing process is the same as in bottom-up DLP, but instead of non-permeable plate, an oxygen-permeable one is used. Oxygen inhibits the polymerisation of the resin in the vicinity of the plate, creating a "dead zone" of resin that remains liquid even after being exposed to the light source [22]. Since recoating the cured structure with a new resin layer is the most time-consuming step, this method results in a huge increase in the manufacturing speed: up to 30 cm/h for a resolution lower than 100 μm (as opposed to an order of cm/h for DLP) [22]

- **Two-photon polymerisation (2PP)**
  Unlike the other vat photopolymerisation methods, two-photon polymerisation uses a completely different approach. It is built on the two-photon absorption process, where the resin cures only when two photons are absorbed simultaneously [27]. This happens at the focal point of a very strong laser. Subsequently, any point in the vat can be chosen to be cured without curing its surrounding resin by changing the location of the focal point of the laser in three directions [22]. 2PP offers the best resolution of all the methods listed, as features below 100 nm are common [22]. This method is widely used in the creation of metamaterial structures that require very detailed features and tunability [26; 27].

4.3 Additive manufacturing of polymer mechanical meta-materials

Of the methods mentioned for printing polymer materials, some are more common and advantageous for printing metamaterials. The PolyJet material jetting system allows the printing of resins with varying stiffness side by side, which governs the final properties of the cured material [27]. When the ratio of the different resins is changed, the properties of the material can be tailored to an extent. Auxetic metamaterials have been manufactured using inkjet printing, utilising the fact that the method allows very complicated 3D patterns and structures to be printed [26].

Selective laser sintering is common in mechanical metamaterial manufacturing. The method is simple and straightforward and suitable for a wide variety of materials, although the surface quality is lower and volume or surface defects may occur.

Similar characteristics are applicable to fused deposition modeling, where the manufacturing machines are available at lower cost, although the resolution might be lower than that for the parts manufactured by SLS. FDM methods allow a relatively easy and fast production of mechanical metamaterials where the properties depend on the structure, such as auxetic materials or materials with energy absorption [26].

Vat photopolymerisation methods are suitable for printing highly detailed small-scale structures. These high-resolution methods are limited to photosensitive resins that are cured by a light source. They have been applied in creating auxetic structures or meta-materials with enhanced mechanical properties [26; 32].

The metamaterial structure researched in the practical part of this thesis (described in Section 3.4.4) was printed using FDM. The method was chosen because of the availability of the printing machine and filament and the easy manufactuing process, since many specimens and structure models had to be printed.

5 Mechanical behaviour of polymers

5.1 Quasi-static behaviour

The elastic behaviour manifests itself in two ways. *Energy elasticity* is realised by intermolecular forces between individual chain molecules, which hold the structure in its original shape until it is overcame by external loading. Since there are more possibilities for folded molecules than for straight molecules, the thermodynamic force drives the molecules to curl and entangle back after loading, resulting in higher entropy. This is called *entropy elasticity* [33].

In amorphous polymers, the chains untangle and arrange in the direction of the load, where they further stretch (Fig. 5.1(i)) [33]. In semi-crystalline polymers, the deformation mechanisms of the amorphous regions are *interlammelar slip, interlammelar separation* and *stack rotation* (Fig. 5.1 (ii)-(b),(c)) [34]. The deformation of the crystalline regions is achieved by crystalographic slip. The slippage of the crystals results in their separation into blocks and, when further loaded, the formation of fibrils (Fig. 5.1(ii)-(d),(e)).
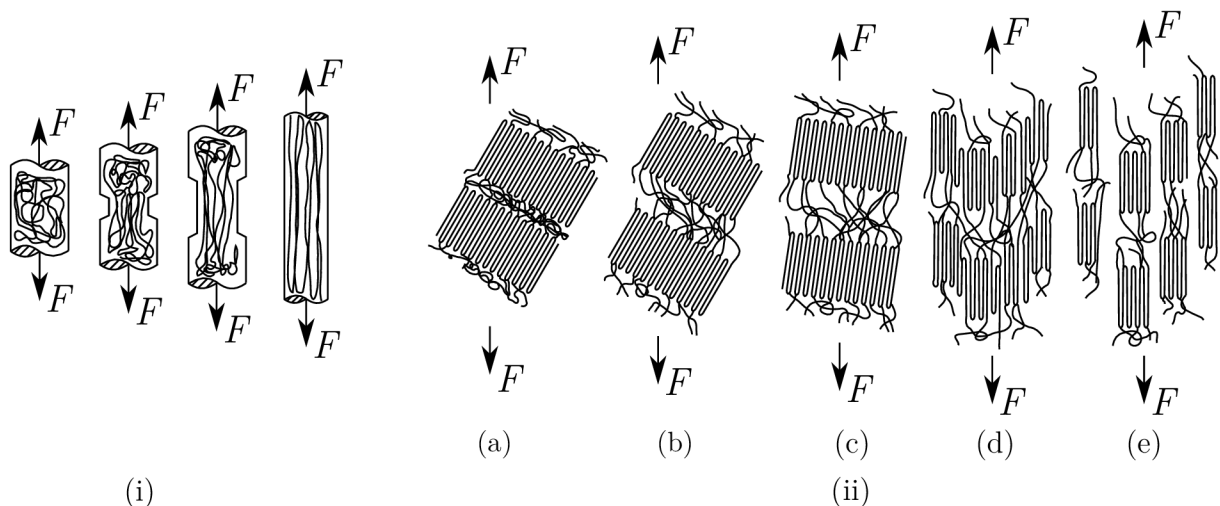
Fig. 5.1: Tensile behaviour of (i) amorphous polymers, (ii) semi-crystalline polymers where (a) is the initial stage, (b) represents the lengthening of amorphous regions, (c) the rearrangement of crystalline regions, (d) the separations into blocks, and (e) the formation of microscopic fibres (microfibrils) [33].

5.1.1 Viscoelastic behaviour

Polymer materials exhibit the behaviour of solids, as well as liquids. This is because the materials deform gradually as the chain molecules unravel over time. The response of the material depends on factors such as loading speed, temperature, or environment. The two main features of viscoelastic behaviour are *creep* and *stress relaxation*. Creep is the plastic flow of material loaded with constant stress (Fig. 5.2(a)). Stress relaxation is the decrease of stress over time while strain is kept constant (Fig. 5.2 (b)) [15].
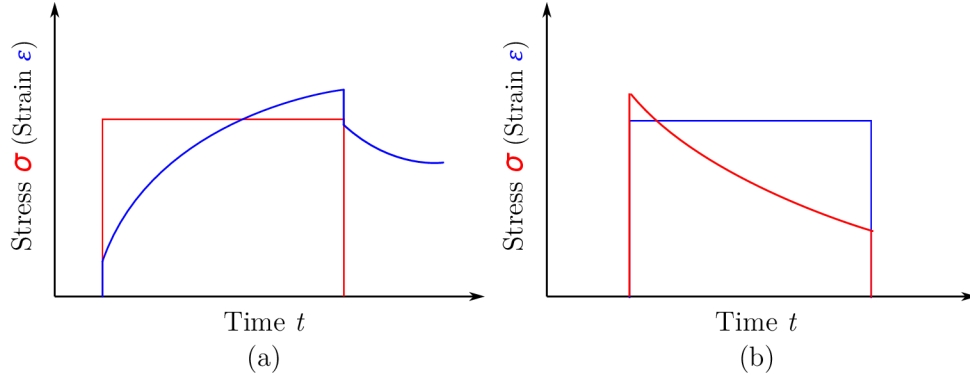
31

Fig. 5.2: Viscoelastic behaviour of polymers: (a) creep, (b) stress relaxation [35].

5.2 Fatigue behaviour of polymers

Fatigue is a damage process that occurs when the material is subjected to repeated alternating stress (e.g. mechanical, thermal) [16]. Failure occurs after a number of cycles depending on the material properties, loading conditions, and loading intensity. It is important to investigate the fatigue behaviour of a material, as parts can fail at much lower stresses when subjected to cyclic loading, compared to monotonic loading.

Fatigue of metals has been researched since 1837 and Wöhler's work on coach axles formulated fatigue principles used to this day [36]. Cyclic loading can be graphically described by a sinusoidal wave (Fig. 5.3(a)). This load can be controlled by stress or strain (a further description will consider stress-controlled fatigue; however, strain-controlled fatigue has analogous principles). A cycle is defined by its mean stress σ_m, amplitude σ_a, and R-ratio calculated as

$$R = \frac{\sigma_{min}}{\sigma_{max}}, \tag{5.1}$$

defining the loading conditions. During one cycle, the material undergoes the full loading scheme consisting of reaching the maximum stress σ_{max}, decreasing until the minimum stress σ_{min} and returning to the initial value of the mean stress σ_m. The stress-strain plane is used to plot the values during one cycle creating the hysteresis loop (Fig. 5.3(b)), which describes the material behaviour within each cycle. This allows the quantification of elastic and plastic strains within one cycle.
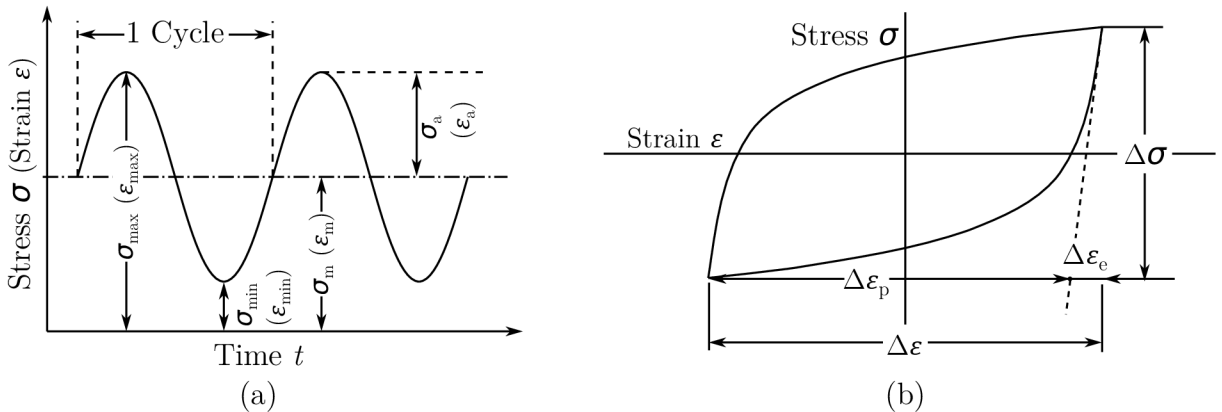

Fig. 5.3: (a) Schematic illustration of cyclic loading in time. (b) Hysteresis loop [16].

32

Fatigue can be divided into low-cycle and high-cycle regimes. In low-cycle fatigue, significant plastic strain is present and the yield stress is exceeded during loading. High-cycle fatigue is the subject of the practical section of this work, so it will be described in more detail.

The most common way to describe high-cycle fatigue are Wöhler curves (Fig. 5.4), also called S-N curves, that can be described by equation

$$\sigma_{\mathrm{a}} = A \cdot N_{\mathrm{f}}^{B}, \tag{5.2}$$

where σ_{a} is the stress amplitude, N_{f} is the number of cycles to failure and A and B are material parameters. An endurance limit σ_{e} can be denoted for most engineering materials. When a given material is subjected to cyclic loading with amplitude lower than the endurance limit, the accumulated damage is too low to cause the material to fail and the material will reach the so-called "infinite life".
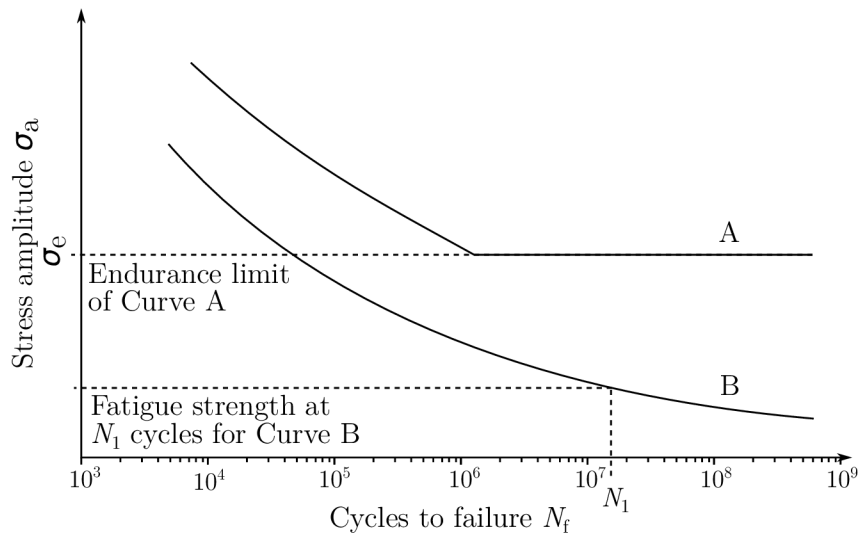
Fig. 5.4: Wöhler (S-N) curve with (A) and without (B) endurance limit [16].

The microstructure of polymers consists of long entangled polymer chains. When subjected to cyclic loading, these chains behave differently from crystalline metallic structures. The two mechanisms of fatigue damage recognised and used in the literature are self-heating (thermal) fatigue failure and mechanical fatigue failure [15; 37; 38; 39].

5.2.1 Self-heating fatigue failure

Self-heating governs the fatigue failure when loading conditions lead to a severe increase in the material temperature. The viscoelastic nature of polymers induces energy dissipation in the form of heat during loading [40]. If the conditions are set up in a way that the heat transfer from the material to its surroundings levels up with the heat produced within, the material reaches the so-called "thermal equilibrium" after a certain temperature increase and stabilises at this temperature (Fig. 5.5 ▼– ▽). Mechanical properties are altered by this increase, but the fatigue failure mechanism is mechanical (see Section 5.2.2).

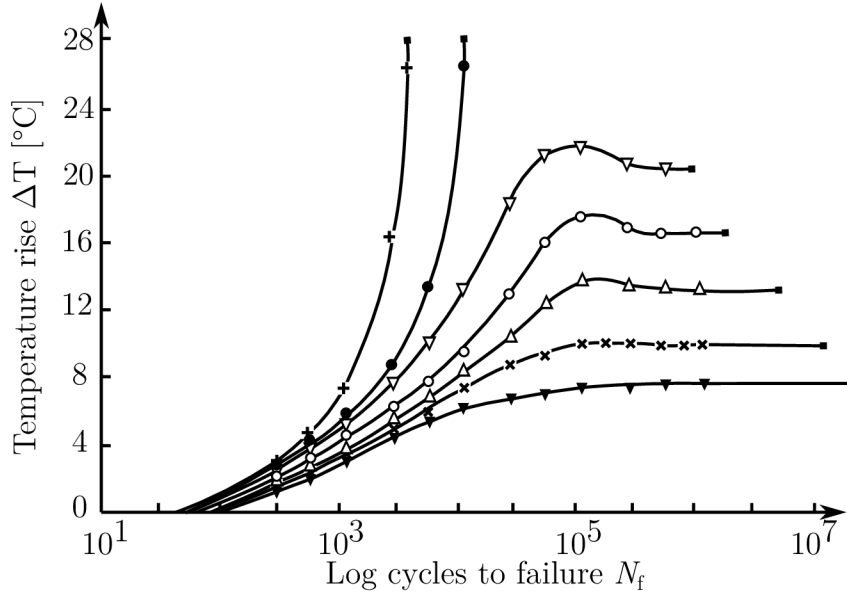Fig. 5.5: Temperature rise during uniaxial cycling of polyacetal at $R = -1$, $f = 5$ Hz for stress amplitudes σ_a ▼: 15.0, ×: 16.0, △: 17.4, ○: 19.7, ▽: 21.6, ●: 22.4, +: 27.8 MPa [38].

However, when loading creates more heat than the amount of heat transferred to the surrounding environment, thermal equilibrium is not reached and the temperature of the material increases until the properties of the material degrade so much that the material cannot withstand the load and fails (Fig. 5.5 ●,+) [37]. In this case, the failure is caused by excessive *self-heating* (also called *thermal fatigue failure*). The failure mechanism depends not only on the amplitude of the stress, but also on the loading frequency, where increasing the frequency increases the risk of overheating, as the material does not have enough time to transfer heat to its surroundings. This effect of frequency is portrayed in Fig. 5.6. Tensile mean stress reduces the allowable stress amplitude to reach thermal equilibrium, specimen geometry, internal friction, and the heat capacity of the material influence the speed of heat transfer [37; 38; 40; 41].
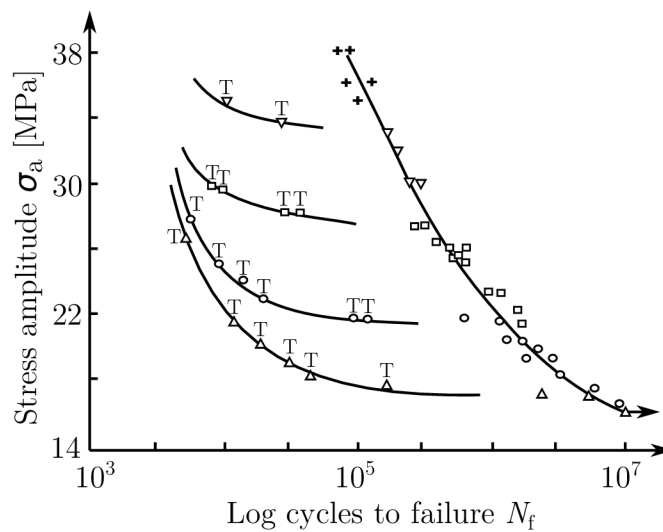
Fig. 5.6: S-N curves of acetal depending on the loading frequency for frequencies f +: 0.167, ▽: 0.5, □: 1.67, ○: 5.0, △: 10.0 Hz [38]. T marks a failure caused by self-heating.

5.2.2 Mechanical fatigue failure

Mechanical fatigue failure represents the "conventional" fatigue behaviour known from metallic materials. The fatigue process has three distinct stages [16]:

1. Crack initiation
2. Crack propagation
3. Final fracture.

A fatigue crack usually initiates in an area of localised plastic deformation or a surface craze, developed due to defects in the part or stress concentration sites [41]. These may be fabrication defects or geometry features in which localised plastic deformation develops. Two mechanisms of polymer failure are **crazing** and **shear yielding** [42].

Craze develops as a result of the untangling and elongation of polymer chains. This mechanism is accompanied by an increase in volume due to voiding of the material [42]. In areas of stress concentration, the material develops a zone of localised stress, where the craze develops. Crazing begins with the formation of microvoids in amorphous interspherulitic regions, as the intermolecular bonds within them are weaker than those within spherulite lammelae [37; 43]. Crazes grow normal to the principal tensile stress. The spherulites in the bulk material around voids bisect into lammelae, whose chains elongate and create one-directionally orientated fibrils. With further load, these fibrils continue to stretch until they break, resulting in crack formation [37; 44]. The schematic of the craze and crack is shown in Fig. 5.7. Repetition of the described process propagates the formed crack. Once the crack reaches a critical length and the ligament cannot withstand the load, the final fracture of the part occurs. The craze is not an area of fractured material, as the fibres still have some bearing capacity [37; 44]. Crazing was initially reported for amorphous polymers only; however, further research has shown that crazing mechanisms occur in semi-crystalline polymers as well [42].
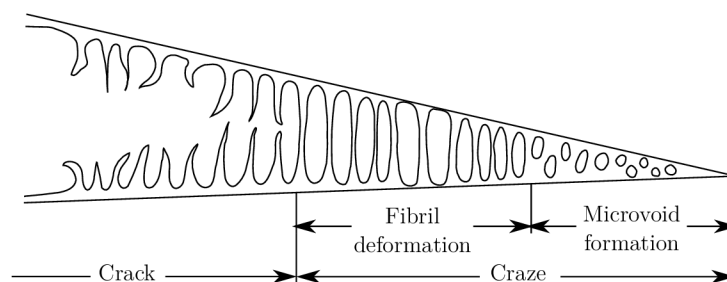

Fig. 5.7: Craze and crack formation [37].

Shear yielding is an intensive plastic deformation of the material mass in the form of shear bands. Shear bands (Fig. 5.8) are localised deformation zones that propagate along the shear planes [37]. The creation of shear bands is not accompanied by any volume change, which means that this mechanism alone does not produce any internal surfaces or cracks [42]. Cracks have been reported to start in several possible ways [45]. Cracks can initiate by voiding at the intersections of shear bands, where the highly strained fibrils of one shear band are further stretched in another direction by another shear band, resulting in disentanglement or scission of the polymer chain, nucleating the crack. Coarse

microshear bands can slide on each other and create fibrous sheets that are prone to cracking under tensile load. However, voiding of material at shear band intersections can also form a craze. If the shearing is highly localised around the crack tip, the crack will propagate and result in a brittle fracture. If the shear yielding is relatively homogenous, the polymer hardens and ductile failure occurs [37; 45].
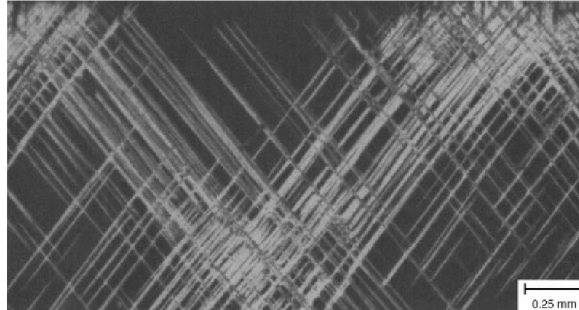

Fig. 5.8: Shear bands in polystyrene [37].

Whether the crazing or yielding mechanism prevails is a subject of many variables. The material properties and cross-linking, the applied load, and the testing temperature all influence the failure mechanism present. At very high and very low temperatures, crazing will occur by disentanglement and scission, respectively. Increasing the thickness of the specimen results in plane strain conditions, which favour craze creation. Higher chain entanglement, high molecular mass, and short chain branching with reduced crystallinity promote the shear yielding mechanism [42]. The two mechanisms can also occur simultaneously, creating the so-called "epsilon plastic zone" consisting of a leading craze and a pair of shear bands [46].

5.3 Fatigue lifetime estimation criteria

Two well-established approaches for fatigue lifetime estimations are adapted from metals. The concept of Wöhler curves [47] has been used extensively over the years. Abdelkader et al. [48] measured the Wöhler curve of high-density polyethylene. Bernasconi et al. [49] investigated the effect of fibre orientation in short glass fibre reinforced polyamide-6 through Wöhler curves. If the failure mechanism is through crack growth, the concepts of fracture mechanics can be applied as described by Moore, Pavan, and Williams [50]. Arbeiter et al. [51] measured the fracture mechanics properties of PLA additively manufactured specimens.

When considering multiaxial fatigue, the failure mechanisms are more complex and various criteria have been presented to predict the lifetime. Wang et al. [8] applied four criteria used for the metallic materials: Fatemi – Socie (shear strain-based critical plane), Smith – Watson – Topper (SWT) criterion (tensile strain-based critical plane), Chen – Xu – Huang criterion (combined energy density and critical plane), and modified SWT criterion on experimental data of PEEK in different loading paths, and found some of them to be applicable for the semi-crystalline polymer. The principal stress criterion, the von Mises criterion, and the energetic criterion were applied to reinforced polybutylene and

polyethylene mix PBT-PET GF30 and reinforced polyamide PA66 GF35 by Klimkeit et al. [52].

In the following sections, criteria chosen for estimating the fatigue lifetime of the polymer metamaterial structure in the practical part of the thesis are presented. The first principal stress criterion and the von Mises criterion were chosen because of their simplicity and applicability with minimum required material parameters. A criterion proposed by Berrehili et al. [53] has been successfully used to estimate the lifetime of high-density polyethylene (HDPE) subjected to multiaxial loading. A criterion by Nitta et al. [54] was proposed to assess the lifetime of 304 stainless steel. However; the approach is generic, and its application to polymer materials can show its transferability to these materials. Furthermore, all chosen criteria require data that can be obtained by testing the available specimens.

5.3.1   First principal stress criterion

The basic assumption of the first principal stress is that fatigue is governed by the first (maximum) principal stress [52]. The crack initiates in the location of the highest value of the first principal stress and grows perpendicularly to its direction. The amplitude of the principal stress over one cycle is used. The criterion can be written as follows:

$$\sigma_{\text{eq}} = \sigma_{1,\text{a}} = \sigma_{\text{f}} \cdot N_{\text{f}}^{-1/m}, \tag{5.3}$$

where the equivalent stress σ_{eq} equals the amplitude of the first principal stress at the investigated location $\sigma_{1,\text{a}}$. N_{f} is the estimated number of cycles to failure. σ_{f} and m are material parameters identified from the Wöhler curve of the material. The values of the stress amplitudes for the lifetime prediction of the metamaterial structure will be obtained from numerical simulations of the structure.

5.3.2   von Mises criterion

Analogously to the principal stress criterion, the von Mises criterion is also based on a Wöhler curve equation. Instead of using the first principal stress as the equivalent stress, von Mises stress is considered the governing mechanical parameter for fatigue damage [52]. Using its amplitude over one cycle, the criterion can be written as

$$\sigma_{\text{eq}} = \sigma_{\text{a,vM}} = \sigma_{\text{f}} \cdot N_{\text{f}}^{-1/m}, \tag{5.4}$$

where $\sigma_{\text{a,vM}}$ is the amplitude of von Mises stress at the critical location and N_{f} is the estimated number of cycles to failure. σ_{f} and m are material parameters derived from the Wöhler curve of the material.

5.3.3 Berrehili et al. second invariant criterion

Berrehili et al. [53] proposed a criterion that utilises the second invariant of the deviatoric stress tensor $\mathcal{J}_2$, which provides information about shear and accounts for the influence of mean stress. The criterion is based on the von Mises criterion with additional terms considering the second invariant of the stress tensor. The criterion can be expressed as follows:

$$\sigma_{\text{eq}} = \sqrt{\mathcal{J}_{2,\text{max}} + \alpha \cdot \mathcal{J}_{2,\text{m}}} \leq \beta + \frac{A}{N_{\text{f}}^c}, \tag{5.5}$$

where α, β, A, and c are parameters. This criterion requires two Wöhler curves of the material. Wöhler curve in fully reversed loading at $R = -1$, for which $\mathcal{J}_{2,\text{m}}$ is zero, allows identification of parameters β, A, and c. These can be fitted using the right-hand side of the equation. α can be identified from a Wöhler curve in pulsating tension, $R = 0.1$ is used in the practical part of the thesis.

5.3.4 Nitta et al. strain energy density criterion

Nitta et al. [54] presented a criterion that uses parameters based on the strain energy density W to calculate the fatigue lifetime. This criterion has different formulations depending on the crack mode and loading type. In this thesis, the proportional loading and crack propagation in Mode 1 (opening mode) are considered. Thus, the criterion can be written as follows:

$$\Delta W_I = \frac{\Delta \sigma_1}{2} \cdot \Delta \varepsilon_1 = A_1 \cdot N_{\text{f}}^{-\beta_1}, \tag{5.6}$$

where A_1 and β_1 are material parameters that can be obtained from the Wöhler curve of the material. $\Delta \sigma_1$ and $\Delta \varepsilon_1$ denote the range of the first principal stress and the first principal strain, respectively.

6 Problem-solution approach

As stated in chapter 2, the aim of this work is to predict the fatigue lifetime of the proposed metamaterial structure. Fig. 6.1 shows schematics of the sequence of tasks and the procedures used to obtain the fatigue lifetime estimation.
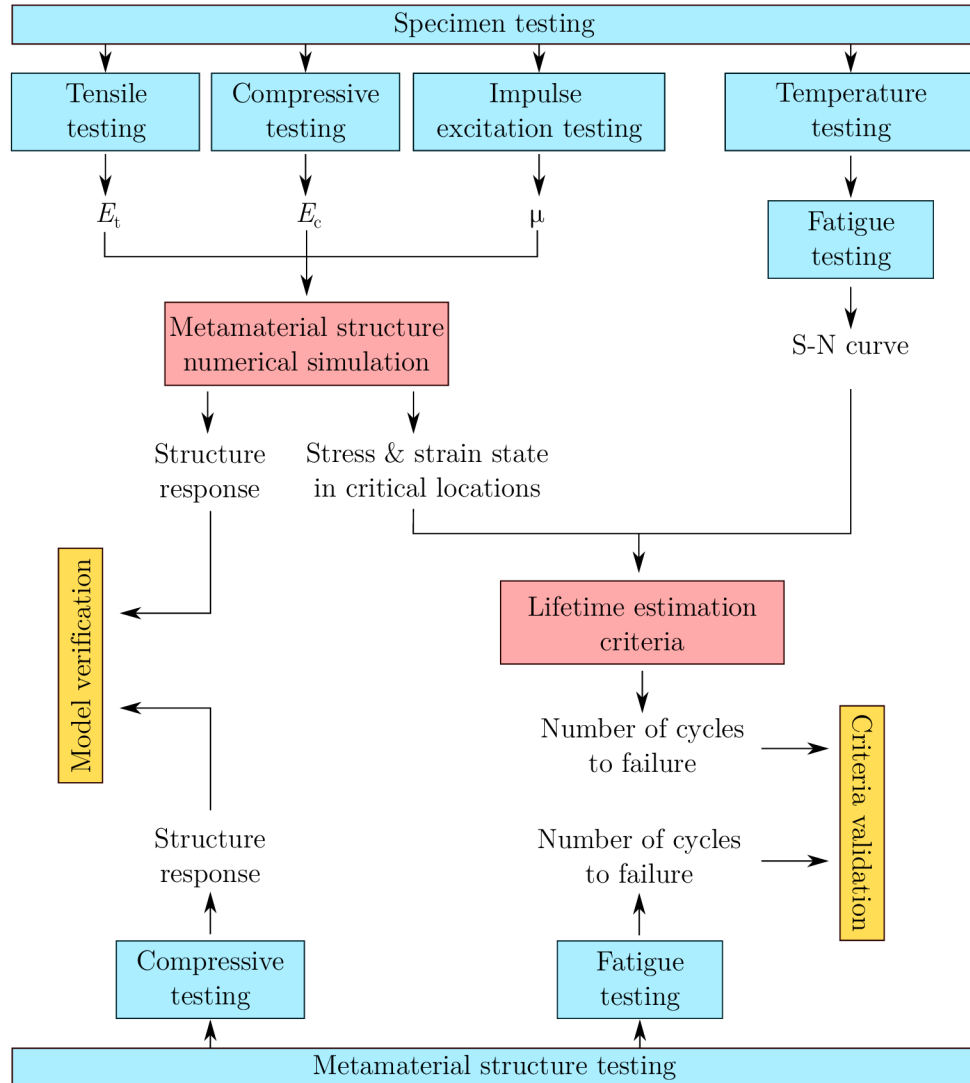
Fig. 6.1: Schematics of the workflow to obtain fatigue lifetime prediction. Laboratory testing is indicted in blue, calculations in red. Obtained parameters are blank, where E_t and E_c are elastic moduli in tension and compression, respectively, and μ is Poisson's ratio. Yellow are verification and validation procedures.

Microsoft Excel [55] and MATLAB R2022a [56] were used for data analysis, numerical simulations were performed in the ANSYS 2023 R2 [57] and 2024 R1 [58] software in Workbench and Classic environments (programming language APDL - Ansys Parametric Design Language was used in the Classic environment).

7 Experimental testing of the material

The proposed metamaterial structure is manufactured from (PA12) filament by FDM. PA12 is one of a few relevant filaments for engineering applications with FDM. It has good tensile strength, impact strength, and fatigue endurance. It is chemically and thermally stable and exhibits high UV resistance [18]. Furthermore, PA12 is a commonly used material for SLS, allowing a comparison of the manufacturing methods in future research.

Additive manufacturing influences the mechanical properties of the manufactured parts. Instead of using the properties of the filament material, laboratory tests of 3D printed specimens were conducted to assess the required model of material. All additively manufactured specimens and structures were sourced from the Polymer Competence Center Leoben (PCCL), where they were printed using printer Qidi X-Max.

7.1 Tensile testing

Dogbone specimens were made from PA12 with the same printing settings as the metamaterial structure. The layered nature of FDM influences the behaviour; therefore, specimens were manufactured in six groups of different printing orientations for comparison. These are flat 90°/90°, flat 0°/0°, flat 0°/90°, flat 45°/135°, upright 0°/90°, and upright 45°/135° (Fig. 7.1(b)). The dimensions of the dogbone samples (Fig. 7.1(a)) are set according to the ASTM D638-2022 standard [59].

The tensile test was used to measure the tensile elastic modulus E_t. The test was carried out according to the ASTM D638-2022 standard with a test speed of 5 mm/min. Multiple specimens from each printing orientation group were tested using an INSTRON E3000 computer-controlled testing machine. A diplacement gage was used to measure the diplacement.

Data from all curves within one group were averaged in one curve using linear interpolation (Fig. 7.2(a)), recalculated to true values, and the tensile elastic modulus E_t was calculated according to the ISO 527-1:2019 standard [60] using the formula

$$E_t = \frac{\sigma_{ii} - \sigma_i}{\varepsilon_{ii} - \varepsilon_i},\tag{7.1}$$

where σ_i is the stress measured at the strain value $\varepsilon_i = 0.0005$ and σ_i is the stress measured at the strain value $\varepsilon_{ii} = 0.0025$. The comparison of the measured tensile elastic modulus of each printing orientation group is shown in Fig. 7.2(b). Flat printed orientations exhibit comparable modulus values. However, upright printing orientations exhibit much lower values of the modulus.

7.2 Compressive testing

Block specimens for compressive testing were printed in the four different flat printing orientations. The methodology of compressive testing of plastics and specimen dimensions
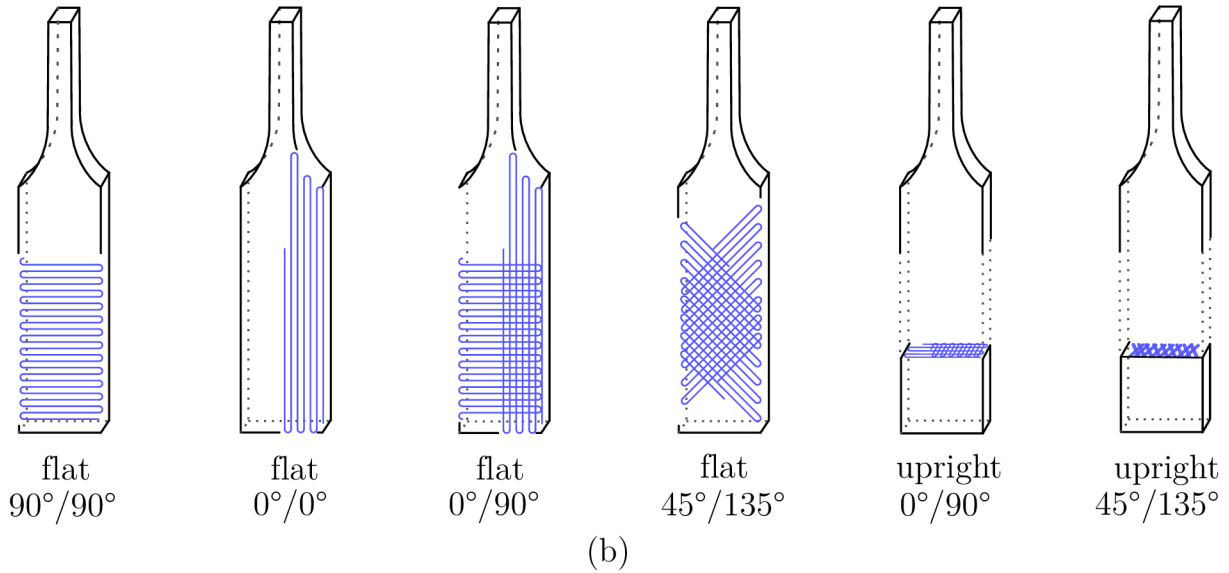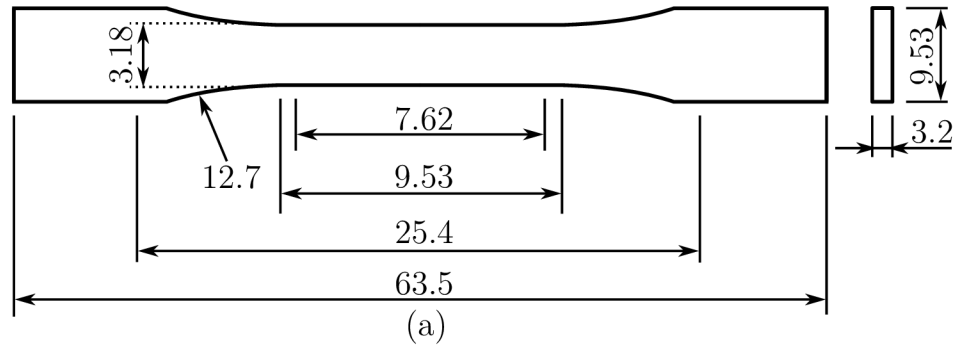
Fig. 7.1: (a) Dimensions of the used dogbone samples, (b) Groups of dogbone specimens based on printing orientation.
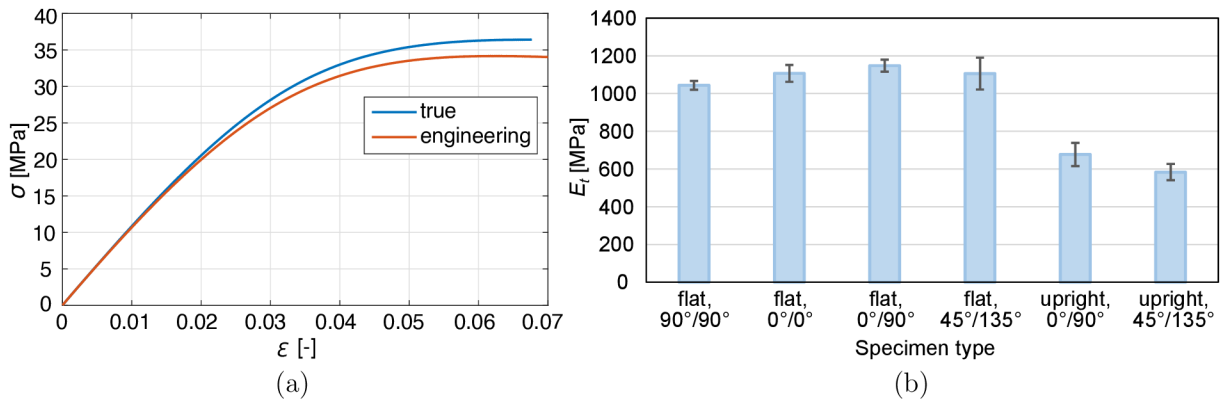

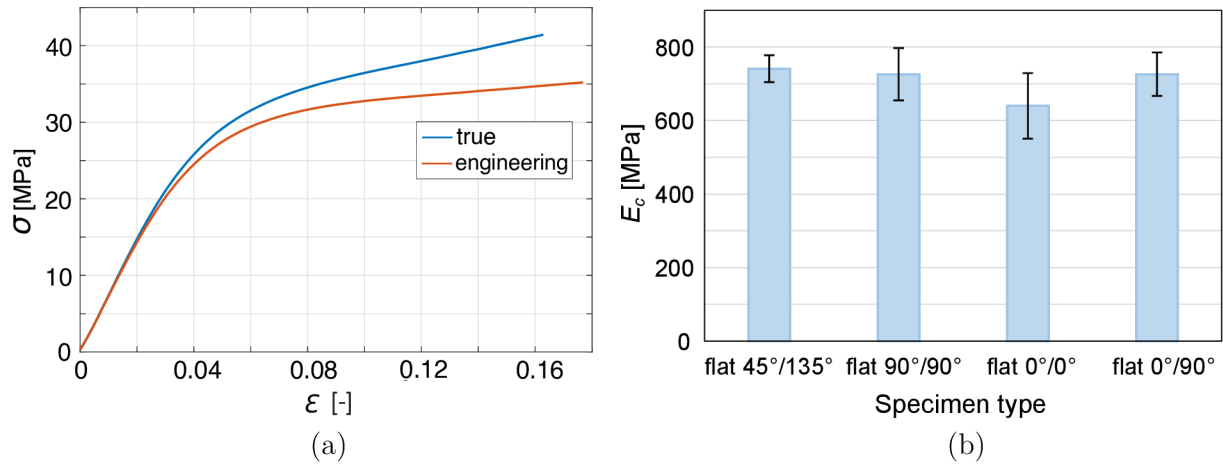Fig. 7.2: (a) Average engineering and true tensile stress–strain curve for flat 0°/0° specimens, (b) Mean values and standard deviations of tensile elasic modulus for individual printing orientation groups.

(10 x 4 x 10 mm) are dictated by the ISO 604:2002 standard [61].

Given that polymers can exhibit different behaviours under tension and compression, compression tests were conducted to capture any differences in behaviour and obtain the correct compressive modulus of elasticity E_c. The testing followed the ISO 604:2002 standard with a test speed of 1 mm/min. Several specimens of each group were tested.

Data were processed in the same way as for the tensile testing mentioned in Section 7.1, giving a resulting compressive elastic modulus E_c.

A representative average compression curve for flat printed 0°/0° specimens is shown in Fig. 7.3(a); the values of the compressive modulus for each tested group are shown in Fig. 7.3(b). The printing orientation groups are again comparable, with the flat 0°/0° orientation showing a slightly lower value. Compressive testing of the block specimens was conducted at the PCCL.

Fig. 7.3: (a) Average engineering and true compressive stress–strain curve for flat 0°/0° specimens, (b) Mean values and standard deviations of compressive elasic modulus for individual printing orientation groups.

7.3 Impulse excitation testing

Impulse excitation testing was used for measurement of the Poisson's ratio of the flat 0°/0° specimens. The test followed the ASTM E1876-22 standard [62] and used thin block specimens with dimensions 50 x 15 x 1 mm. The experiment was carried out by IPM colleagues on an IMCE HT1600 test machine with the data processed in RFDA Professional software.

Multiple specimens were tested and the averaged Poisson's ratio of the measured flat 0°/0° printed material is $\mu = 0.43$. This value corresponds to results from literature [63; 64].

7.4 Fatigue testing

ASTM7791-22 standard [65] was followed for the fatigue testing of the material. Dogbone samples described in Section 7.1 were used for the testing, as the specimens required by the standards are identical. The tests were performed using an INSTRON E10000 electrodynamic testing machine.

The standard prescribes a test frequency between 1-25 Hz. However, as discussed in Section 5.2.1, polymers can suffer a significant temperature increase during cyclic loading leading to failure due to self-heating. Temperature measurements were taken for the flat 0°/0° printed specimens at loading frequencies 5, 10, and 15 Hz at an R-ratio of 0.1

and loading amplitudes 2, 4, 6, 8, and 10 MPa. The tests showed that the PA12 material used is not highly sensitive to the loading frequency within the investigated range and the applied load. The temperature testing graphs are shown in Appendix A.

Therefore, a test frequency of 10 Hz was chosen as a sufficient compromise between the testing time and the increase in the material temperature. Cyclic loading with R-ratio $R = 0.1$ was applied. The infinite life of the dogbone specimens was considered to be $N_{\text{f,limit}} = 10^6$ cycles. Wöhler curves were measured for each printing direction group and are plotted in Fig. 7.4. Similarly to tensile behaviour, significantly worse fatigue endurance can be observed in the upright printing direction groups.
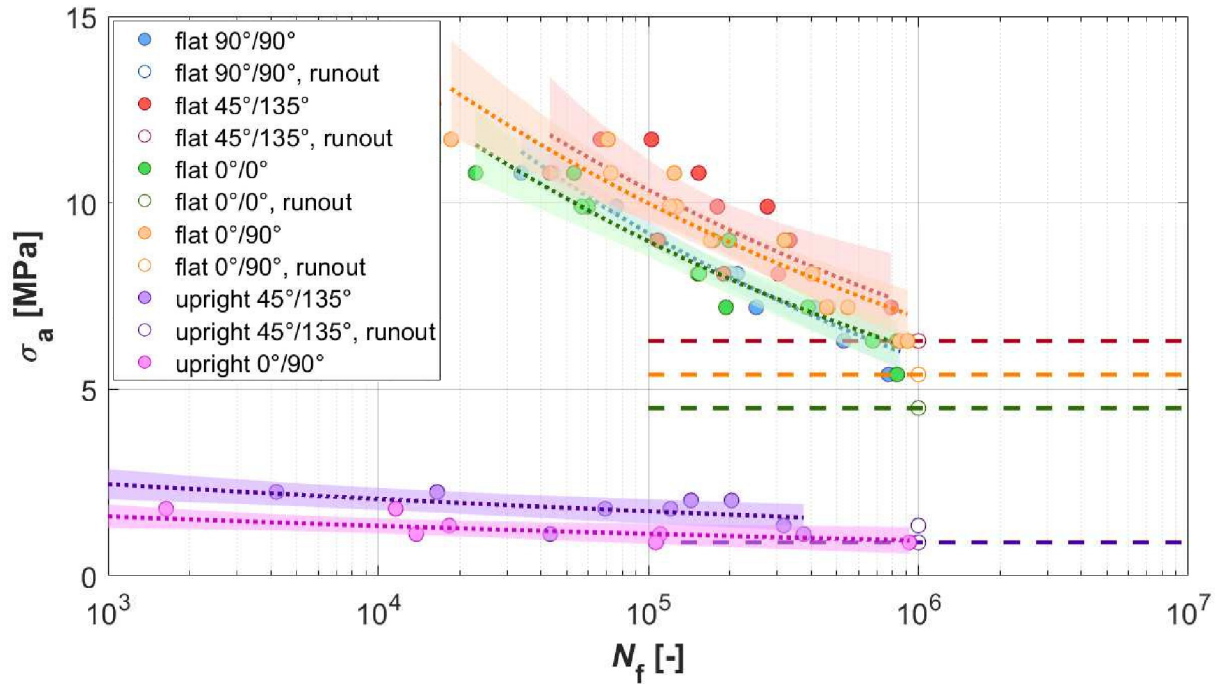
Fig. 7.4: Wöhler curves of the respective groups of dogbone specimens tested at $f = 10$ Hz and $R = 0.1$.

7.5   Model of material

The material parameters obtained from the testing are:

- Tensile elastic modulus E_{t}
- Compressive elastic modulus E_{c}
- Poisson's ratio μ
- Wöhler curve with the corresponding fatigue endurance limit σ_{e}.

Based on the poor performance of the upright printed specimens, avoiding this printing direction within the metamaterial structure is necessary. The absence of these printing directions can be confirmed by checking the printing orientation of the metamaterial structure (Fig. 7.5). Furthermore, by analysing the printing directions within the structure with respect to the loading conditions (marked with blue arrows in Fig. 7.5), the struts can be investigated. With the applied load, the struts experience the highest stress. The

direction of printing that best matches the struts with respect to the load is the flat 0°/0° one. The model of material will thus be created on the basis of the experimental testing of the flat 0°/0° printed specimens. Its parameters are listed in Tab. 7.1.
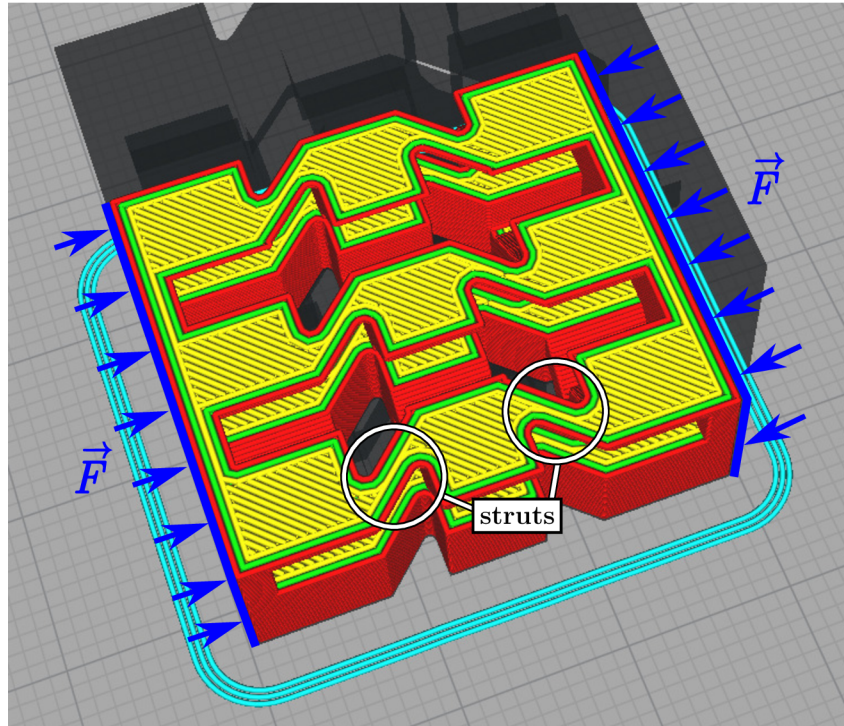
Fig. 7.5: Printing directions within a cut of the metamaterial structure and the direction of applied load.

Tab. 7.1: Measured material parameters of the flat 0°/0° 3D printed material used for creation of the model of material.

Material parameter	Value	Unit
Tensile elastic modulus E_t	1107	MPa
Poisson's ratio μ	0.43	-
Compressive elastic modulus E_c	641	MPa
Fatigue endurance limit σ_e	4,5	MPa

8 Numerical modelling

Finite element method (FEM) was used for numerical modelling of the metamaterial structure. This method allows for a detailed analysis of the stresses and deformations within the structure. In this chapter, the development of the numerical model of the structure is described with the applied loading and boundary conditions.

8.1 Model of geometry

The PCCL provided a CAD model of geometry of the full structure with 7x7x7 cubes (Fig. 8.1(a)). In order to reduce the material used for manufacturing the structures, a model reduction was desirable. Thus, a reduced structure with 3x3x3 cubes was proposed (Fig. 8.1 (b)). This structure needs to be sufficiently equivalent to the full-size structure. Therefore, the dimensions of struts and cubes were kept identical. The values of the first principal stress along the sides of the upper and lower struts of the centre cube were analysed for this assessment.
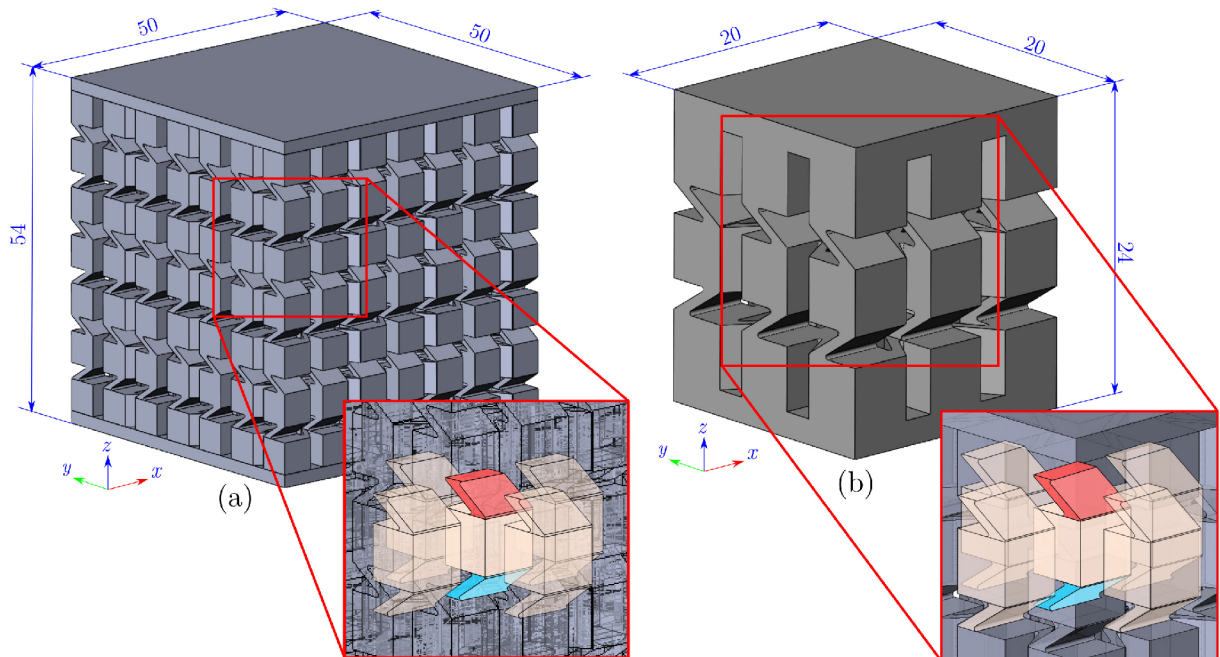
Fig. 8.1: (a) CAD model of the full-size structure, (b) proposed reduced structure model, with details of the upper (red) and lower (blue) strut of the centre cube respective for each structure.

Both structures were meshed with the same parmeters. Linear model of material was used with parameters listed in Section 7.5. Both structures were loaded by displacement causing a compressive strain of $\varepsilon = 0.01$. The first principal stress σ_1 along the outer and inner faces of the strut above and below the centre cube (as shown in Fig. 8.1) was plotted for both cases. The results are plotted in Fig. 8.2.

The stress profiles along the strut faces can be clearly compared in the plotted figures. Even though the maximum difference of the first principal stress along the strut face is ca. 30 %, the stress distribution is comparable. Thus, the full-size structure can be substituted
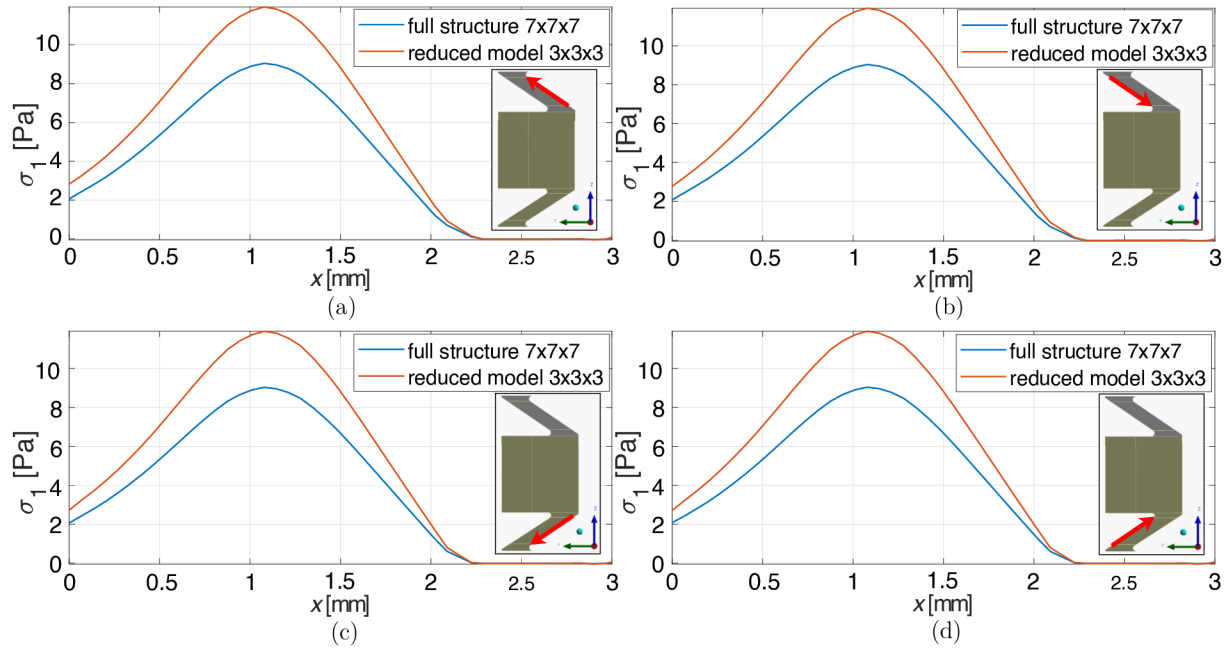
Fig. 8.2: Values of the first principal stress along the (a) outside and (b) inside face of the centre cube upper strut, and (c) outside and (d) inside face of the centre cube bottom strut.

by the reduced model. Moreover, manufacturing and computational time, as well as the consumed material, will be greatly reduced. After consultation with colleagues from PCCL, some further changes were made to the model of geometry to ensure printability of the structure by FDM. The final reduced structure, used for further experimental testing and numerical simulations, is shown in Fig. 8.3.
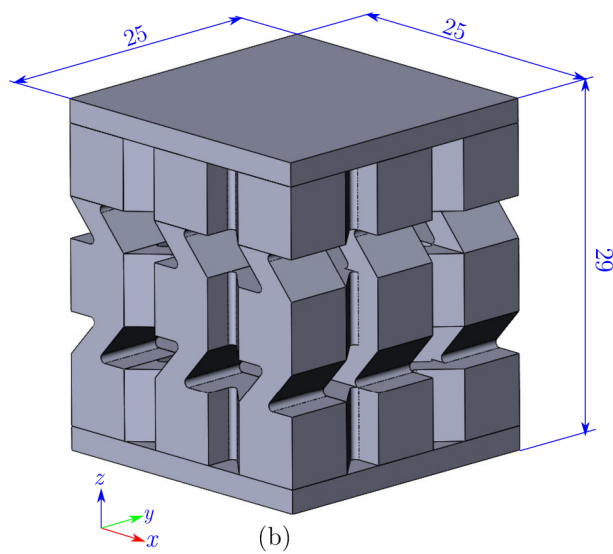
Fig. 8.3: Reduced model of the metamaterial structure with 3x3x3 cubes with altered geometry parameters for printing reasons.

8.2 Discretisation

The stresses and strains within the structure are calculated using FEM. Therefore, the model of geometry must be divided into elements, and mesh must be created. The quality of the mesh will directly affect the accuracy of the results.

The mesh was created in the Workbench interface of the ANSYS software [57]. Quadratic elements SOLID 186 and its tetrahedral form SOLID 187 were used for the entire structure to describe the evolution of the stress field along the geometry better. The geometry was separated into cubes and struts. Since struts are the main domains of interest, a regular fine mesh was created, which further refines the accuracy of the results in these locations.

8.2.1 Mesh size sensitivity analysis

To ensure the sufficiency of the created mesh, a sensitivity analysis was carried out. The effect of the element size of the struts on the maximum value of the first principal stress was investigated. The general rule of sensitivity analyses states that the results are representative once the difference between the results of an initial model and a model with doubled mesh density is less than 5%. Meshes of the three calculated cases are shown in Fig. 8.4.

(a)

(b)

(c)
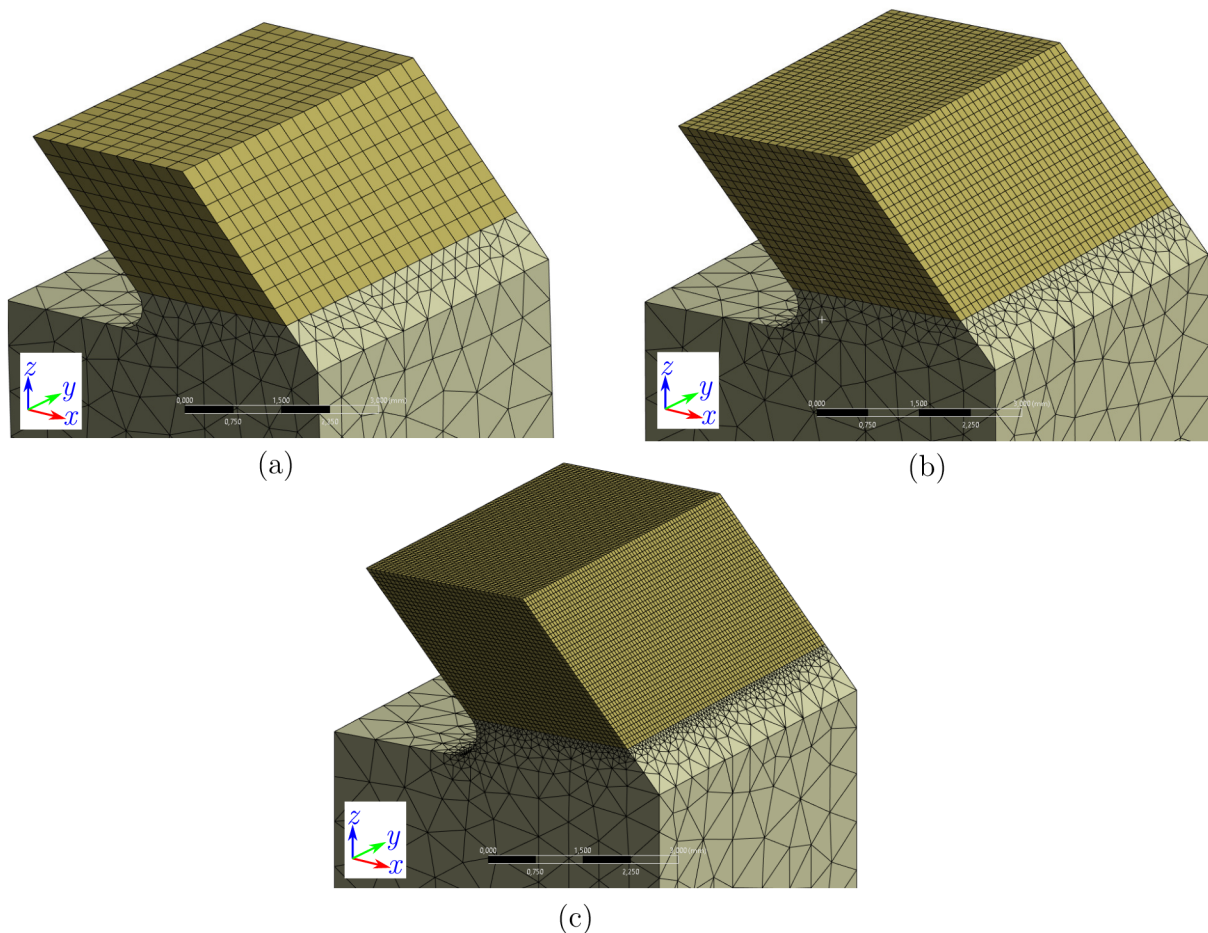
Fig. 8.4: Mesh density of the struts for a strut element size of (a) 0.3 mm, (b) 0.15 mm, (c) 0.075 mm.

47

A boudary condition of 1 mm compressive displacement of the top face was set for each case. The maximum first principal stress on the struts is the monitored solution parameter, as it is the crack opening stress. The parameters of each case including the element size, number of elements in the model, the computational time, the maximum value of the first principal stress, and the difference between cases is listed in Tab. 8.1.

Tab. 8.1: Dependence of the maximum first principal stress on the strut element size, with respective number of elements and computational time for each case.

Element size [mm]	No. of elements [-]	Runtime [hh:mm:ss]	σ_1 [MPa]	Difference [%]
0.3	346 833	00:04:10	22.775	-
0.15	987 280	00:13:50	22.354	1.86
0.075	4 730 391	01:49:00	22.284	0.29

The results show little difference between the simulated cases. The number of elements increases rapidly with decreasing element size and with that increases the computational time of the numerical simulation. The refined mesh with an element size of 0.075 mm improves the result only by 0.29 %, but the runtime increases almost eight times. As a result of this, the medium element size was chosen for further simulations.
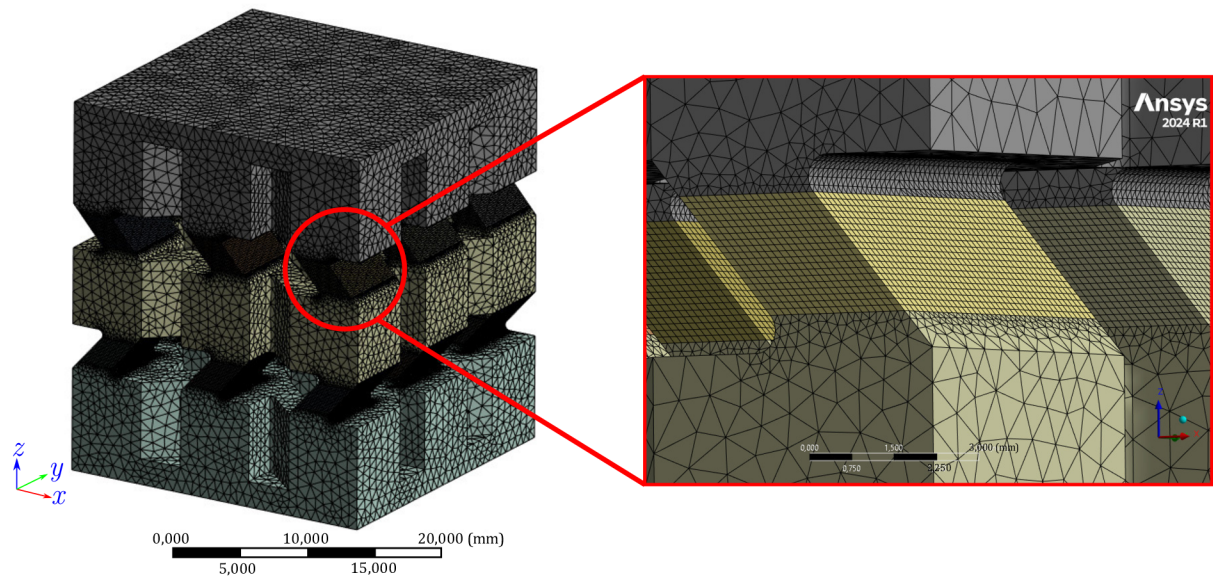
Fig. 8.5: Mesh of the entire metamaterial structure with a detailed view of the fine regular mesh on the struts.

8.3 Boundary conditions

In order to calculate the results of the stress and strain corresponding to the real loading of the structure, the loading and boundary conditions of the structure must be set correctly. The structure is loaded in compression, so the necessary boundary conditions need to represent

- The flat base the structure is located on
- The fixed rotation of the structure on the flat base
- The uniform compressive loading on the top face.

48

Further modelling was performed in the Classic interface of the ANSYS software [57]. Fig. 8.6 shows the schematics of the boundary conditions applied on the structure. To represent the flat base under the structure, the displacement of the bottom face is restricted in the z-direction. Two nodes in the centre of the bottom face are fixed to prevent rotation of the structure. Vertices on the top face are coupled together in the z-direction to model the uniform compression of the structure that would occur during the real loading.
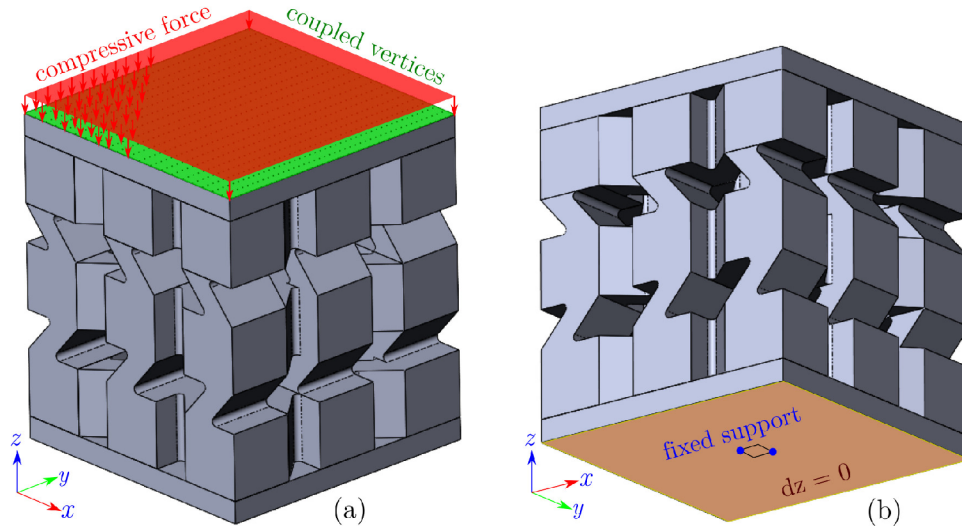
Fig. 8.6: Schematic representations of the boundary conditions applied on the top (a) and bottom (b) face consisting of force load and coupled z-displacement on the top face, and fixed support of two vertices and restricted z-displacements on the bottom face.

8.4   Tension and compression element models of material

As described in Chapter 7, the 3D printed material behaves differently in tension and compression. The numerical model thus needs to be adjusted to reflect this behaviour.

Due to inability to set different tensile and compressive properties within one model of material using ANSYS, two linear models of material were created; a model with tensile properties and a model with compressive properties. The models of material were then assigned to each element based on their response to loading. This process followed the scheme in Fig. 8.7.

First, all elements were set to the tensile model of material. The structure was then loaded, and for each element, the volumetric strain was calculated following the equation

$$\varepsilon_\mathrm{v} = \frac{\Delta V}{V} = \varepsilon_1 + \varepsilon_2 + \varepsilon_3. \tag{8.1}$$

The volumetric strain ε_v represents the change in volume of an element. In case of negative volumetric strain, the element model of material was changed to compressive. The calculation was then repeated with the resulting arrangement of elements with the respective models of material from the previous calculation, and the same process was
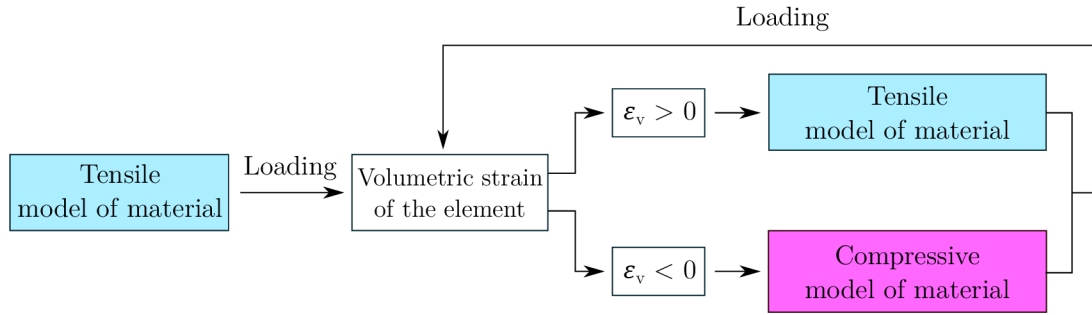
Fig. 8.7: Process of assigning the model of material to each element respective to its volumetric change.

followed. A total of 10 iterations were calculated to stabilise the response of the structure. The resulting distribution of the models of material within the structure is shown in Fig. 8.8.
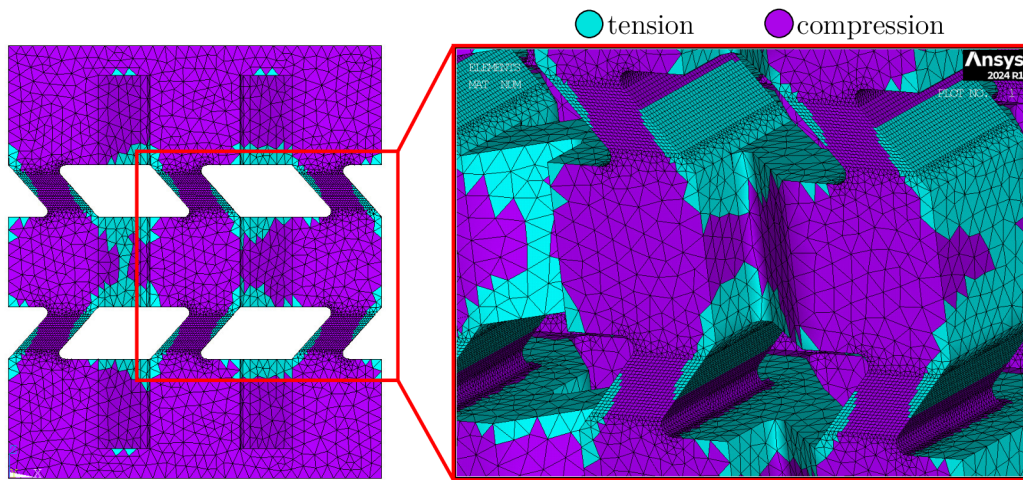
Fig. 8.8: Arrangement of elements with tensile and compressive models of material within the numerical model of the metamaterial structure.

8.5   Numerical model verification

Compressive testing of two printed structures was performed to verify the numerical model. The structures were tested at a test speed of 5 mm/min and the stress-strain curves are plotted in Fig. 8.10. The compressive testing was performed by an IPM colleague on a machine INSTRON 8862, where the displacement was measured with a displacement gage.

The measured compressive curves can be divided into three distinct regions. In the first region, until $\varepsilon_c \approx 0.04$, the functional deformation of the struts occurs (Fig. 8.9(a)). Once the struts are extensively plasticised, they lose their function, which can be observed by the plateau region of the compressive curve. In the plateau region, the failed struts are compressed until the structure is compact and behaves cohesively (Fig. 8.9(b)). After that, from $\varepsilon_c \approx 0.1$, the compact structure starts to deform (Fig. 8.9(c)).
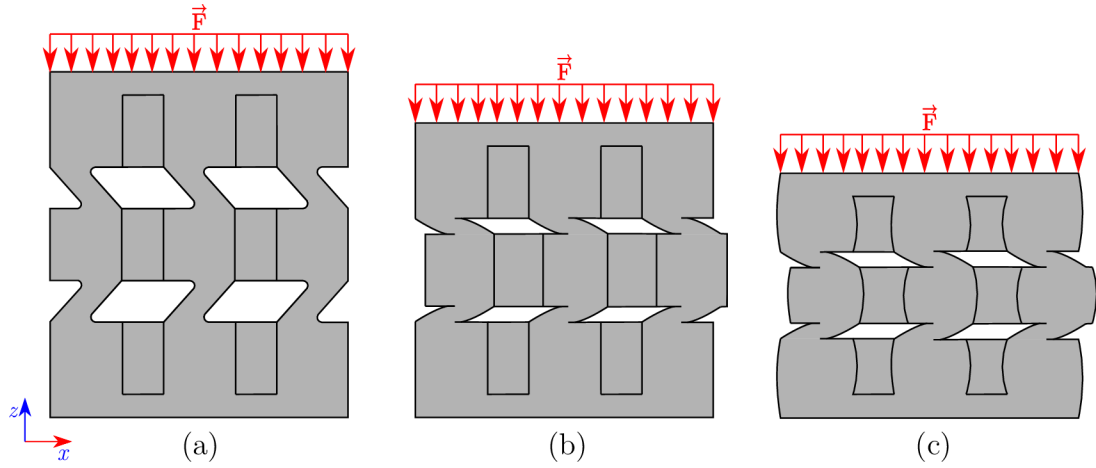
Fig. 8.9: Behaviour of the metamaterial structure under compression, (a) elastic deformation of the struts, (b) struts lose function and the structure gets compacted, (c) compacted structure deforms as one unit.

The simulation of a compressive test was performed using a deformation boundary condition. A displacement of 1 mm was applied to the coupled nodes on the top face of the structure, equal to a compressive strain of $\varepsilon_c = 0.035$. The simulation consisted of ten substeps in which the reaction force in the z direction was noted. Using this force, the pressure that needs to be applied to the top face to result in the respective strain is calculated. This dependence is plotted along the experimental curves in Fig. 8.10. The response obtained from the numerical modelling aligns well with the experimental data. This verifies the created numerical model. The fatigue lifetime will be estimated in the region of linear behaviour up to pressure magnitude ~4 MPa; therefore, the linear model of material is sufficient for further analyses.
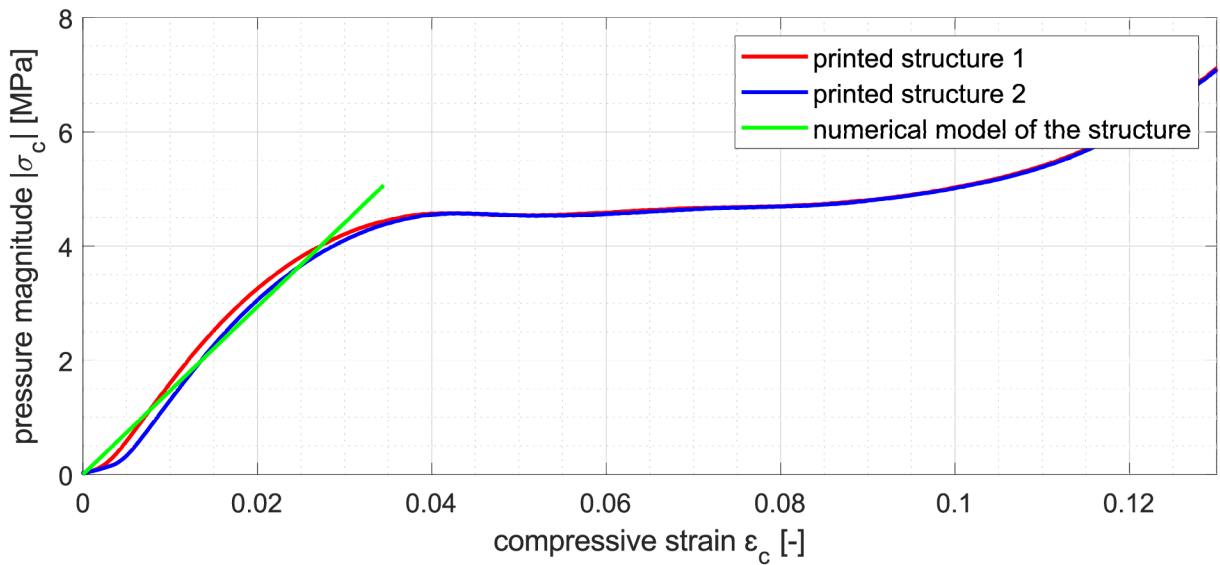
Fig. 8.10: Pressure–compressive strain curves of the tested metamaterial structures and the numerically simulated response of the structure.

8.6 Assessment of critical locations

Critical locations within the structure must be specified for the description of fatigue behaviour and the prediction of fatigue lifetime. The first principal stress was chosen as the defining parameter, as it is the crack opening stress. After loading the structure with a compressive displacement of 1 mm, the first principal stress was plotted (Fig. 8.11). As expected, the highest stress acts on the struts. Two distinct types of critical locations can be recognised: Location 1 on the vertical faces of the struts and Location 2 on the sloped faces of the struts. For these locations, the fatigue lifetimes will be estimated using criteria from the literature. The upper-centre strut will be used for these predictions, as the least stress relaxation is possible.
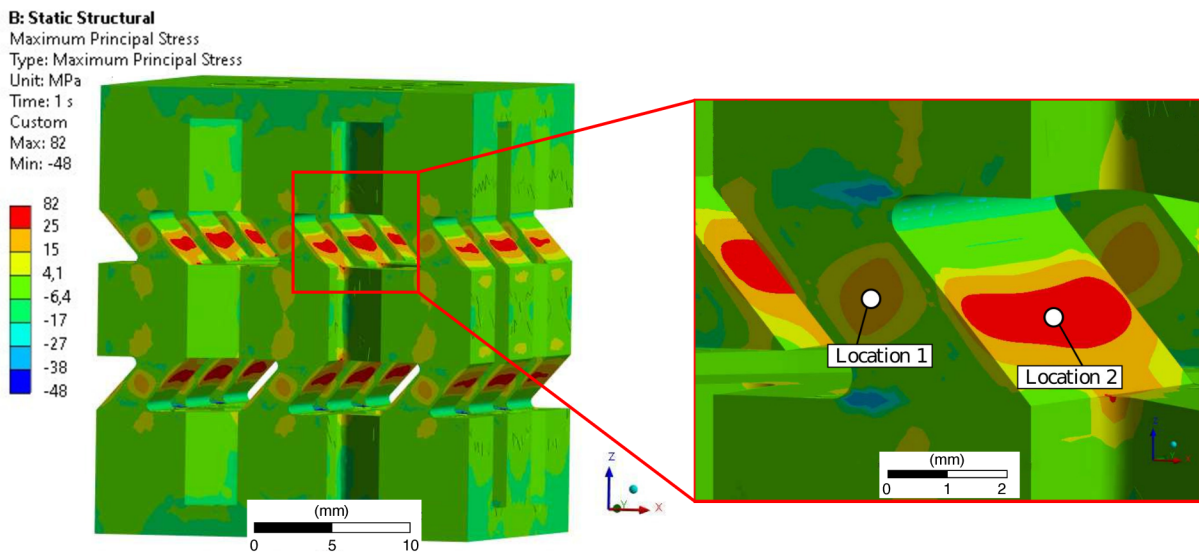
Fig. 8.11: First principal stress acting on the metamaterial structure with a detailed view of the upper-centre strut with two marked types of critical locations.

8.7 Simulation of cyclic loading

To predict fatigue lifetime using the criteria described in Section 5.3, the stress and strain conditions at the investigated locations must be known. All chosen criteria are evaluated for an amplitude of alternating stress (strain) due to the applied cyclic loading. The linearity of the system requires simulations of two loading cases in order to describe the response of the linear section of the model for any load magnitude.

To obtain the amplitude of the resulting stress (strain), the response of the structure is examined for the minimum and mean compressive forces representing a loading cycle (Fig. 8.12). Note, that the minimum compressive force results in the maximum stresses and deformations in the structure, which may be counter-intuitive. Pressure magnitudes of 4 and 3 MPa were chosen from the linear region of Fig. 8.10.

The minimum compressive force $F_{c,min}$, corresponding to the chosen stress, is calculated using the basic stress equation
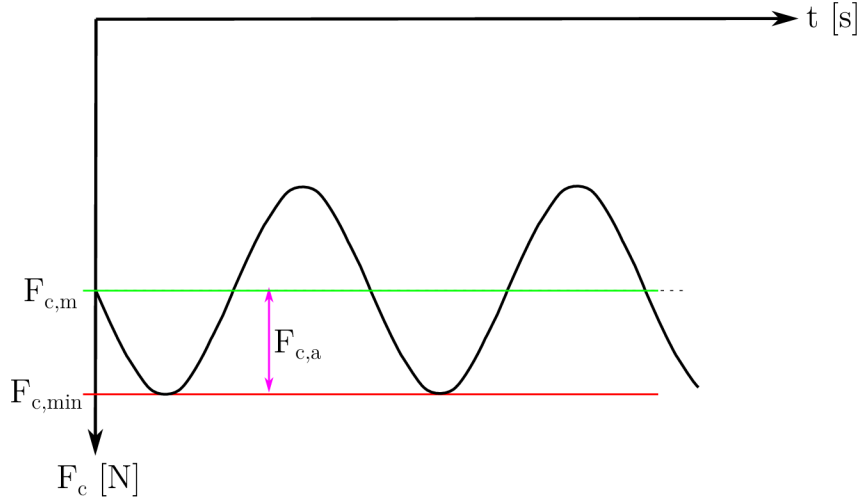
Fig. 8.12: Compressive forces representing the loading cycle for characterisation of the metamaterial structure response during cyclic loading.

$$F_{\text{c,min}} = \sigma_{\text{c}} \cdot A, \tag{8.2}$$

where σ_{c} is the applied pressure and A is the area of the top face. Using the stress asymmetry ratio R and the minimum compressive force, the mean force $F_{\text{c,m}}$ can be calculated with equation

$$F_{\text{c,m}} = \frac{F_{\text{c,min}} \cdot \left(\frac{1}{R} + 1\right)}{2}. \tag{8.3}$$

The stress asymmetry ratio R was set to be the same as in the case of fatigue testing of the 3D printed specimens described in Section 7.4. However, as the structure is loaded in compressive regime, the corresponding R-ratio is 10. Note, that the stress asymmetry ratio R at the critical locations is $R = 0.1$. Parameters $F_{\text{c,min}}$ and $F_{\text{c,m}}$ are used as load input parameters for the simulations of the structure. The amplitude of the loading force is given by a simple equation

$$F_{\text{a,c}} = |F_{\text{c,min}}| - |F_{\text{c,m}}|. \tag{8.4}$$

For each critical location and load case, stress and strain tensors are recorded in the global and principal coordinate system. Furthermore, von Mises stress is recorded at both locations for the von Mises criterion.

9 Fatigue lifetime prediction

Once all numerical calculations are performed and the stress and strain tensors and von Mises stresses are recorded, the fatigue lifetime for the two critical locations can be predicted using the four criteria discussed in Section 5.3. The respective criteria formulations are presented again for clarity.

9.1 First principal stress criterion

As discussed in Section 5.3.1, the first principal stress criterion is defined by an equation

$$\sigma_{\mathrm{eq}} = \sigma_{1,\mathrm{a}} = \sigma_{\mathrm{f}} \cdot N_{\mathrm{f}}^{-1/m}, \tag{9.1}$$

where the amplitude of the first principal stress $\sigma_{1,\mathrm{a}}$ is the equivalent stress considered. σ_{f} and m are fatigue material parameters.

The material parameters can be obtained from the Wöhler curve of the material. The model of material's parameters were established from the flat 0°/0° printing direction specimens. Therefore, the Wöhler curve used for the lifetime estimation is also of the flat 0°/0° printed specimens. The considered Wöhler curve is plotted in Fig. 9.1. The parameters σ_{f} and m are derived from the Wöhler curve, and their values are listed in Tab. 9.1.

Tab. 9.1: Fatigue material parameters of the flat 0°/0° 3D printed material.

Material parameter	Value	Unit
fatigue strength coefficient σ_{f}	74.58	MPa
fatigue lifetime exponent m	5.435	-
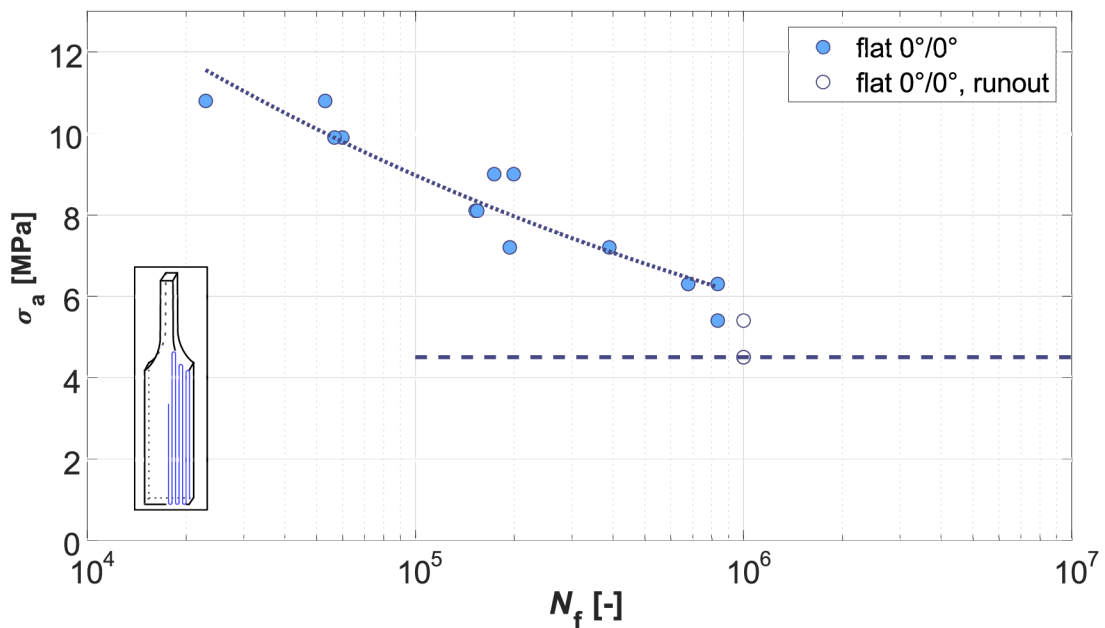
Fig. 9.1: Wöhler curve of the flat 0°/0° printed dogbone specimens.

54

The amplitude of the first principal stress at the investigated location is the last required input for this criterion. For this, the stress tensors in the principal coordinate system for forces F_{m} and F_{min} are used. The amplitude is calculated as

$$\sigma_{1,\mathrm{a}} = \sigma_{1,F_{\mathrm{min}}} - \sigma_{1,F_{\mathrm{m}}}. \tag{9.2}$$

Using these input parameters, the lifetime can be predicted for each location at both pressure levels. The formula for calculating the lifetime estimation according to the first principal stress criterion is as follows

$$N_{\mathrm{f}} = \left(\frac{\sigma_{1,F_{\mathrm{min}}} - \sigma_{1,F_{\mathrm{m}}}}{\sigma_{\mathrm{f}}} \right)^{-m}. \tag{9.3}$$

The lifetime predicted by the first principal stress criterion for both loading cases at critical location 1 (vertical face) and critical location 2 (sloped face) are listed in Tab. 9.2.

Tab. 9.2: Estimated numbers of cycles to failure at investigated locations for pressure magnitude $|\sigma_{\mathrm{c}}| = 4$ and 3 MPa according to principal stress criterion.

Pressure magnitude $|\sigma_{\mathrm{c}}|$ [MPa]	Estimated lifetime N_{f} [-]	
	Location 1	Location 2
4	172 402	46 365
3	823 301	221 414

9.2   Von Mises stress criterion

The von Mises stress criterion is analogous to the first principal stress one and was discussed in Section 5.3.2. The proposed criterion formula is defined as

$$\sigma_{\mathrm{eq}} = \sigma_{\mathrm{vM,a}} = \sigma_{\mathrm{f}} \cdot N_{\mathrm{f}}^{-1/m}, \tag{9.4}$$

where the governing stress is the von Mises stress σ_{vM} at the investigated location. Similarly to the first principal stress criterion, σ_{f} and m are fatigue material parameters derived from the Wöhler curve of the material.

The considered Wöhler curve is the same as in the previous case. Therefore, the material parameters are identical. The amplitude of the von Mises stress at a location can be calculated from the results of von Mises stress for the minimum and mean loading force obtained from numerical calculations as

$$\sigma_{\mathrm{vM,a}} = \sigma_{\mathrm{vM},F_{\mathrm{min}}} - \sigma_{\mathrm{vM},F_{\mathrm{m}}}. \tag{9.5}$$

The resulting formula for the lifetime estimation for a given location and pressure using the von Mises stress criterion follows. The predicted lifetimes at the critical locations according to the von Mises criterion are listed in Tab. 9.3.

$$N_f = \left(\frac{\sigma_{vM,F_{min}} - \sigma_{vM,F_m}}{\sigma_f} \right)^{-m} \tag{9.6}$$

Tab. 9.3: Estimated numbers of cycles to failure at investigated locations for pressure magnitude $|\sigma_c| = 4$ and 3 MPa according to von Mises stress criterion.

Pressure magnitude $|\sigma_c|$ [MPa]	Estimated lifetime N_f [-]	
	Location 1	Location 2
4	1 034	95 736
3	4 942	457 190

9.3 Berrehili et al. second invariant criterion

A more complex criterion, referred to as the second invariant criterion, was discussed in Section 5.3.3. This criterion is prescribed by a formula

$$\sigma_{eq} = \sqrt{\mathcal{J}_{2,max} + \alpha \cdot \mathcal{J}_{2,m}} \leq \beta + \frac{A}{N_f^c}, \tag{9.7}$$

where $\mathcal{J}_{2,max}$ and $\mathcal{J}_{2,m}$ are the second invariants of the deviatoric parts of the stress tensor $\mathcal{J}_2$ at minimum (the minimum force produces the maximum stress) and mean load, respectively. Parameters β, A, and c can be derived from a Wöhler curve in fully reversed loading ($R = -1$). α can be derived from a Wöhler curve in pulsating tension.

An experimentally measured Wöhler curve is available only for a stress ratio $R = 0.1$. Therefore, in order to derive the material parameters, the curve is transformed using a formula proposed by Smith, Watson and Topper [66]

$$\sigma_{a,-1} = \sqrt{\sigma_{a,0.1} \cdot (\sigma_{a,0.1} + \sigma_{m,0.1})}, \tag{9.8}$$

where $\sigma_{a,-1}$ is the load amplitude of a fully reversed cyclic load ($R = -1$), which results in damage equivalent to a load cycle in pulsating tension ($R = 0.1$) with mean stress $\sigma_{m,0.1}$ and amplitude $\sigma_{a,0.1}$. Although this formula was proposed for metals, it has been successfully used for plastics by Hutař and Trávníček [67]. The stress amplitude and the stress ratio are known, and the mean stress of the pulsating cycle is calculated from the amplitude using equation [67]

$$\sigma_{m,0.1} = \frac{1 + R}{1 - R} \cdot \sigma_{a,0.1}. \tag{9.9}$$

The second invariant of the deviatoric stress tensor $\mathcal{J}_2$ is zero for fully reversed loading. Thus, the Equation (9.7) is simplified to a form

$$\sigma_{eq} = \sqrt{\mathcal{J}_{2,max,-1}} \leq \beta + \frac{A}{N_f^c}. \tag{9.10}$$

The general formula for calculating the second invariant of the deviatoric stress tensor is [68]

$$
\begin{aligned}
\mathcal{J}_2 &= \frac{1}{6} \cdot \left[(\sigma_{11} - \sigma_{22})^2 + (\sigma_{22} - \sigma_{33})^2 + (\sigma_{33} - \sigma_{11})^2 \right] + \sigma_{12}^2 + \sigma_{23}^2 + \sigma_{31}^2 \\
&= \frac{1}{6} \cdot \left[(\sigma_1 - \sigma_2)^2 + (\sigma_2 - \sigma_3)^2 + (\sigma_3 - \sigma_1)^2 \right].
\end{aligned}
\tag{9.11}
$$

The maximum stress for a fully reversed loading equals the stress amplitude. Since the loading is uniaxial, the second invariant of the deviatoric tensor can be calculated as

$$
\mathcal{J}_{2,\mathrm{max},-1} = \frac{1}{3} \cdot \sigma_{\mathrm{a},-1}^2,
\tag{9.12}
$$

where $\sigma_{\mathrm{a},-1}$ is the load stress amplitude. With this parameter calculated for each data point, the dependence of $\sqrt{\mathcal{J}_{2,\mathrm{max}}}$ on the number of cycles to failure N can be expressed and the parameters β, A, and c determined.

Next, the parameter α can be determined using a Wöhler curve in pulsating tension. Again, the experimentally measured Wöhler curve of the flat 0°/0° printed specimens, shown in Fig. 9.1, is used. For each data point, the maximum and mean second invariant is calculated using equations

$$
\mathcal{J}_{2,\mathrm{max},0.1} = \frac{1}{3} \cdot \sigma_{\mathrm{min},0.1}^2,
\tag{9.13}
$$

$$
\mathcal{J}_{2,\mathrm{m},0.1} = \frac{1}{3} \cdot \sigma_{\mathrm{m},0.1}^2,
\tag{9.14}
$$

where the mean stress $\sigma_{\mathrm{m},0.1}$ is calculated using Equation (9.9). Equation (9.7) can be reorganised in a form

$$
\alpha \cdot \mathcal{J}_{2,\mathrm{m},0.1} = \left(\beta + \frac{A}{N_{\mathrm{f}}^c} \right)^2 - \mathcal{J}_{2,\mathrm{max},0.1}.
\tag{9.15}
$$

All parameters are known on the right side of the Equation (9.15). Its value is calculated for each point in the data set. Then, the value of α is calculated using the least squares method to solve the system of linear equations in the MATLAB software [56]. All material parameters necessary for this criterion are therefore calculated and their values are listed in Tab. 9.4.

Tab. 9.4: Material parameters required for the Berrehili et al. second invariant criterion.

Material parameter	Value	Unit
β	3.87	MPa
A	768.08	MPa
c	0.463	-
α	−1.795	-

To estimate the fatigue lifetime at a critical location, $\mathcal{J}_{2,\mathrm{max}}$ and $\mathcal{J}_{2,\mathrm{m}}$ must be calculated from the results of the numerical simulation according to Equation (9.11).The resulting formula for fatigue lifetime prediction is

$$N_{\mathrm{f}} = \sqrt[c]{\frac{A}{\sqrt{\mathcal{J}_{2,\mathrm{max}} + \alpha \cdot \mathcal{J}_{2,\mathrm{m}}} - \beta}}, \tag{9.16}$$

where A, α, β, and c are taken from table 9.4. $\mathcal{J}_{2,\mathrm{max}}$ is calculated as

$$
\begin{aligned}
\mathcal{J}_{2,\mathrm{max}} = {} & \frac{1}{6} \cdot [(\sigma_{11,\mathrm{min}} - \sigma_{22,\mathrm{min}})^2 + (\sigma_{22,\mathrm{min}} - \sigma_{33,\mathrm{min}})^2 + (\sigma_{33,\mathrm{min}} - \sigma_{11,\mathrm{min}})^2] \\
& + \sigma_{12,\mathrm{min}}^2 + \sigma_{23,\mathrm{min}}^2 + \sigma_{31,\mathrm{min}}^2,
\end{aligned}
\tag{9.17}
$$

and $\mathcal{J}_{2,\mathrm{m}}$ is calculated as

$$
\begin{aligned}
\mathcal{J}_{2,\mathrm{m}} = {} & \frac{1}{6} \cdot [(\sigma_{11,\mathrm{m}} - \sigma_{22,\mathrm{m}})^2 + (\sigma_{22,\mathrm{m}} - \sigma_{33,\mathrm{m}})^2 + (\sigma_{33,\mathrm{m}} - \sigma_{11,\mathrm{m}})^2] \\
& + \sigma_{12,\mathrm{m}}^2 + \sigma_{23,\mathrm{m}}^2 + \sigma_{31,\mathrm{m}}^2,
\end{aligned}
\tag{9.18}
$$

where individual stress values are taken from the stress tensor in the global coordinate system for minimum force $\boldsymbol{T}_{\sigma,\mathrm{global},F_{\mathrm{min}}}$ and the stress tensor in the global coordinate system for mean force $\boldsymbol{T}_{\sigma,\mathrm{global},F_{\mathrm{m}}}$, respectively. The resulting lifetime predictions for both critical locations and load cases are listed in Tab. 9.5.

Tab. 9.5: Estimated numbers of cycles to failure at investigated locations for pressure magnitude $|\sigma_{\mathrm{c}}| = 4$ and 3 MPa according to Berrehili et al. second invariant criterion.

Pressure magnitude $|\sigma_{\mathrm{c}}|$ [MPa]	Estimated lifetime N_{f} [-]	
	Location 1	Location 2
4	5 570	86 905
3	12 743	378 134

9.4 Nitta et al. strain energy density criterion

The criterion proposed by Nitta et al. was discussed in Section 5.3.4. The previously presented criterion formula is

$$\Delta W_1 = \frac{\Delta\sigma_1}{2}\Delta\varepsilon_1 = A_1 \cdot N_{\mathrm{f}}^{-\beta_1}, \tag{9.19}$$

where A_1 and β_1 are material parameters, which can be derived from the Wöhler curve of the material. Again, the Wöhler curve of flat 0°/0° printed specimens was used. The strain range in the elastic region is defined as

$$\Delta\varepsilon = \frac{\Delta\sigma}{E}, \tag{9.20}$$

where E is the elastic modulus of the material. Substituting the strain range in the criterion Equation (9.19) by the term in Equation (9.20), the formula results in

$$
\begin{aligned}
\Delta W_I &= \frac{\Delta\sigma_1}{2} \cdot \Delta\varepsilon_1 = A_1 \cdot N_{\mathrm{f}}^{-\beta_1} \\
&= \frac{\Delta\sigma_1}{2} \cdot \frac{\Delta\sigma_1}{E} = A_1 \cdot N_{\mathrm{f}}^{-\beta_1} \\
&= \frac{\Delta\sigma_1^2}{2 \cdot E} = A_1 \cdot N_{\mathrm{f}}^{-\beta_1}.
\end{aligned}
\tag{9.21}
$$

The Wöhler curve was measured under uniaxial tension, therefore the load nature corresponds with the proposed criterion. The tensile elastic modulus of the material is used. Using the experimentally measured data, the left term in Equation (9.21) can be calculated and the material parameters A_1 and β_1 can be derived using a power fit of the data points. The resulting parameters are listed in Tab. 9.6.

Tab. 9.6: Material parameters required for the Nitta et al. strain energy density criterion.

Material parameter	Value	Unit
A_1	10.05	MPa
β_1	0.368	-

To estimate the lifetime at the investigated locations, the first principal stress and strain ranges must be calculated. The first principal stress range is calculated as

$$\Delta\sigma_1 = 2 \cdot (\sigma_{1,F_{\min}} - \sigma_{1,F_{\mathrm{m}}}), \tag{9.22}$$

the first principal strain is calculated analogously as

$$\Delta\varepsilon_1 = 2 \cdot (\varepsilon_{1,F_{\min}} - \varepsilon_{1,F_{\mathrm{m}}}), \tag{9.23}$$

where the stress and strain values for the minimum and mean force are taken from the stress and strain tensors in the principal coordinate system.

The formula for estimating the lifetime at the investigated locations is presented in Equation (9.24). The predicted cycles to failure for each of these locations corresponding to a given pressure magnitude are listed in Tab. 9.7.

$$N_{\mathrm{f}} = \sqrt[-\beta]{\frac{\Delta\sigma_1 \cdot \Delta\varepsilon_1}{2 \cdot A_1}} \tag{9.24}$$

Tab. 9.7: Estimated numbers of cycles to failure at investigated locations for pressure magnitude $|\sigma_c| = 4$ and 3 MPa according to Nitta et al. strain energy density criterion.

Pressure magnitude $|\sigma_c|$ [MPa]	Estimated lifetime N_f [-]	
	Location 1	Location 2
4	7 650	110 446
3	36 562	526 028

9.5 Validation of the lifetime prediction criteria

Compressive fatigue testing of the 3D printed metamaterial structure was performed to validate the lifetimes predicted by the individual criteria. The test frequency was the same as for the dogbone specimens $f = 10$ Hz. The stress assymetry ratio $R = 10$, as the loading is compressive. This matter was previously discussed in Section 8.7. An infinite fatigue life of the tested structure was assumed after $N_{limit} = 5 \cdot 10^6$ cycles without visible damage to the struts. The measured Wöhler curve of the structure is shown in Fig. 9.2. The number of cycles to failure is presented in relation to the amplitude of pressure applied on the top face $\sigma_{c,a}$. The failure in all structures was caused by cracks propagating from the second critical location (sloped strut face).
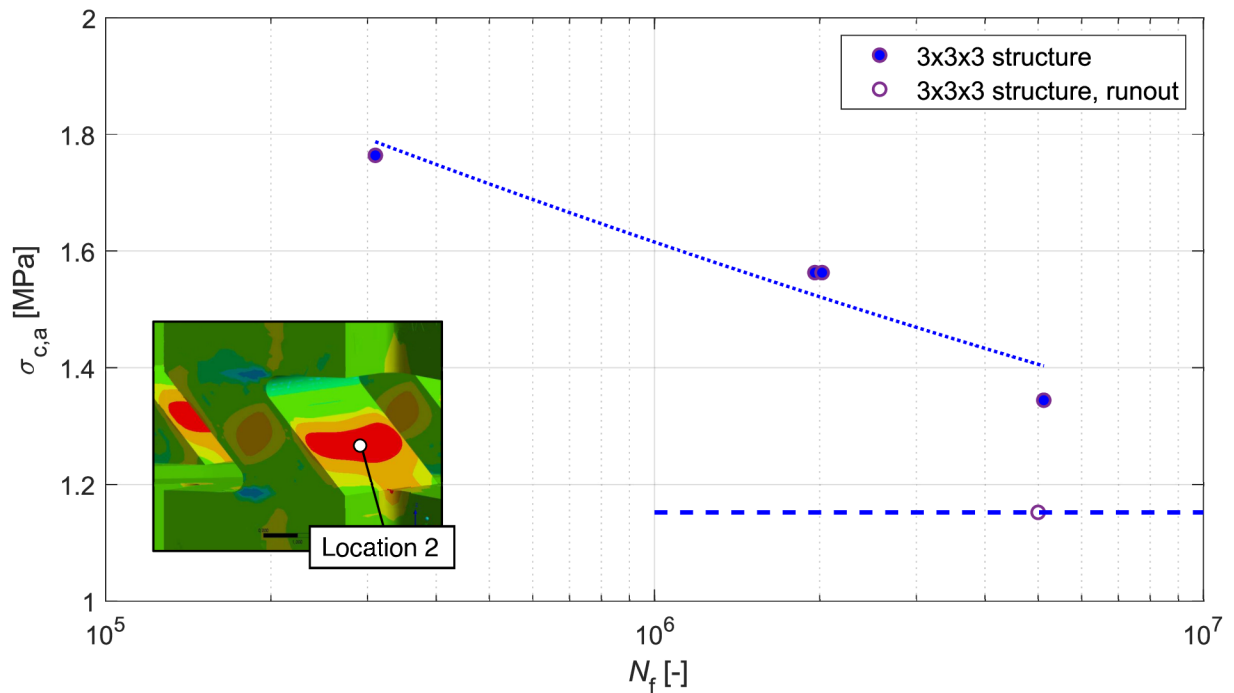
Fig. 9.2: Wöhler curve of the 3D printed metamaterial structure of 3x3x3 cubes.

9.6 Results of the lifetime predictions

The linear dependence of the stress and strain response of the numerical model can be expressed from the realised pair of load cases (maximum pressure magnitude $|\sigma_c|$ of 4 and 3 MPa). The values were interpolated to obtain the model response at a maximum pressure magnitude of 3.25, 3.5, and 3.75 MPa. For all of these loading levels, the fatigue lifetime was predicted to plot the respective dependencies. The resulting fatigue lifetime

predictions for all criteria at critical locations 1 and 2 are shown in Fig. 9.3 and Fig. 9.4, respectively. The lifetime of the printed structure was plotted in the same graph to allow the possibility of comparison of the criteria and the assertion of their suitability. The fatigue lifetime is plotted as a function of the amplitude of pressure $\sigma_{c,a}$.
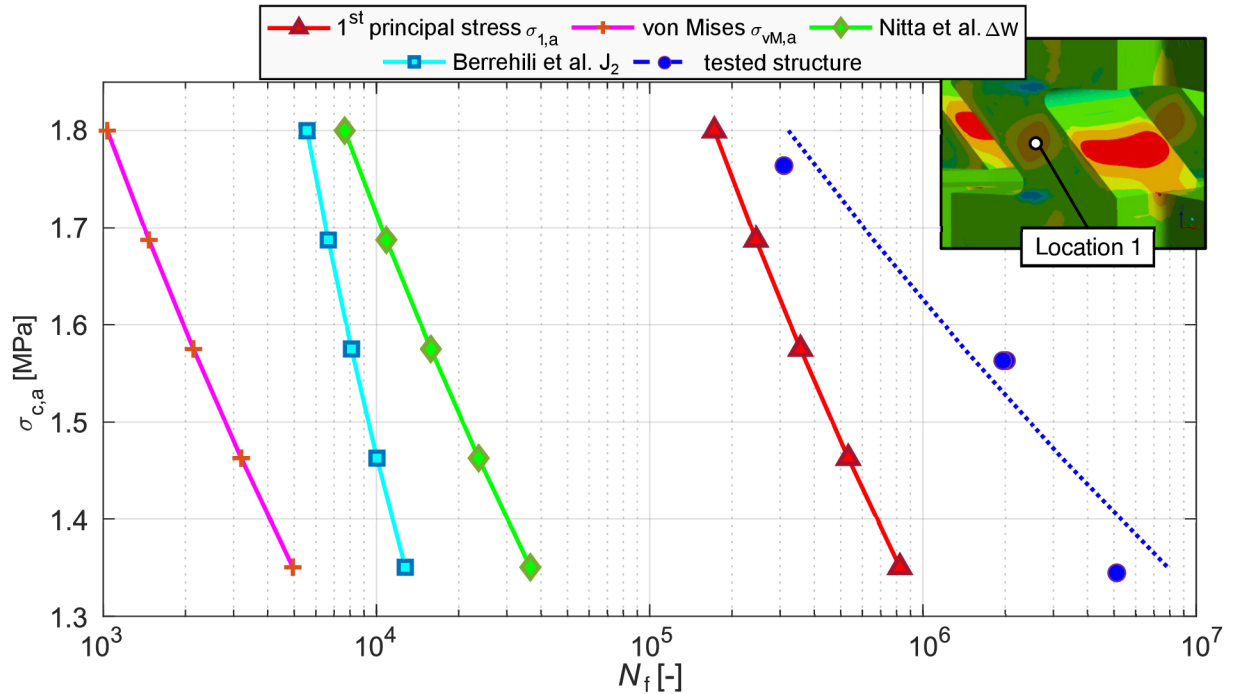
Fig. 9.3: Predicted fatigue lifetimes at the first critical location (vertical strut face) according to each criterion and the observed fatigue lifetimes of the real printed structure.
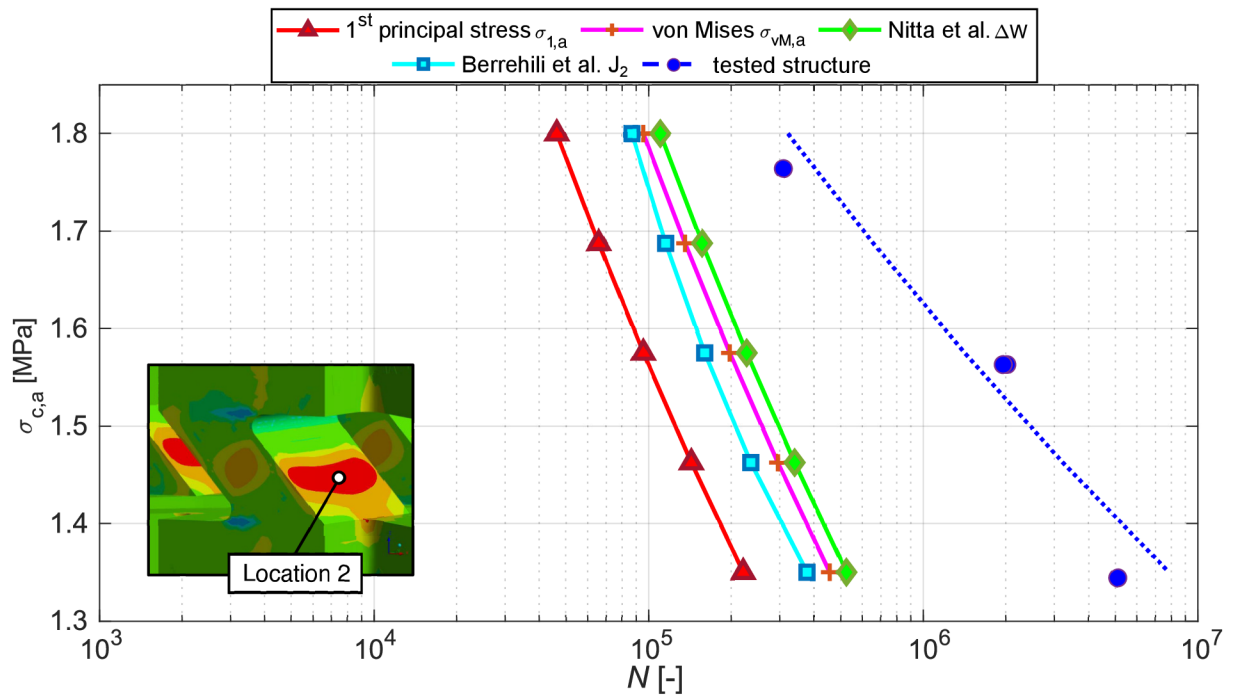
Fig. 9.4: Predicted fatigue lifetimes at the second critical location (sloped strut face) according to each criterion and the observed fatigue lifetimes of the real printed structure.

10   Analysis of the results and discussion

The results of the lifetime predictions according to each criterion can be analysed and their appropriateness discussed thanks to the experimentally measured Wöhler curve of the printed structure.

10.1   Compatibility of the criteria

First, the results for the second critical location are discussed. The lifetime estimations obtained using all criteria are comparable, showing that they are suitable for the stress state present at this location. Furthermore, the results are conservative, meaning that the lifetime predictions are on the safe side and that the real structure will not fail sooner than predicted. The stress state at this location can be considered biaxial, given the low magnitude of the third principal stress. The dominant stresses are the first and second principal stresses. For illustration purposes, the stress and strain tensors in the principal coordinate system at the second critical location for the loading case of the minimum force corresponding to a pressure magnitude of 4 MPa is shown below.

$$\boldsymbol{T}_\sigma = \begin{bmatrix} 22.95 & 0 & 0 \\ 0 & 14.52 & 0 \\ 0 & 0 & 0.025 \end{bmatrix} \text{MPa}$$

$$\boldsymbol{T}_\varepsilon = \begin{bmatrix} 0.0151 & 0 & 0 \\ 0 & 0.0042 & 0 \\ 0 & 0 & -0.0145 \end{bmatrix}$$

The criteria considering more aspects predicted the fatigue lifetime better than the first principal stress criterion, which is built on only one parameter. However, even this simple criterion predicted the fatigue lifetime comparably with the other criteria. Both Berrehili et al. and von Mises criteria work with all components of the stress tensor and describe the present stress state better. Nitta et al. predicted the fatigue lifetime the best at the second critical location.

A higher discrepancy is observed in the fatigue lifetime predictions at the first critical location. Upon inspection, the stress state at this location is also biaxial. However, as opposed to the second critical location, the dominant principal stresses are the first and third one. Furthermore, the third principal stress has a very high negative value. The stress and strain tensors in the principal coordinate system at the first location for the loading case of the minimum force corresponding to a pressure magnitude of 4 MPa is shown below.

$$\boldsymbol{T}_\sigma = \begin{bmatrix} 18.02 & 0 & 0 \\ 0 & 0.005 & 0 \\ 0 & 0 & -34.47 \end{bmatrix} \text{MPa}$$

$$\boldsymbol{T}_{\varepsilon} = \begin{bmatrix} 0.0512 & 0 & 0 \\ 0 & 0.0110 & 0 \\ 0 & 0 & -0.0659 \end{bmatrix}$$

For this location, the criteria using more parameters were not useful. Both the von Mises and Berrehili et al. criteria failed to predict the increased lifetime at the first critical location. The opposite occurred, as these criteria predicted a much shorter fatigue lifetime at this location. Different hypothetical stress states were assumed, and their lifetime was predicted to describe the behaviour of the criteria. The difference between the two dominant principal stresses is the governing parameter in these criteria, where a higher difference decreases the ability of the criteria to correctly predict the lifetime. Furthermore, both of these criteria simplify to the first principal stress criterion for uniaxial and equibiaxial stress states. The hypothetical stress states and their predicted lifetimes are listed in Appendix B. Nitta et al. criterion, which is based on the strain energy density, also failed to better predict the fatigue lifetime. Upon inspection of the principal stress and strain tensors, it can be stated that although the first principal stress is lower at this location, the first principal strain is much higher than at the previous location. However, the precise reason for the criterion inacurracy at this location is unclear. A possible explanation might be related to the first principal stress and strain ratio at the given location. However, the first principal stress criterion produces estimates sufficient for a high-cycle fatigue regime. This criterion is also the only one that correctly predicted the increase in fatigue lifetime at the first critical location.

10.2 Experimental measurement observations

As noted previously, the failure of the printed structures was due to cracks originating at the second critical location. Consequently, it is understood that the fatigue lifetime at the first critical location would likely be longer than observed. However, the fatigue lifetime predictions obtained for both critical locations were compared with a single measured curve from an experiment in which failures occurred only at the second location. This should be taken into account when analysing the results at the first critical location.

Additionaly, some comments can be drawn from the validation experimental measurement. First, the precision of placement of the critical locations that were selected in Section 8.6. Photos of the tested structures were taken at times during and after the experiments. All tested structures had initiated cracks mainly at the second critical location, from where they grew inward and caused the strut failure (Fig. 10.1). This observation aligns with the distribution of the first principal stress along the strut, which is higher at the second critical location, and the crack begins to initiate earlier.

Furthermore, some more remarks should be made considering the measured and predicted Wöhler curves. The lifetime predictions were made using the stress and strain values of one strut before cracks began to initiate. Thus, the predicted lifetimes only account for one strut, not taking into account the effect of the whole structure. In contrast to this, the behaviour of the printed structure is highly affected by this. Once a crack initiates
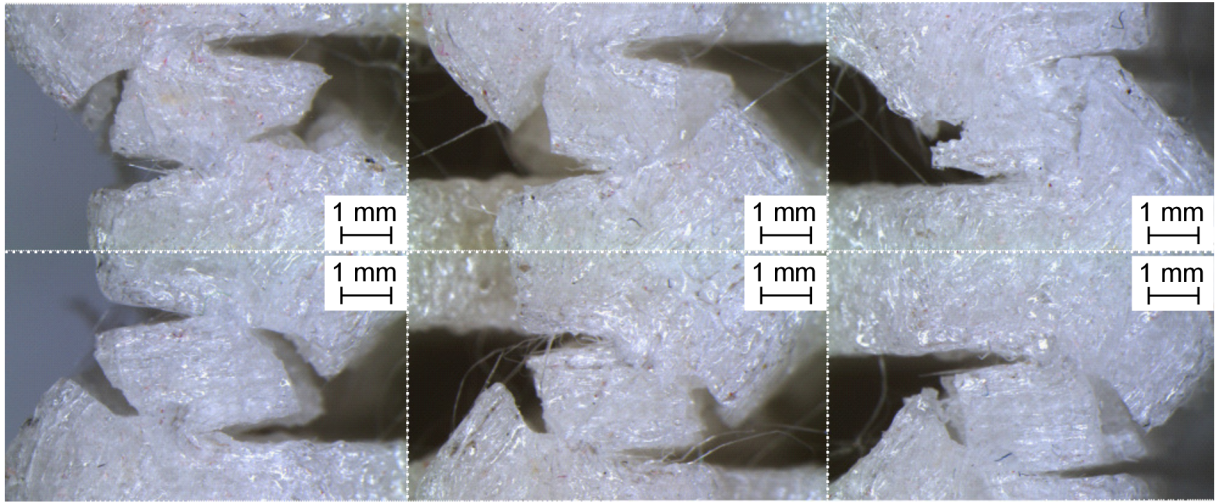
Fig. 10.1: Failed layers of struts due to cracks initiated at the second critical location and growing through the strut.

on one strut and the strut loses some of its bearing capacity, the load is redistributed among the other ones. The crack growth is thus somewhat even along all struts, and the structure failure is noted as a failure of the whole layer of struts. This can be observed in the development of the minimum displacement of the machine piston in each cycle during the experiment, which is plotted in Fig. 10.2. The displacement decreases slowly until the entire strut layer fails. At that point, the displacement decreases dramatically as the failed struts are compressed. This number of cycles is recorded as the number of cycles to failure N_f.
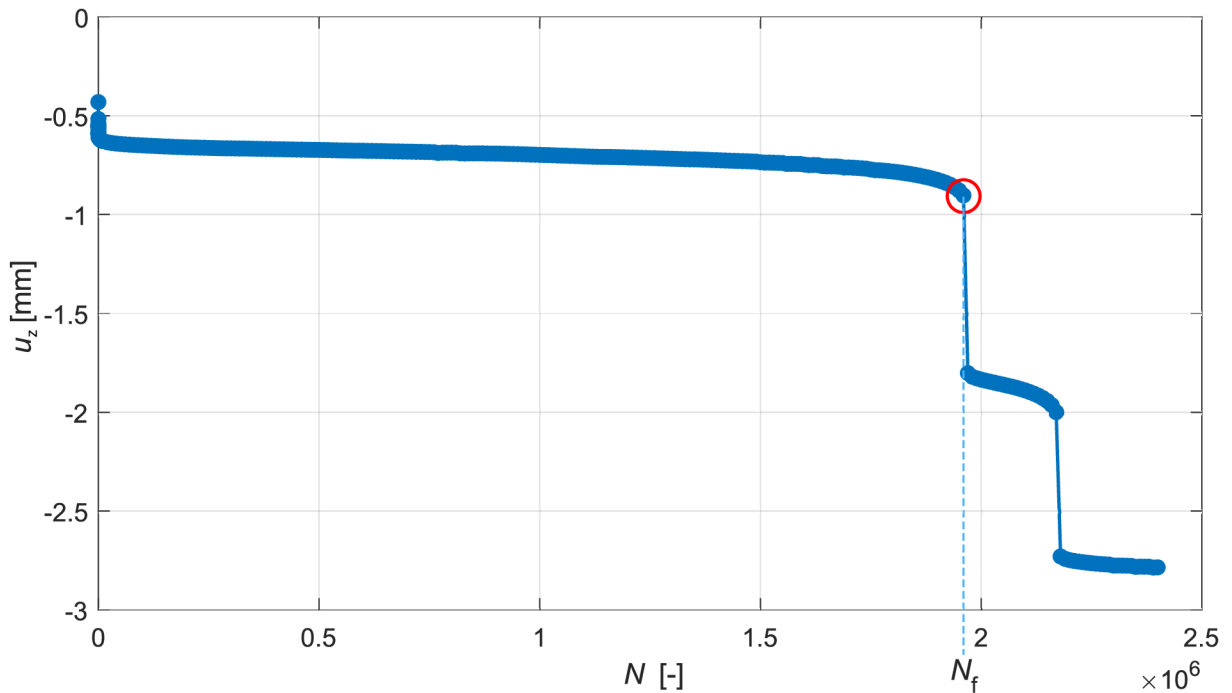
Fig. 10.2: Displacement measured during a fatigue test of a printed metamaterial structure. The point in red circle is considered as the number of cycles to failure N_f, as it marks the failure of a full layer of struts of the structure.

10.3 Printing repeatability

All specimens and structures investigated in this thesis were printed using a Qidi Tech X-Max FDM printer. More structures were printed using a printer of the same brand but with a different model, the Qidi Tech X-Plus, to test the repeatability of the printing. All printing parameters were set identically, only the printer model and its location changed. One printed structure from each printer was scanned using an X-Ray scanner Tescan UniTOM XL at Technical University Graz. This provided layer-by-layer imaging of the structures, which could be reconstructed into 3D models of the printed structures, as shown in Fig. 10.3

(a)   (b)
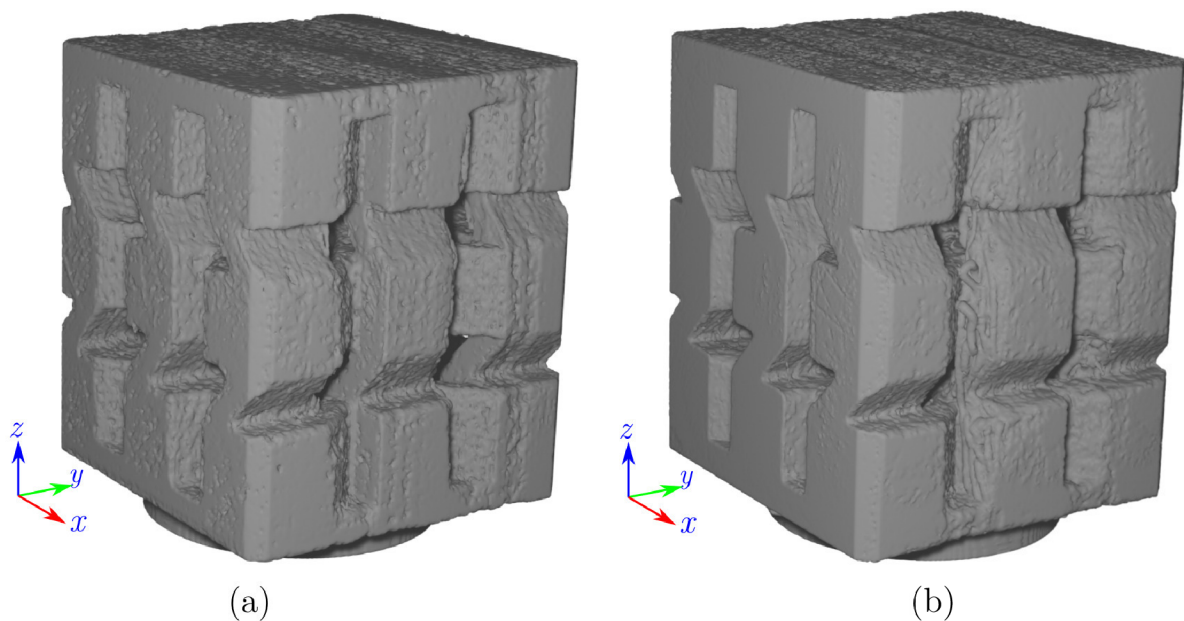
Fig. 10.3: 3D models of the scanned printed metamaterial structures printed with (a) Qidi Tech X-Max, (b) Qidi Tech X-Plus.

The differences in structures were investigated. Special attention was paid to the struts, as these are the main areas of interest. The structures printed with Qidi Tech X-Plus have on average 15.6% thicker struts than the original structures printed with Qidi Tech X-Max. This can dramatically change the behaviour of the structure. Furthermore, the structures printed with Qidi Tech X-Plus are on average 7.8 % heavier, 1.3 % thicker, 0.4 % wider and 0.7 % higher. All of these contribute to an increase in stiffness by 38 %.

Fatigue tests were performed on the second set of structures under identical testing conditions. The cracks initiated at both locations with prominent damage at the first critical location (Fig. 10.4). The cause of this difference in behaviour can be linked to the increased structure stiffness and the thickness of the struts. Greater thickness makes the struts less prone to bending and the first critical location (vertical strut face) more pronounced. The Wöhler curves of both structures are plotted in Fig. 10.5. The Wöhler curves show the significant increase in fatigue lifetime for structures printed with Qidi Tech X-Plus. The change in thickness thus causes not only a change in the dominant
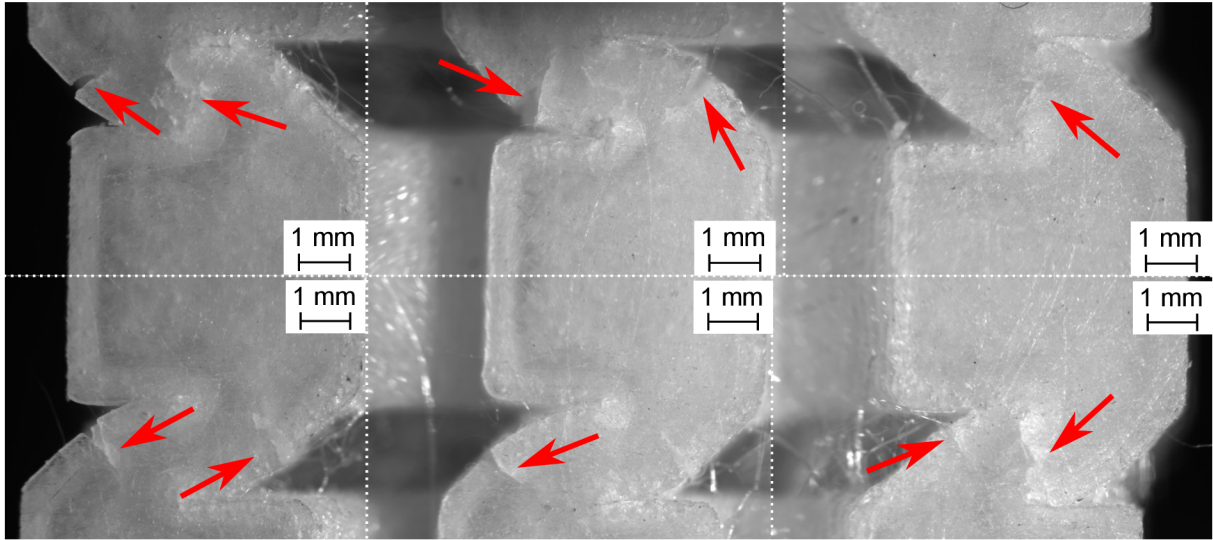
Fig. 10.4: Front view of the structure's failed struts with cracks initiating at both the first and second critical locations. Printer used: Qidi Tech X-Plus.

critical location but also a significant increase in the lifetime. However, it also shows the main disadvantage of FDM, which is the low resolution and dimensional inaccuracy. Individual machines might produce different dimensions of a printed part while using the same source geometry. The method can also be sensitive to environmental conditions, depending on the source material used.
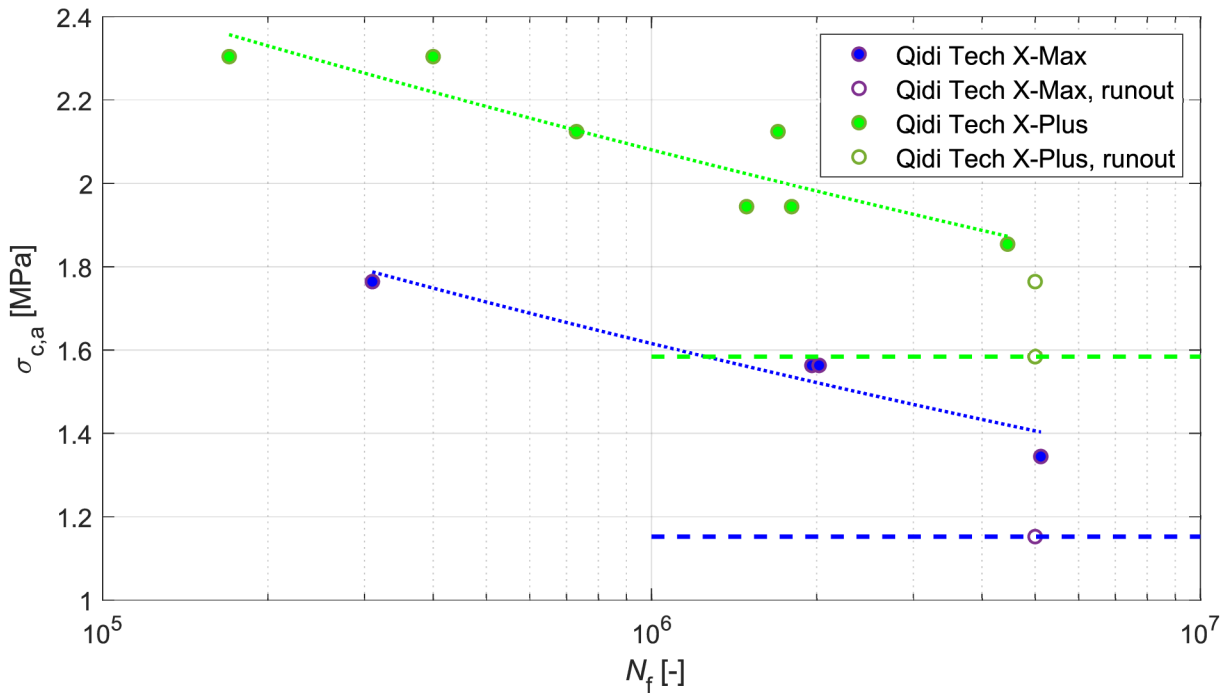
Fig. 10.5: Measured Wöhler curves of 3x3x3 structures printed with Qidi Tech X-Max and Qidi Tech X-Plus with identical printing setting.

Conclusion

This thesis focuses on the topic of fatigue behaviour of an additively manufactured meta-material structure. The main objective of the thesis was to predict the fatigue lifetime of a 3D printed metamaterial structure with tunable stiffness.

The topic of metamaterials was introduced in the theoretical part of the thesis. Additionaly, the AM methods of polymer materials were described and their advantages for metamaterial production were highlighted. The mechanical behaviour of polymers was discussed to lay the basis for the practical part of the thesis. Four criteria were presented for fatigue lifetime prediction: the first principal stress criterion, von Mises criterion, Berrehili et al. second invariant criterion and Nitta et al. strain energy density criterion.

The practical part of the thesis includes steps that lead to a fatigue lifetime prediction of the proposed metamaterial structure. First, the material parameters necessary for the material model were obtained experimentally. Standardised 3D printed specimens including dogbone, cube, and rectangular specimens were manufactured in six different printing orientations to quantify the directional effect of the printing.

Then, based on the experimentally obtained data, the numerical model was created. The full-size model was reduced to minimise the amount of material consumed. Mesh sensitivity analysis was performed to ensure the validity of numerically calculated results. The boundary conditions were applied, and the tensile/compressive model of material was applied to individual elements according to each element's response to load. The numerical model was verified using an experimentally measured response to compressive loading, which aligned with the response obtained from the model. Two critical locations were assessed based on the value of the first principal stress, which is the crack-opening stress. The structure loading scheme to simulate cyclic loading was presented.

The stress and strain values obtained from the numerical simulation were applied to the lifetime prediction criteria presented. The results were plotted against a measured Wöhler curve of the structure for validation purposes. The more complicated criteria proved useful at the critical location with a compact Mohr's circle, indicating a more uniform stress state. Here they predicted the lifetime with more accuracy than the first principal stress criterion. In contrast, the other critical location exhibits a much larger difference between the two principal stresses, resulting in an elevated stress state, which neither of the complex criteria could capture. The large principal stress range proved to be the main obstacle to a correct prediction of the lifetime. However, the first principal stress criterion predicted the fatigue lifetime sufficiently well in both locations, while being very straightforward and not requiring many input parameters.

This thesis can also serve as a good base for further research, where geometrical imperfections or crack growth can be included in the numerical model. The environmental influence could also be investigated and a new criterion could be proposed with experiments required to describe the stress state correctly in both critical locations.

Bibliography

[1] KSHETRIMAYUM, R.S. A brief intro to metamaterials. Online. *IEEE Potentials*. 2005, vol. 23, iss. 5, p. 44-46. ISSN 0278-6648. Available at: `https://doi.org/10.1109/MP.2005.1368916`. [cit. 2023-10-20].

[2] SURJADI, James Utama; GAO, Libo; DU, Huifeng; LI, Xiang; XIONG, Xiang et. al. Mechanical Metamaterials and Their Engineering Applications. Online. *Advanced Engineering Materials* . 2019, vol. 21. Available at: `https://doi.org/10.1002/adem.201800864`. [cit. 2023-11-02].

[3] KUMAR, R.; KUMAR, M.; CHOHAN, J.S. and KUMAR, S. Overview on metamaterial: History, types and applications. Online. *Materials Today: Proceedings* . 2022, vol. 56, part 5, p. 3016-3024. ISSN 2214-7853. Available at: `https://doi.org/10.1016/j.matpr.2021.11.423`. [cit. 2023-10-26].

[4] ENGHETA, N and ZIOLKOWSKI, Richard .W. *Overview on metamaterial: History, types and applications* PDF. Online. Hoboken: Wiley-Interscience, c2006. ISBN 978-0-471-76102-0. [cit. 2023-10-24].

[5] CUMMER, Steven A.; CHRISTENSEN, Johan and ALÙ, Andrea. Controlling sound with acoustic metamaterials. Online. *Nature Reviews Materials* . 2016, vol. 1, iss. 3. ISSN 2058-8437. Available at: `https://doi.org/10.1038/natrevmats.2016.1`. [cit. 2023-10-26].

[6] MA, Guancong and SHENG, Ping. Acoustic metamaterials: From local resonances to broad horizons. Online. *Science Advances* . 2016, vol. 2, iss. 2. ISSN 2375-2548. Available at: `https://doi.org/10.1126/sciadv.1501595`. [cit. 2023-10-26].

[7] SKLAN, Sophia R and LI, Baowen. Thermal metamaterials: functions and prospects. Online. *National Science Review* . 2018, vol. 5, iss. 2. p. 138-141. ISSN 2095-5138. Available at: `https://doi.org/10.1093/nsr/nwy005`. [cit. 2024-02-25].

[8] WANG, Lei; SHI, Shouwen; FU, Sichao; CHEN, Gang and CHEN, Xu. Evaluation of multiaxial fatigue life prediction criteria for PEEK. Online. *Theoretical and Applied Fracture Mechanics* . 2014, vol. 73, p. 128-135. ISSN 01678442. Available at: `https://doi.org/10.1016/j.tafmec.2014.07.012`. [cit. 2024-01-24].

[9] LI, Ying; LI, Wei; HAN, Tiancheng; ZHENG, Xu; LI, Jiaxin et al. Transforming heat transfer with thermal metamaterials and devices. Online. *Nature Reviews Materials* . 2021, vol. 6, iss. 6, p. 488-507. ISSN 2058-8437. Available at: `https://doi.org/10.1038/s41578-021-00283-2`. [cit.2023-10-26].

[10] CARDOSO, Joao O.; BORGES Joao Paulo and VELHINHO, Alexandre. Structural metamaterials with negative mechanical/thermomechanical indices: A review. Online. *Progress in Natural Science: Materials International* . 2021, vol. 31, iss. 6, p. 801-808. ISSN 1002-0071. Available at: `https://doi.org/10.1016/j.pnsc.2021.10.015`. [cit. 2023-10-27].

[11] YU, Xianglong; ZHOU, Ji; LIANG, Haiyi; JIANG, Zhengyi and WU, Lingling. Mechanical metamaterials associated with stiffness, rigidity and compressibility: A brief review. Online. *Progress in Materials Science* . 2018, vol. 94, p. 114-173. ISSN 0079-6425. Available at: https://doi.org/10.1016/j.pmatsci.2017.12.003. [cit. 2023-10-27].

[12] RAMINHOS, J S; BORGES, J P and VELHINHO, A. Development of polymeric anepectic meshes: auxetic metamaterials with negative thermal expansion. Online. *Smart Materials and Structures* . 2019, vol. 28., iss. 4. ISSN 0964-1726. Available at: https://doi.org/10.1088/1361-665X/ab034b. [cit. 2023-11-16].

[13] FLEISCH, M; THALHAMER, A.; MEIER, G; RAGUŽ, I; FUCHS, P.F. et. al. Functional mechanical metamaterial with independently tunable stiffness in the three spatial directions. Online. *Materials Today Advances* . 2021, vol. 11., iss. 4, p. 100155. ISSN 2590-0498. Available at: https://doi.org/10.1016/j.mtadv.2021.100155. [cit. 2023-11-16].

[14] *History and Future of Plastics* . Online. Sciencehistory.org. 2023. Available at: https://www.sciencehistory.org/education/classroom-activities/role-playing-games/case-of-plastics/history-and-future-of-plastics/. [cit.2023-11-28].

[15] OSSWALD, Tim A. and MENGES, Georg. *Materials science of polymers for engineers* . 3rd ed. Cincinnati: Hanser Publishers, 2012. ISBN 9781569905142.

[16] MCKEEN, Laurence W.*Fatigue and Tribological Properties of Plastics and Elastomers* . 3rd ed. William Andrew, 2016. ISBN 978-0-323-44201-5.

[17] SMITH, Raymond L.; TAKKELLAPATI, Sudhakar and RIEGERIX, Rachelle C. Recycling of Plastics in the United States: Plastic Material Flows and Polyethylene Terephthalate (PET) Recycling Processes. Online. *ACS Sustainable Chemistry & Engineering* . 2022, vol. 10., iss. 6, p. 2084-2096. ISSN 2168-0485. Available at: https://doi.org/10.1021/acssuschemeng.1c06845. [cit. 2023-12-07].

[18] IZDEBSKA-PODSIADŁY, Joanna.*Polymers for 3D Printing* . 1st ed. William Andrew, 2022. ISBN 978-0-12-818311-3.

[19] *Ullmann's Encyclopedia of Industrial Chemistry* . Online. Wiley, 2003. ISBN 9783527303854. Available at: https://doi.org/10.1002/14356007. [cit. 2024-02-25].

[20] *Nylons Polyamide* . Online. bpf.co.uk. 2008. Available at: https://www.bpf.co.uk/plastipedia/polymers/Polyamides.aspx. [cit.2023-12-15].

[21] INTERNATIONAL ORGANIZATION FOR STANDARDIZATION [ISO]. ISO/ASTM 52900:2021, *Additive manufacturing – General principles – Fundamentals and vocabulary*. Geneva: ISO, 2021.

[22] LIGON, Samuel Clark; LISKA, Robert; STAMPFL, Jürgen; GURR, Matthias and MÜLHAUPT, Rolf. Polymers for 3D Printing and Customized Additive Manufac-

turing. Online. *Chemical Reviews*. 2017, vol. 117, iss. 15, p. 10212-10290. ISSN 0009-2665. Available at: `https://doi.org/10.1021/acs.chemrev.7b00074`. [cit. 2024-01-29].

[23] ZIAEE, Mohsen and CRANE, Nathan B. Binder jetting: A review of process, materials, and methods. Online. *Additive Manufacturing*. 2019, vol. 28, p. 781-801. ISSN 22148604. Available at: `https://doi.org/10.1016/j.addma.2019.05.031`. [cit. 2024-01-29].

[24] SUWANPRATEEB, Jintamai; KERDSOOK, Somrudee; BOONSIRI, Tanyarat and PRATUMPONG, Patcharee. Evaluation of heat treatment regimes and their influences on the properties of powder-printed high-density polyethylene bone implant. Online. *Polymer International*. 2011, vol. 60, iss. 5, p. 758-764. ISSN 0959-8103. Available at: `https://doi.org/10.1002/pi.3006`. [cit. 2024-01-29].

[25] TAN, Lisa Jiaying; ZHU, Wei and ZHOU, Kun. Recent Progress on Polymer Materials for Additive Manufacturing. Online. *Advanced Functional Materials*. 2020, vol. 30, iss. 30. ISSN 1616-301X. Available at: `https://doi.org/10.1002/adfm.202003062`. [cit. 2024-01-25].

[26] ASKARI, Meisam; HUTCHINS, David A.; THOMAS, Peter J.; ASTOLFI, Lorenzo; WATSON, Richard L. et al. Additive manufacturing of metamaterials: A review. Online. *Additive Manufacturing*. 2020, vol. 36. ISSN 22148604. Available at: `https://doi.org/10.1016/j.addma.2020.101562`. [cit. 2024-01-25].

[27] MONTGOMERY, S. Macrae; KUANG, Xiao; ARMSTRONG, Connor D. and QI, H. Jerry. Recent advances in additive manufacturing of active mechanical metamaterials. Online. *Current Opinion in Solid State and Materials Science*. 2020, vol. 24, iss. 5. ISSN 13590286. Available at: `https://doi.org/10.1016/j.cossms.2020.100869`. [cit. 2024-01-25].

[28] SAADI, M. A. S. R.; MAGUIRE, Alianna; POTTACKAL, Neethu T.; THAKUR, Md Shajedul Hoque; IKRAM, Maruf Md. et al. Direct Ink Writing: A 3D Printing Technology for Diverse Materials. Online. *Advanced Materials*. 2022, vol. 34, iss. 28. ISSN 0935-9648. Available at: `https://doi.org/10.1002/adma.202108855`. [cit. 2024-02-25].

[29] MELCHELS, Ferry P.W.; FEIJEN, Jan and GRIJPMA, Dirk W. A review on stereolithography and its applications in biomedical engineering. Online. *Biomaterials*. 2010, vol. 31, iss. 24, p. 6121-6130. ISSN 01429612. Available at: `https://doi.org/10.1016/j.biomaterials.2010.04.050`. [cit. 2024-02-25].

[30] YAO, Hongyi; WANG, Jieqiong and MI, Shengli. Photo Processing for Biomedical Hydrogels Design and Functionality: A Review. Online. *Polymers*. 2018, vol. 10, iss. 1, p. 6121-6130. ISSN 2073-4360. Available at: `https://doi.org/10.3390/polym10010011`. [cit. 2024-02-25].

[31] KHADILKAR, Aditya; WANG, Jun and RAI, Rahul. Deep learning–based stress prediction for bottom-up SLA 3D printing process. Online. *The International Jour-*

nal of Advanced Manufacturing Technology. 2019, vol. 102 iss. 5-8, p. 2555-2569. ISSN 0268-3768. Available at: `https://doi.org/10.1007/s00170-019-03363-4`. [cit. 2024-02-25].

[32] WU, Xin; SU, Yutai a SHI, Jing. Perspective of additive manufacturing for metamaterials development. Online. *Smart Materials and Structures*. 2019, vol. 208 iss. 9. ISSN 0964-1726. Available at: `https://doi.org/10.1088/1361-665X/ab2eb6`. [cit. 2024-03-20].

[33] RÖESLER, Joachim; BÄKER, Martin and HARDERS, Harald.*Mechanical Behaviour of Engineering Materials*. 1st ed. Springer Berlin, Heidelberg, 2007. ISBN 978-3-540-73446-8.

[34] GALESKI, Andrzej. Strength and toughness of crystalline polymer systems. Online. *Progress in Polymer Science*. 2003, vol. 28, iss. 12, p. 1643-1699. ISSN 00796700. Available at: `https://doi.org/10.1016/j.progpolymsci.2003.09.003`. [cit. 2024-03-20].

[35] *Handbook of polyethylene pipe* . Online. Plastic Pipe Institute, 2012. [cit. 2024-03-20].

[36] SCHÜTZ, Walter. A history of fatigue. Online. *Engineering Fracture Mechanics*. 1996, vol. 54, iss. 2, p. 263-300. ISSN 00137944. Available at: `https://doi.org/10.1016/0013-7944(95)00178-6`. [cit. 2024-03-20].

[37] *Characterization and failure analysis of plastics*. Editor Steve LAMPMAN. Materials Park, OH: ASM International, 2003. ISBN 978-0-87170-789-5.

[38] CRAWFORD, R.J. and BENHAM, P.P. Some fatigue characteristics of thermoplastics. Online. *Polymer*. 1975, vol. 16, iss. 12, p. 908-914. ISSN 00323861. Available at: `https://doi.org/10.1016/0032-3861(75)90212-8`. [cit. 2024-01-23].

[39] DAO, K. C. Fatigue failure mechanisms in polymer composites. Online. *Polymer Composites*. 1982, vol. 3, iss. 1, p. 12-17. ISSN 0272-8397. Available at: `https://doi.org/10.1002/pc.750030104`. [cit. 2024-01-23].

[40] RIDDELL, M. N.; KOO, G. P. and O'TOOLE, J. L. Fatigue mechanisms of thermoplastics. Online. *Polymer Engineering & Science*. 1966, vol. 6, iss. 4, p. 363-368. ISSN 0032-3888. Available at: `https://doi.org/10.1002/pen.760060414`. [cit. 2024-01-23].

[41] SAUER, J.A. and RICHARDSON, G.C. Fatigue of polymers. Online. *Int J Fract*. 1980, vol. 16, p. 499–532. Available at: `https://doi.org/10.1007/BF02265215`. [cit. 2024-01-23].

[42] DEBLIECK, Rudy A.C.; VAN BEEK, D.J.M.; REMERIE, Klaas and WARD, Ian M. Failure mechanisms in polyolefines: The role of crazing, shear yielding and the entanglement network. Online. *Polymer*. 2011, vol. 52, iss. 14, p. 2979-2990. ISSN 00323861. Available at: `https://doi.org/10.1016/j.polymer.2011.03.055`. [2024-03-13].

[43] BRETZ, P.E.; HERTZBERG, R.W. and MANSON, J.A. Mechanisms of fatigue damage and fracture in semi-crystalline polymers. Online. *Polymer*. 1981, vol. 22, iss. 9, p. 1272-1278. ISSN 00323861. Available at: `https://doi.org/10.1016/0032-3861(81)90145-2`. [cit. 2024-03-13].

[44] HERTZBERG, Richard W.; VINCI, Richard P. and HERTZBERG, Jason L.*Deformation and fracture mechanics of engineering materials*. 6th ed. Wiley, 2021. ISBN 978-1-119-67049-0.

[45] KINLOCH, A. J. and YOUNG, R. J.*Fracture Behaviour of Polymers*. Online. Dordrecht: Springer Netherlands, 1995. ISBN 978-94-017-1596-6. Available at: `https://doi.org/10.1007/978-94-017-1594-2`. [cit. 2024-03-13].

[46] ZIRAK, Nader and TCHARKHTCHI, Abbas. Fatigue life prediction for amorphous glassy polymers based on cumulative evolution of micro-defects. Online. *International Journal of Fatigue*. 2023, vol. 167, ISSN 01421123. Available at: `https://doi.org/10.1016/j.ijfatigue.2022.107360`. [cit. 2024-03-13].

[47] WÖHLER, August. *Ueber die Festigkeits-versuche mit Eisen und Stahl*. 1870.

[48] ABDELKADER, Djebli; MOSTEFA, Bendouba; ABDELKRIM, Aid; ABDERRAHIM, Talha; NOUREDDINE, Benseddiq et al. Fatigue Life Prediction and Damage Modelling of High-density Polyethylene under Constant and Two-block Loading. Online. *Procedia Engineering*. 2015, vol. 101, p. 2-9. ISSN 18777058. Available at: `https://doi.org/10.1016/j.proeng.2015.02.002`. [cit. 2024-01-24].

[49] BERNASCONI, A; DAVOLI, P; BASILE, A a FILIPPI, A. Effect of fibre orientation on the fatigue behaviour of a short glass fibre reinforced polyamide-6. Online. *International Journal of Fatigue*. 2007, vol. 29, p. 199-208. ISSN 01421123. Available at: `https://doi.org/10.1016/j.ijfatigue.2006.04.001`. [cit. 2024-01-24].

[50] MOORE, David R.; WILLIAMS, J.G.; Pavan, A.*Fracture mechanics testing methods for polymers, adhesives and composites*. Elsevier, 2001. ISBN 0080531962.

[51] ARBEITER, Florian; SPOERK, Martin; WIENER, Johannes; GOSCH, Anja a PINTER, Gerald. Fracture mechanical characterization and lifetime estimation of near-homogeneous components produced by fused filament fabrication. Online. *Polymer Testing*. 2018, vol. 66, p. 105-113. ISSN 01429418. Available at: `https://doi.org/10.1016/j.polymertesting.2018.01.002`. [cit. 2024-01-24].

[52] KLIMKEIT, B.; NADOT, Y.; CASTAGNET, S.; NADOT-MARTIN, C.; DUMAS, C. et al. Multiaxial fatigue life assessment for reinforced polymers. Online. *International Journal of Fatigue*. 2011, vol. 33, p. 766-780. ISSN 01421123. Available at: `https://doi.org/10.1016/j.ijfatigue.2010.12.004`. [cit. 2024-01-24].

[53] BERREHILI, A.; CASTAGNET, S. a NADOT, Y. Multiaxial fatigue criterion for a high-density polyethylene thermoplastic. Online. *Fatigue & Fracture of Engineering Materials & Structures*. 2010, vol. 33, iss. 6, p. 345-357. ISSN 8756-758X. Available at: `https://doi.org/10.1111/j.1460-2695.2010.01446.x`. [cit. 2024-01-24].

[54] NITTA, Akito; OGATA, Takashi a KUWABARA, Kazuo. Fracture Mechanisms And Life Assessment Under High-strain Biaxial Cyclic Loading Of Type 304 Stainless Steel. Online. *Fatigue & Fracture of Engineering Materials & Structures*. 1989, vol. 12, iss. 2, p. 77-92. ISSN 8756-758X. Available at: `https://doi.org/10.1111/j.1460-2695.1989.tb00515.x`. [cit. 2024-03-13].

[55] Microsoft Excel. *Microsoft Corporation* . 2019. Software.

[56] MATLAB version: 9.13.0 (R2022b). *The MathWorks Inc.* Software.

[57] Ansys® Mechanical Enterprise, Release 23.2. Software.

[58] Ansys® Mechanical Enterprise, Release 24.1. Software.

[59] ASTM INTERNATIONAL [ISO]. ASTM D638-22: *Standard Test Method for Tensile Properties of Plastics*. ASTM International, 2022. Available at: `http://dx.doi.org/10.1520/D0638-22`.

[60] INTERNATIONAL ORGANIZATION FOR STANDARDIZATION [ISO]. ISO 527-1:2019, *Plastics — Determination of tensile properties — Part 1: General principles*. Geneva: ISO, 2019.

[61] INTERNATIONAL ORGANIZATION FOR STANDARDIZATION [ISO]. ISO 604:2002, *Plastics — Determination of compressive properties*. Geneva: ISO, 2002.

[62] ASTM INTERNATIONAL [ISO]. ASTM E1876-22: *Standard Test Method for Dynamic Young's Modulus, Shear Modulus, and Poisson's Ratio by Impulse Excitation of Vibration*. ASTM International, 2022. Available at: `http://dx.doi.org/10.1520/E1876-22`.

[63] GRIEDER, Stefan; ZHILYAEV, Igor; KÜNG, Marco; BRAUNER, Christian; AKERMANN, Michael et al. Consolidation of Additive Manufactured Continuous Carbon Fiber Reinforced Polyamide 12 Composites and the Development of Process-Related Numerical Simulation Methods. Online. *Polymers*. 2022, vol. 14, iss. 16. ISSN 2073-4360. Available at: `https://doi.org/10.3390/polym14163429`. [cit. 2024-04-08].

[64] LAMMENS, N.; DE BAERE, I. and VAN PAEPEGEM, W. On the orthotropic elasto-plastic material response of additively manufactured polyamide 12. Online. *7th bi-annual international conference of Polymers & moulds innovations*. Ghent, Belgium, 2016. ISBN 9789081313605. Available at: `https://biblio.ugent.be/publication/8086754`. [cit. 2024-04-08].

[65] ASTM INTERNATIONAL [ISO]. ASTM 7791-22: *Standard Test Method for Uniaxial Fatigue Properties of Plastics*. ASTM International, 2022. Available at: `http://dx.doi.org/10.1520/D7791-22`.

[66] SMITH, K. N.; WATSON, P. and TOPPER, T. H. A Stress-Strain Function for the Fatigue of Metals. *Journal of Materials*, JMLSA, vol. 5, iss. 4, p. 767-778. [cit. 2023-10-23].

[67] HUTAŘ, Pavel and TRÁVNÍČEK, Lukáš. *High cycle fatigue of PPC+MB, Bayblend T85XF, Finalloy EBP830 and PP+TPO TD15+rc*. Technical report. Brno, September 2022.

[68] KELLY, P.A. *An introduction to Solid Mechanics.*. Mechanics Lecture Notes: Engineering Solid Mechanics - small strain. University of Auckland, 2012. Available at: `https://pkel015.connect.amazon.auckland.ac.nz/SolidMechanicsBooks/Part_II/08_Plasticity/08_Plasticity_02_Stress_Analysis.pdf`. [cit. 2024-04-08].

Symbols and abbreviations

2PP	two-photon polymerisation
ABS	acrylonitrile butadiene styrene
AM	additive manufacturing
APDL	ansys parametric design language
BJT	binder jetting
CAD	computer-aided design
CLIP	continuous liquid interface production
DED	directed energy deposition
DIW	direct ink writing
DLP	digital light processing
DMD	digital micromirror device
DNG	double-negative
DPS	double-positive
FDM	fused deposition modelling
FEM	finite element method
FFF	fused filament fabrication
GF	glass fibre
HDPE	high-density polyethylene
IPM	institute of physics of materials
LHM	left-handed materials
LOM	laminated object manufacturing
MEX	material extrusion
MJT	material jetting
NTE	negative thermal expansion
PA	polyamide
PBF	powder bed fusion
PBT	polybutylene
PCCL	polymer competence center leoben
PDMS	polydimethylsiloxane
PE	polyethylene
PEEK	polyether ether ketone
PET	polyethylene terephthalate
PLA	polylactic acid
PP	polypropylene
PVA	poly(vinyl alcohol)
SDL	selective deposition lamination
SHL	sheet lamination
SLA	stereolithography
SLM	selective laser melting
SLS	selective laser sintering
SNG	single-positive
SWT	Smith–Watson–Topper

UV		ultraviolet
VPP		vat photopolymerisation
A	[MPa]	Wöhler curve material parameter
A	[MPa]	fatigue material parameter required by Berrehili criterion
A	[mm^2]	area
A_1	[MPa]	fatigue material parameter required by Nitta et al. criterion
B	[-]	Wöhler curve material parameter
c	[-]	fatigue material parameter required by Berrehlili et al. criterion
E	[-]	elastic modulus
E_c	[MPa]	compressive elastic modulus
E_t	[MPa]	tensile elastic modulus
f	[Hz]	frequency
F	[N]	force
$F_\mathrm{c,a}$	[N]	amplitude of compressive force
$F_\mathrm{c,m}$	[N]	mean compressive force
$F_\mathrm{c,min}$	[N]	minimum compressive force
$\mathcal{J}_2$	[MPa^2]	second invariant of the deviatoric stress tensor
$\mathcal{J}_\mathrm{2,m}$	[MPa^2]	second invariant of the deviatoric stress tensor for mean loading
$\mathcal{J}_\mathrm{2,m,0.1}$	[MPa^2]	second invariant of the deviatoric stress tensor for mean loading of a cycle with R-ratio 0.1
$\mathcal{J}_\mathrm{2,m,-1}$	[MPa^2]	second invariant of the deviatoric stress tensor for mean loading of a cycle with R-ratio -1
$\mathcal{J}_\mathrm{2,max}$	[MPa^2]	second invariant of the deviatoric stress tensor for minimum loading
$\mathcal{J}_\mathrm{2,max,0.1}$	[MPa^2]	second invariant of the deviatoric stress tensor for minimum loading of a cycle with R-ratio 0.1
$\mathcal{J}_\mathrm{2,max,-1}$	[MPa^2]	second invariant of the deviatoric stress tensor for maximum loading of a cycle with R-ratio -1
m	[-]	fatigue material parameter required by 1$^\mathrm{st}$ principal and von Mises stress criterion
N	[-]	number of cycles
N_f	[-]	number of cycles to failure
p	[MPa]	pressure
R	[-]	stress asymmetry ratio
t	[s]	time
T	[°C]	temperature
ΔT	[°C]	temperature rise
$\boldsymbol{T}_\varepsilon$		strain tensor
$\boldsymbol{T}_{\varepsilon,\mathrm{principal},F_\mathrm{m}}$		strain tensor in the principal coordinate system

		for mean force
$\boldsymbol{T}_{\varepsilon,\text{principal},F_\text{min}}$		strain tensor in the principal coordinate system for minimum force
$\boldsymbol{T}_\sigma$		stress tensor
$\boldsymbol{T}_{\sigma,\text{global},F_\text{m}}$		stress tensor in the global coordinate system for mean force
$\boldsymbol{T}_{\sigma,\text{global},F_\text{min}}$		stress tensor in the global coordinate system for minimum force
$\boldsymbol{T}_{\sigma,\text{principal},F_\text{m}}$		stress tensor in the principal coordinate system for mean force
$\boldsymbol{T}_{\sigma,\text{principal},F_\text{min}}$		stress tensor in the principal coordinate system for minimum force
u	[mm]	displacement
V	[m^3]	volume
ΔV	[m^3]	volume change
W	[MPa]	strain energy density
ΔW	[MPa]	strain energy density range
x	[mm]	distance
x, y, z		coordinates of the Cartesian coordinate system
α	[-]	fatigue material parameter required by Berrehlili et al. criterion
β	[MPa]	fatigue material parameter required by Berrehlili et al. criterion
β_1	[-]	fatigue material parameter required by Nitta et al. criterion
ε	[-]	strain
$\Delta\varepsilon$	[-]	strain range
ε_1	[-]	first principal strain
$\Delta\varepsilon_1$	[-]	range of the first principal strain
ε_2	[-]	second principal strain
ε_3	[-]	third principal strain
ε_c	[-]	compressive strain
ε_e	[-]	elastic strain
$\Delta\varepsilon_\text{e}$	[-]	elastic strain range
ε_L	[-]	strain in loading direction
ε_m	[-]	mean strain
ε_max	[-]	maximum strain
ε_min	[-]	minimum strain
ε_p	[-]	plastic strain
$\Delta\varepsilon_\text{p}$	[-]	plastic strain range
ε_T	[-]	train in transversal direction
ε_v	[-]	volumetric strain
μ	[-]	Poisson's ratio

σ	[MPa]	stress
$\Delta\sigma$	[MPa]	stress range
σ_a	[MPa]	stress amplitude
$\sigma_{a,0.1}$	[MPa]	stress amplitude of a cycle with R-ratio 0.1
$\sigma_{a,-1}$	[MPa]	stress amplitude of a cycle with R-ratio -1
σ_1	[MPa]	first princiapal stress
$\sigma_{1,a}$	[MPa]	amplitude of the first principal stress
$\Delta\sigma_1$	[MPa]	range of the first principal stress
σ_{1,F_m}	[MPa]	first principal stress at mean force
$\sigma_{1,F_{min}}$	[MPa]	first principal stress at minimum force
$\sigma_{11}, \sigma_{12}, ..., \sigma_{33}$	[MPa]	components of stress tensor in global coordinate system
$\sigma_{11,m}, \sigma_{12,m}, ..., \sigma_{33,m}$	[MPa]	components of stress tensor in global coordinate system for mean loading
$\sigma_{11,min}, \sigma_{12,min}, ..., \sigma_{33,min}$	[MPa]	components of stress tensor in global coordinate system for minimum loading
σ_c	[MPa]	pressure
$\sigma_{c,a}$	[MPa]	amplitude of pressure
σ_e	[MPa]	endurance limit
σ_{eq}	[MPa]	equivalent stress
σ_f	[MPa]	fatigue material parameter required by 1st principal and von Mises stress criterion
σ_m	[MPa]	mean stress
$\sigma_{m,0.1}$	[MPa]	mean stress of a cycle with R-ratio 0.1
σ_{max}	[MPa]	maximum stress
σ_{min}	[MPa]	minimum stress
σ_{vM}	[MPa]	von Mises stress
$\sigma_{vM,a}$	[MPa]	amplitude of von Mises stress
σ_{vM,F_m}	[MPa]	von Mises stress at mean force
$\sigma_{vM,F_{min}}$	[MPa]	von Mises stress at minimum force

List of Figures

List of Tables

Appendices

A   Cyclic loading temperature measurement

This appendix addresses the measurement of temperature increase mentioned in Section 7.4. The experiments were carried out for loading frequencies $f = 5$, 10, and 15 Hz for loading amplitudes 2, 4, 6, 8, and 10 MPa, with $R = 0.1$. The experiments were performed using an INSTRON E3000 computer-controlled testing machine. Two thermometers were used to record the temperature in the room and on the surface of the specimen, respectively.

A loading scheme was set for each specimen for a given loading frequency. A two-hour idle interval was set at the start of a test to allow for stabilisation of temperatures after sample and thermometer mounting. After that, the machine alternated between intervals of 30 000 cycles at a given stress level and intervals of two-hour idleness. The loading was applied in an ascending manner. The number of cycles withstood in an interval was noted. In case of a specimen failure, the number of cycles for a given interval was recorded, and the test was stopped. The temperature was measured at both locations for the entire duration of the test.

The data obtained for temperature and number of cycles were analysed. The continuous temperature data were split into intervals of idleness and loading using measurement time stamps, number of cycles, and loading frequency. A temperature increase was calculated, as well as its derivative, which describes whether the internal heating is substantial and the loading conditions would lead to self-heating fatigue failure.

Graphs of the temperature increase and its derivative for a loading frequency of $f = 5$ Hz are shown in Fig. A.1, for $f = 10$ Hz in Fig. A.2, and for $f = 15$ Hz in Fig. A.3.
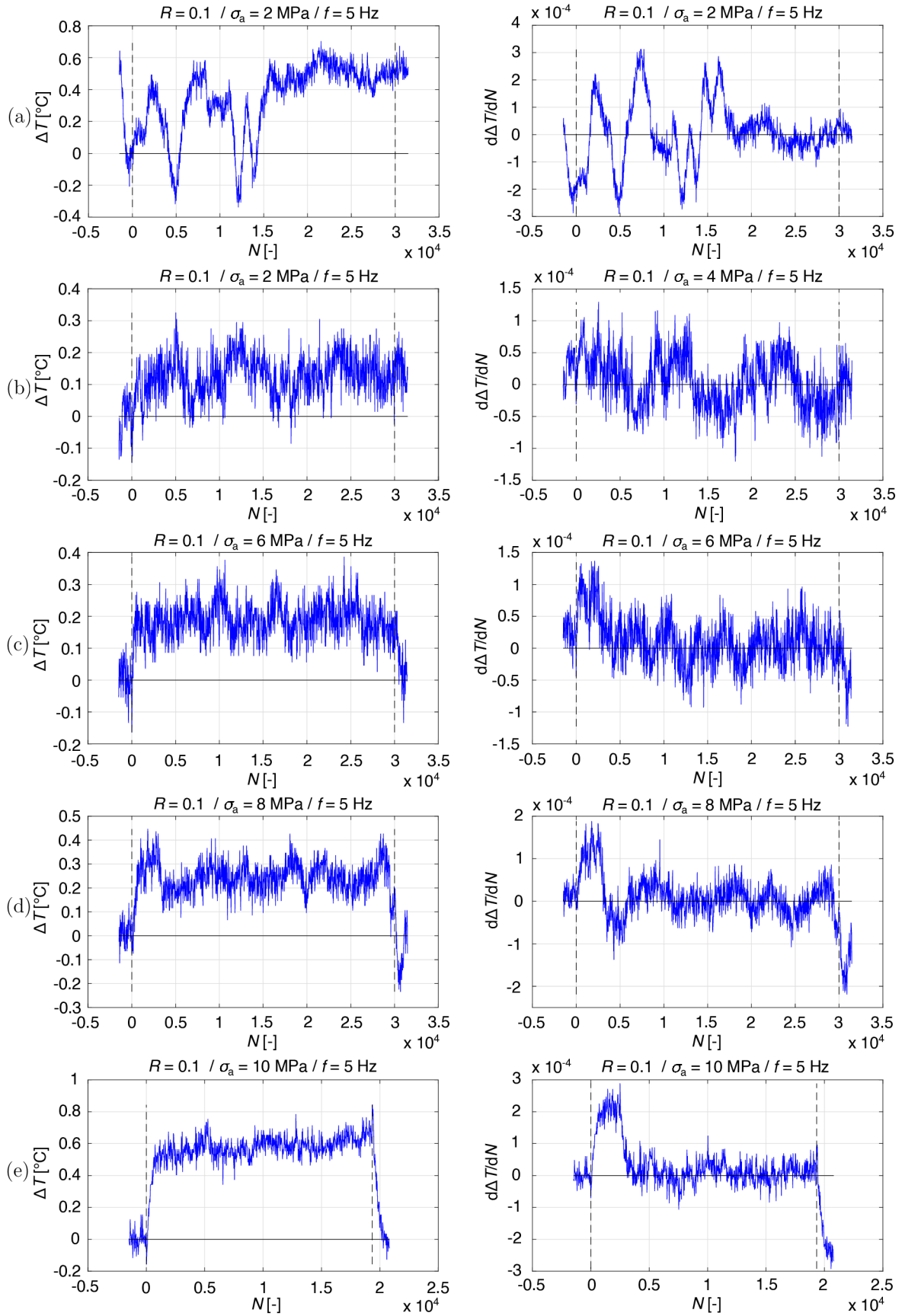
Fig. A.1: Temperature evolvement over cycling and its derivative for $f = 5$ Hz, $R = 0.1$, and $\sigma_a =$ (a) 2, (b) 4, (c) 6, (d) 8, (e) 10 MPa.
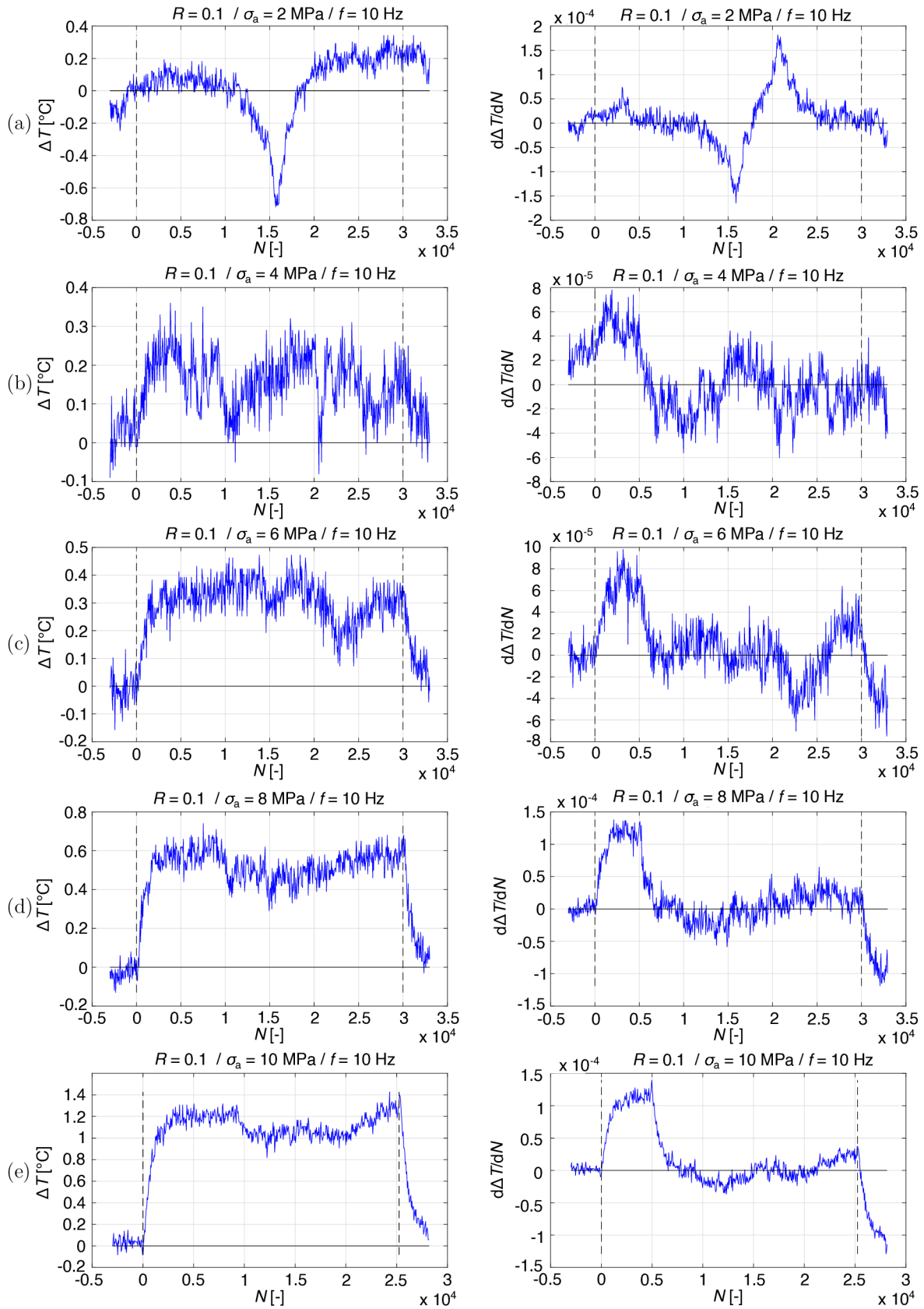
Fig. A.2: Temperature evolvement over cycling and its derivative for $f = 10$ Hz, $R = 0.1$, and $\sigma_a =$ (a) 2, (b) 4, (c) 6, (d) 8, (e) 10 MPa.
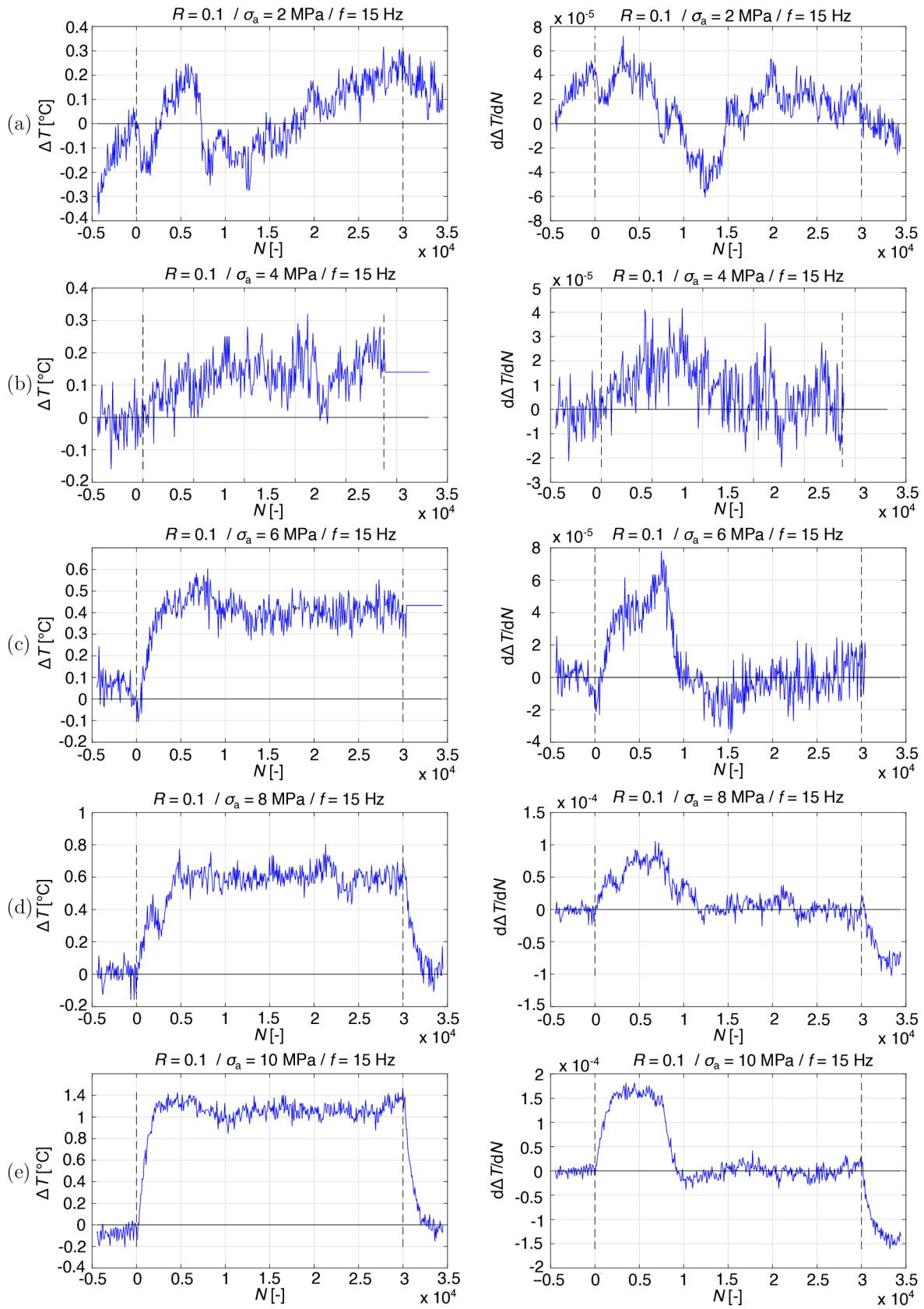
Fig. A.3: Temperature evolvement over cycling and its derivative for $f = 15$ Hz, $R = 0.1$, and $\sigma_a =$ (a) 2, (b) 4, (c) 6, (d) 8, (e) 10 MPa.

B   Criteria response to different stress states

To analyse the behaviour of the von Mises and Berrehili et al. second invariant criteria for different stress states, the original stress state at each location was altered into different variations, and the lifetimes predicted for each of these variations. Lifetimes were estimated using the two investigated criteria, as well as the first principal stress criterion to compare the results. The Wöhler curve of the tested structure is also plotted in the graphs. The first principal stress was always kept at the original value, and the second or third principal stress was changed, respectively (third principal stress for the first critical location and second principal stress for the second critical location). For the first critical location, the third principal stress σ_3 was altered into $0.5 \cdot \sigma_3$, $0.25 \cdot \sigma_3$, $\sigma_3 = 0$, $-0.25 \cdot \sigma_3$, $-0.5 \cdot \sigma_3$, and $-\sigma_3$, respectively. For the second critical location, the second principal stress was altered into $0.5 \cdot \sigma_2$, $0.25 \cdot \sigma_2$, $\sigma_2 = 0$, $-0.25 \cdot \sigma_2$, $-\sigma_2$, and $1.5 \cdot \sigma_2$, respectively.

It can be concluded that these criteria are highly dependent on the stress range present at the given location. When the stress range increases, the ability of the criteria to predict the lifetime decreases. Larger difference between the principal stresses results in a larger internal shear, which can be seen in the respective Mohr's circles (Fig. B.1). This might reduce the capability of the criteria to correctly predict the lifetime. Furthermore, for uniaxial and equibiaxial stress states, both of these criteria are reduced to the first principal stress criterion.

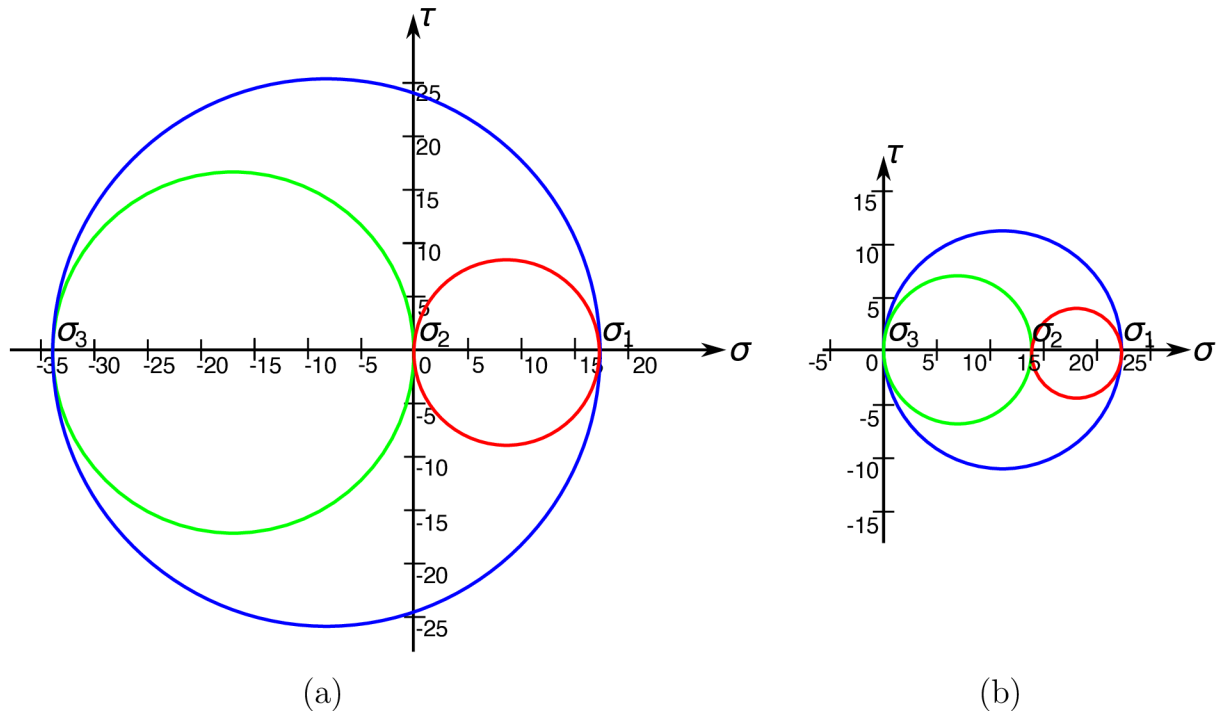(a)   (b)

Fig. B.1: Mohr's circle of the (a) first critical location, (b) second critical location representing the stress state of each location for the loading case of the minimum force corresponding to a pressure magnitude of 4 MPa.
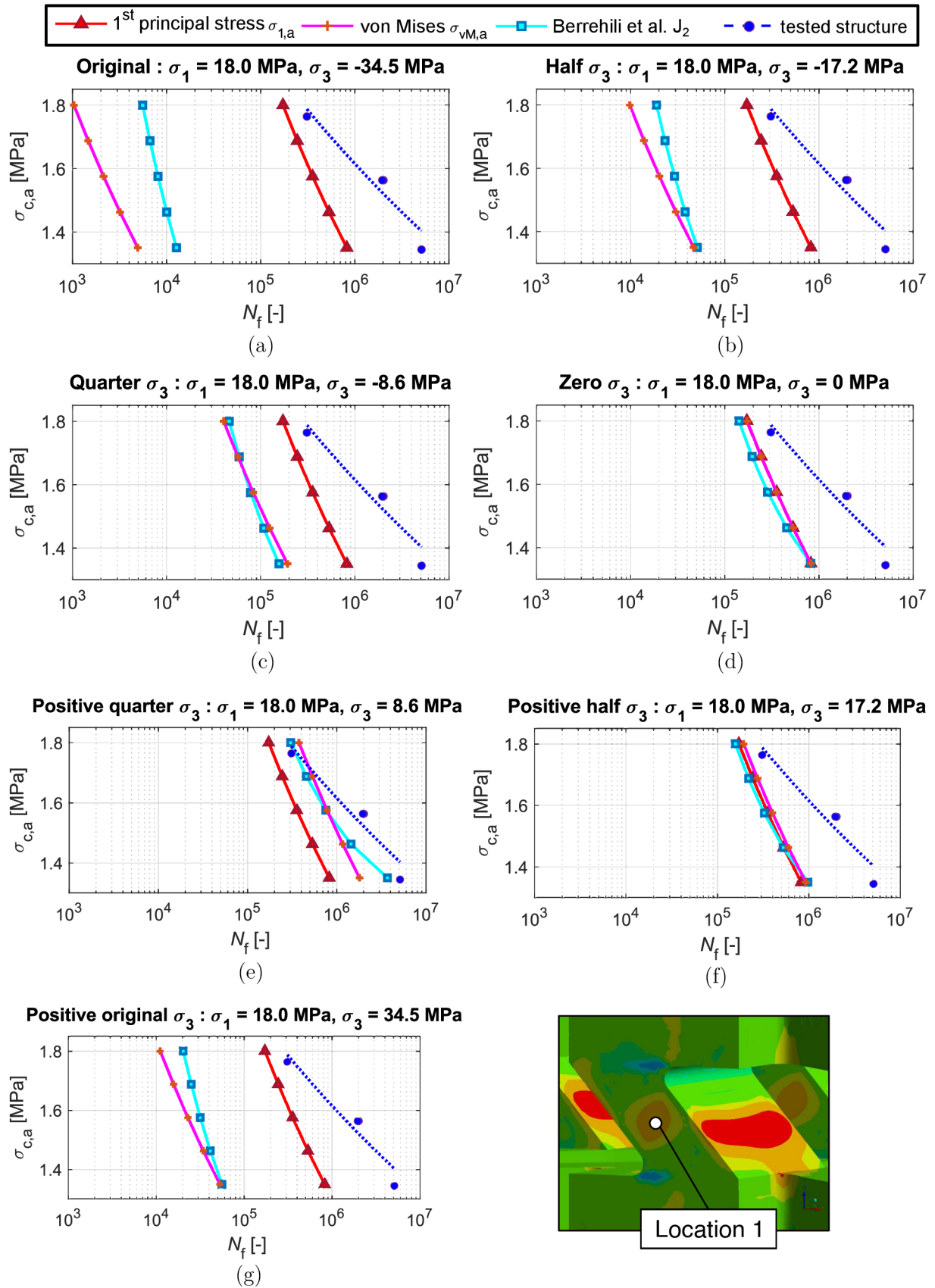
Fig. B.2: Lifetime estimations according to the first principal stress criterion, von Mises criterion, and Berrehili et al. second invariant criterion for different biaxial stress states at the first critical location. Note that for uniaxial (d) and equibiaxial (f) stress state the Berrehili et al. and von Mises criteria reduce to the first principal stress criterion.
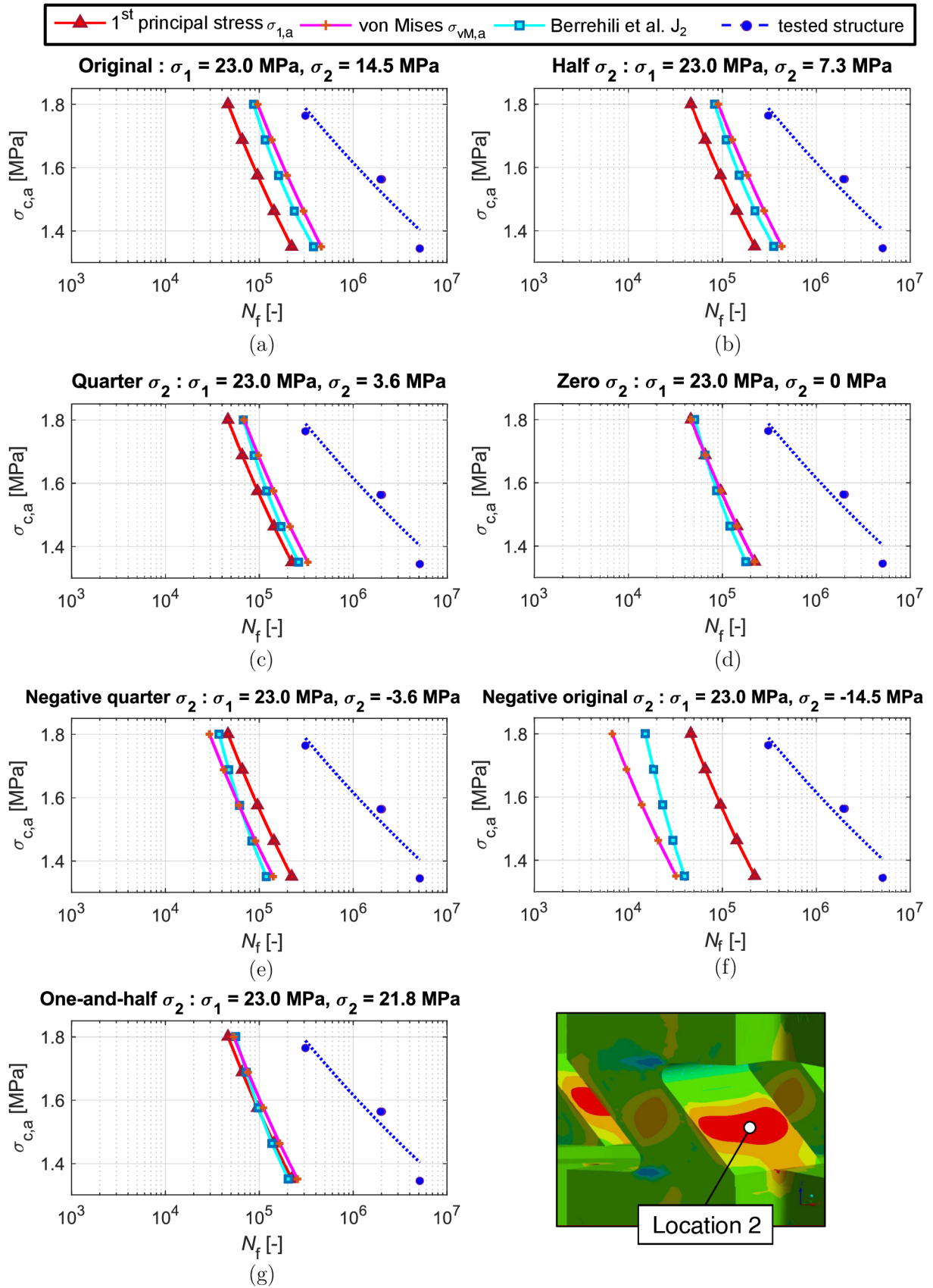
Fig. B.3: Lifetime estimations according to the first principal stress criterion, von Mises criterion, and Berrehili et al. second invariant criterion for different biaxial stress states at the second critical location. Note that for uniaxial (d) and equibiaxial (g) stress state the Berrehili et al. and von Mises criteria reduce to the first principal stress criterion.